DEUTSCHES ELEKTRONEN-SYNCHROTRON

DESY

A Study of
Quasi-Real QED Compton Events at HERA

by

R. Maraček
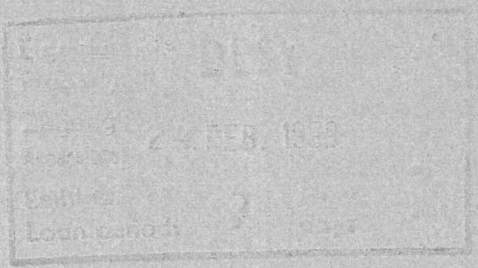
NOTKESTRASSE 85 - 22607 HAMBURG

Institute of Experimental Physics
Slovak Academy of Sciences, Košice
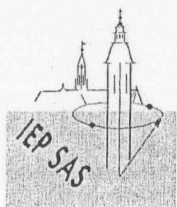
A Study of Quasi-Real QED Compton Events at HERA

Mgr. Richard Maraček

PhD Thesis

Košice 1998

Abstract

An experimental study of the QED Compton process using the data recorded by the H1 detector at the electron-proton collider HERA in 1994 and 1995 is presented. Using the samples of these events the backward electromagnetic calorimeters, i.e. lead-scintillator sampling calorimeter BEMC in 1994 and the one of the spaghetti lead-fibre type SPACAL in 1995 were studied in terms of the absolute energy scale, response linearity, relative position to the beam line, and the corresponding backward tracking detector, i.e. backward proportional chamber (BPC) in 1994 and backward drift chamber (BDC) in 1995. The efficiencies of the BPC and BDC are determined, the probability of the γ-conversion in front of the BPC-BEMC and BDC-SPACAL systems are evaluated and the amount of the dead material in that region is estimated. The selected samples of the QED Compton events are employed to make an independent luminosity measurement. The rôle of the results of the QED Compton events analysis in the physics analysis such as the proton structure function F_2 measurement is discussed.

Abstrakt

V predkladanej dizertačnej práci sa zaoberáme analýzou kvantovo-elektrodynamického (QED) Comptonovho rozptylu použitím údajov získaných pomocou detektora H1 pracujúceho na urýchľovači protibežných zväzkov elektrónov a protónov HERA v rokoch 1994 a 1995. Pomocou štatistických súborov prípadov spomínaných zrážok sme najprv študovali absolútnu energetickú kalibráciu, a linearitu odozvy zadného elektomagnetického vzorkovacieho kalorimetera (BEMC) olovo-scintilátorovej konštrukcie v roku 1994 a kalorimetra špagetového typu (SPACAL) olovo-vláknovej konštrukcie v roku 1995. Ďalej sme určili relatívnu polohu oboch kalorimetrov voči osi zväzku a odpovedajúcemu dráhovému detektoru, t.j. zadnej proporcionálnej komore (BPC) v roku 1994 a tzv. zadnej driftovej komore (BDC) v roku 1995. Potom sme vyčíslili efektívnosť dráhových detektorov BPC a BDC a pravdepodobnosť γ-konverzie. Následne sme odhadli množstvo mŕtveho materiálu pred systémami BPC-BEMC a BDC-SPACAL. Získané štatistické súbory prípadov QED Comptonovho rozptylu sme použili na nezávislé meranie svietivosti. Záver práce sme venovali diskusii o úlohe výsledkov analýzy prípadov QED Comptonovho rozptylu v tak dôležitej fyzikálnej analýze ako je meranie štruktúrnej funkcie protónu F_2.

A note on units

In this thesis, a system of natural units will be used, whereby $\hbar = c = 1$.

Contents

Chapter 1

Introduction

The electron-proton beam facility HERA at DESY, Hamburg, collide the two counter-rotating beams of 27.5 GeV electrons (positron) and 820 GeV protons [1]. The center of mass energy of the ep collision is $\sqrt{s} \simeq 300$ GeV. Compared to former fixed target experiments [2, 3, 4, 5, 6], where the nucleons probed by the leptons were at the rest in the laboratory frame, the center of mass energy is larger by more than one order of magnitude. HERA provides thus a unique facility for the study of the structure of the proton in a new kinematical regime: at very large $-Q^2 \simeq 10^4$ GeV^2 (where Q^2 is the squared momentum transfered) allowing to resolve structure down to 10^{-18} cm, and in the region of high parton density in the momentum space (very low Bjorken scaling variable $x \simeq 10^{-4}$).

Deep inelastic scattering (DIS) is a fundamental process to investigate the quark-gluon interaction, and to make precise tests of the perturbative quantum chromodynamics (QCD) theory. The inclusive analysis of the DIS events leads to measurements of the proton structure function $F_2(x, Q^2)$. The strong coupling constant $\alpha_s(Q^2)$ and the gluon distribution $xg(x, Q^2)$ can be determined in different processes as deep inelastic jet production, charm and J/ψ production or the measurement of longitudinal structure function F_L. However, the accurate measurement of the structure functions is the most precise way to determine $\alpha_s(Q^2)$, and $xg(x, Q^2)$ from the scaling violation of F_2. The high statistics measurements of the proton structure already obtained in the first years of running at HERA require to lower the systematics errors, which main sources are electron energy calibration error, electron polar angle uncertainty, uncertainty of the hadronic energy scale, knowledge of the QED radiative correction, photo-production and beam background, the luminosity error.

The measurement of the radiative inelastic and elastic scattering processes is of the primary importance at HERA because it allows to cross check of the QED radiative corrections, which are indispensable in the determination of the proton structure. In addition since at the elastic process the corresponding cross section can be precisely calculated this process is used to monitor the luminosity at HERA. The number of great importance for most of the physics analyses. In the DIS regime the emission of photons collinear with the incident electrons can be interpreted as a reduction of the effective electron beam energy and consequently the center of mass energy of collisions. Thus exploiting of hard proton radiation processes can yield information on the internal proton structure at distances

larger than previously studied at HERA. In addition it can provide a measurement such as determination of the cross sections for scattering of longitudinally, σ_L, and transversally, σ_T, polarized photons [7].

In order to measure the luminosity delivered in the acceptance region of the H1 detector, four different methods are presently used: the $(e - \gamma)$ coincidence, the hard γ rate, the random coincidence and the Compton method. The precision of the later (former) two methods is presently limited by the statistical (systematic) error. The agreement of the different values using largely independent methods provides confidence of our understanding of the luminosity measurement.

As it was suggested in [8, 9] the QED Compton scattering, produced in the head-on collision at high-energy electron proton collider, such as HERA, can be used for various purposes: for the already mentioned above luminosity measurement, the methodological/calibration studies of detectors, the determination of the photon content of the proton and the search for a candidate for excited electron e^*.

In the presented thesis the QED Compton event observed in the H1 detector during the 1994 and 1995 running periods are analyzed. Although the amount of collected luminosity during the 1994 and 1995 and the different trigger configurations put limits on the here presented analysis, the selected samples of the QED Compton events provides an opportunity to cross-check the total integrated luminosity with a precision of few per cent. It also allows us to study the backward scattering region of the H1 experiment in terms of the absolute energy scale and the response linearity of the electromagnetic calorimeter, its relative position to the beam line and the misalignment of the calorimeter and the tracking detector. The mentioned above methodological studies are of greater importance since during the winter shutdown 1994/95 the H1 collaboration has upgraded the H1 detector with a new backward calorimeter of the spaghetti (SPACAL) lead-fiber design and the new backward tracking detector (BDC) [10]. In order to fulfill the main target of this upgrade, i.e. to provide the improved measurement of the scattered particles in the new extended kinematical region, the newly installed detectors were to be well understood and calibrated.

The thesis is organized as follows. In chapter 2 theoretical issues relating to hard photon radiation processes at HERA are surveyed and the formulas for quasi-real QED Compton event are presented. Chapter 3 contains a brief description of the HERA accelerator and a review of the components of the H1 detector with emphasizing on H1 backward scattering region, which is mainly relevant for the presented analysis. Chapter 4 is concerned with the study of the BEMC nuclear counter effect as a source of the fake electron trigger signals and the increase of the rate of the stand-alone BEMC electron trigger, which was used for selecting not only the QED Compton event candidates but the candidates on the deep-inelastic scattering events. In Chapter 5 the experimental techniques used to select the QED Compton event samples in both 1994 and 1995 data taking periods are described. Chapter 6 is concerned with the methodological studies of the electromagnetic calorimeters in terms of the absolute energy scale, response linearity, relative position to the beam line, the misalignment of the calorimeter and the tracking detector. The measurement of total integrated luminosity using the QED Compton events detected by H1 experiment during the 1994 and 1995 running periods, is then presented. In Chapter 7 the rôle of the QED Compton events analysis in the physics analysis such as

measurement of the proton structure function F_2 is illustrated and discussed. The final chapter reviews the results obtained.

Chapter 2

The Quasi–Real QED Compton Process

In this chapter a survey of the definitions of the three classes of the hard photon radiation from the lepton line in the neutral current (NC) processes at HERA is given. The exact analytic expressions of the QED Compton event cross section are presented. The three separate contributions depending on the value of the invariant mass of the hadronic system are reviewed. The definitions of the kinematical relations, which characterize the QED Compton events are presented. The basic ideas and solutions which have been chosen in COMPTON, a Monte Carlo generator for QED Compton events, are summarized together with the input values of the kinematical variables used in the production of the Monte Carlo simulation data used in the here presented analysis. Finally the various predictions of the distributions and correlations of the crucial kinematical variables for a sample of the QED Compton events generated using the COMPTON generator are shown and discuss.

2.1 Radiative Events in Electron-Proton Scattering at HERA Energies

The dominant QED radiative contributions to elastic ($ep \rightarrow ep$) and inelastic ($ep \rightarrow eX$) scattering consist the radiation of a real photon from the leptonic line and are described by diagrams shown in Fig. 2.1.

The radiative scattering cross section is large in the neighborhood of the poles of the virtual electron and virtual photon propagators. The following three classes of the radiative processes corresponding to these kinematic domains are defined [11, 35]: (i) the bremsstrahlung process corresponding to the poles in both the virtual electron and the virtual photon propagators; (ii) the radiative DIS process corresponding to the pole in the virtual electron propagator and to the large virtual photon mass; (iii) the quasi-real QED Compton process corresponding to the pole in the virtual photon propagator and to a large virtual electron mass. Note, that these three classes of radiative processes correspond to the "different" kinematic domains.
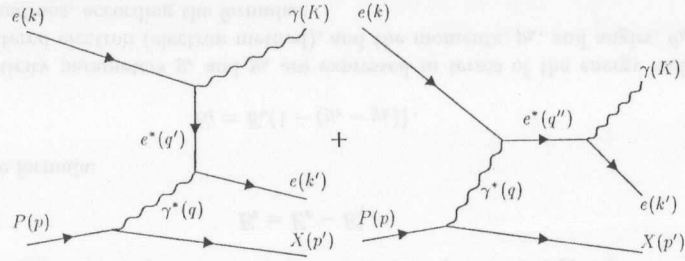
Fig. 2.1: The Feynman diagram for the radiative $(ep \to e\gamma + X)$ scattering.

A complete example of treatment of the radiative channels is described in [9], where the authors concentrate on the pure photon exchange contribution to the cross section which is essentially determined by factor:

$$\frac{1}{z_1 z_2 \hat{Q}^2} \tag{2.1}$$

with (note that the factors in denominator are not independent):

$$z_1 = 2(K.k), \tag{2.2}$$
$$z_2 = 2(K.k'), \tag{2.3}$$
$$\hat{Q}^2 = -(k - k' - K)^2 = Q^2 + z_1 + z_2. \tag{2.4}$$

Using the partial fractioning and, consequently, the fact that the factors multiplying the pole terms terms $1/z_1$, $1/z_2$ and $1/\hat{Q}^2$ do not vary strongly and therefore for kinematically allowed configurations none of the other denominators can become small, the cross section can be decomposited into the form:

$$\sim \frac{M_1}{z_1} + \frac{M_2}{z_2} + \frac{M_{\hat{Q}^2}}{\hat{Q}^2}. \tag{2.5}$$

This separation defines three radiative channels: (j) initial state radiation, peaking for $z_1 \to 0$, i.e. for events where the photon is emitted colinearly with (jj) the incoming electron; final state radiation, peaking for $z_2 \to 0$, i.e. for events where the photon is emitted colinearly with the scattered electron; (jjj) Compton part, peaking for $\hat{Q}^2 \to 0$. These events are characterized by the photon balancing the transverse momentum of the scattered electron and the final quark which is going close to the initial quark direction. The contribution of the Compton part to the bremsstrahlung cross section can be viewed as resulting from the emission of a quasi-real photon from the quark line with subsequent Compton scattering, $e\gamma \to e\gamma$.

Since the nature of these processes is that there are no substantial or discrete borders in the phase space, the way to separate them is based on their distinct experimental signatures [35], as it is defined in the following sections.

In the H1 detector which will be described in more detail in Sec. 3.2 the radiative photons are measured (in terms of their polar angle θ_γ) in two angular domains: $\theta_\gamma \leq \theta_{pa}$ corresponding to the acceptance region of the photon arm of the luminosity detector, θ_{pa}, and $\theta_{cd1} \leq \theta_\gamma \leq \theta_{cd2}$ corresponding to the acceptance of the region of the central detector, where θ_{cd1} and θ_{cd2} are the minimal and maximal angular acceptance of the central detector, respectively. The scattered electrons are measured (in terms of their polar angle θ_e), either in the central detector or in the electron arm of the luminosity system $\theta_e \leq \theta_{ea}$, where θ_{ea} is the upper edge of the acceptance of the electron arm of the luminosity system. The radiative photon and the scattered electron of energy $E'_e \geq 10$ GeV cannot be resolved in any region of the central detector if the photon emission angle, $\delta_{e\gamma}$, with respect to the electron is smaller than δ_{cd}, where the δ_{cd} stands for the angular $(e - \gamma)$ resolution of the central detector. The approximate values of the borders of the mentioned above acceptance regions together with the corresponding symbols are summarized in Tab. 2.1.

border of detector acceptance region		polar angle
photon arm of the luminosity system	θ_{pa}	≤ 0.45 mrad
electron arm of the luminosity system	θ_{ea}	≤ 5 mrad
central detector (forward part)	θ_{cd1}	≥ 0.07 rad
central detector (backward part)	θ_{cd2}	$\leq (\pi - 0.05)$ rad
$e - \gamma$ resolution[1]	δ_{cd}	≥ 0.02 rad

Tab. 2.1: Approximate values of the borders of the acceptance regions.

The kinematic variables p, k, p', k', K are the four-momenta of the incoming proton, incoming electron, hadronic system[2], scattered electron and radiated photon, respectively. The kinematics of the radiative processes are described by the five following independent Lorentz-invariant variables:

$$q^2 = (p' - p)^2 = -Q^2, \tag{2.6}$$
$$s = (k + p)^2, \tag{2.7}$$
$$t = (K - k)^2, \tag{2.8}$$
$$W^2 = (k' + K)^2, \tag{2.9}$$
$$W_h^2 = p'^2. \tag{2.10}$$

The four-momentum transfer squared, t, and the squared invariant mass of the $(e - \gamma)$ system, W^2, correspond to q'^2 and q''^2 in the diagrams in Fig. 2.1.

2.1.1 Bremsstrahlung Process

In the bremsstrahlung process the masses of the virtual photon and of the virtual electron are small: $0 \leq -q^2, -q'^2, -q''^2 \lesssim (E_e \theta_{pa})^2 \simeq 0.00015$ GeV^2. In this kinematical domain the elastic channel $(ep \to ep\gamma)$ is the dominant process. The electron radiates a photon in the electromagnetic field of the proton, which can be regarded as point-like. Both

---

[1]For more detail definition see the text.

[2]In the elastic case a proton.

the outgoing electron and the photon emerge at very small angles with respect to the incident electron direction. The recoil proton continues its motion almost undisturbed. Events of this type are identified either by detecting both the scattered electron and the photon or by detecting only the photon. In the bremsstrahlung process the energy of the photon, E'_γ, and the energy of the scattered electron, E'_e, are constrained:

$$E'_\gamma = E_e - E'_e, \tag{2.11}$$

where E_e and E'_e being the energy of incoming and scattered electron, respectively. In the unrelativistic limit and in the small angle approximation the bremsstrahlung cross section is described by the Bethe–Heitler formula [15]. Since the cross section is insensitive to the internal proton structure, the bremsstrahlung process can be used for the luminosity measurement, see Sec. 6.3.1.1.

2.1.2 Radiative DIS Process

In the radiative DIS process $-q^2$ is large, $-q^2 \gtrsim (E_e \theta_{cd1})^2$, while either $-q'^2$ or $-q''^2$ is small, $-q'^2 \lesssim (E_e \theta_{pa1})^2 \simeq 0.00015$ GeV^2, $-q''^2 \lesssim (E_e \delta_{cd})^2$. Since the inelastic structure function of the proton rises[3], and the elastic form factors decrease rapidly with increasing $-q^2$, this process is dominated by the inelastic channel.

As $-q^2$ is large, the scattered electron or the $(e - \gamma)$ system is observed in the angular range $\theta_e \geq \theta_{cd1}$ and a large fraction of the produced hadrons is detected. The transverse momentum of the hadronic system is balanced by the transverse momentum of the electron $(e - \gamma)$ system. The angular distribution of the radiated photons in DIS exhibits two peaks around the directions of the incident and scattered electron, corresponding to the region of small $-q'^2$ and small $-q''^2$, respectively.

Despite most of the radiative photons emitted in the direction of the scattered electrons of energy $E \geq 10$ GeV cannot be resolved a sizeable fraction of events with radiative photons emitted in the direction of the incoming electrons can be identified in the H1 detector. These kind of events can be interpreted as originating from non-radiative scattering at reduced electron beam energy [7]. The effective, so-called true, electron beam energy E_t can be determined directly from the measured radiative photon energy E'_γ:

$$E_t = E_e - E'_\gamma, \tag{2.12}$$

or from the formula:

$$E_t = E_e(1 - (y_e - y_h)). \tag{2.13}$$

The inelasticity parameters y_e and y_h are expressed in terms of the energy and angle of the scattered electron (electron method), and the momenta, p_h, and angles, θ_h of all produced hadrons, according the formulae:

$$y_e = 1 - \frac{E'_e}{E_e} \sin^2 \frac{\theta_e}{2} \tag{2.14}$$

---

[3]This is valid for $x \leq 0.2$, see e.g. [88, 90]

and

$$y_h = \frac{\Sigma}{2E_e}, \tag{2.15}$$

with

$$\Sigma = \sum_h (E_h - p_h \cos \theta_h). \tag{2.16}$$

The DIS ep collision at reduced energy E_t can be described using the "true" kinematical variables x_t, y_t, and Q_t^2 defined as:

$$x_t = \frac{E_t E'_e \cos^2 \theta_e/2}{E_p (E_t - E_e \sin^2 \theta_e/2)}, \tag{2.17}$$

$$y_t = 1 - \frac{E'_e}{E_t} \sin^2 \theta_e/2, \tag{2.18}$$

$$Q_t^2 = 4 E'_e E_t \cos^2 \theta_e/2, \tag{2.19}$$

which can be obtained by replacing the nominal electron beam energy by the effective "true" electron energy in the conventional expressions for x_e, y_e, Q_e^2, see Sec. 7.1.

2.1.3 Quasi-Real QED Compton Process

In the QED Compton process both $-q'^2$ and $-q''^2$ are large, $-q'^2, -q''^2 \gtrsim (E_e \theta_{cd1})^2$ and $-q^2$ is small, $m_p(W^4/s^2) \leq -q^2 \ll -q'^2, -q''^2$ (quasi-real electron), where m_p is the proton mass. Ignoring the hadronic vertex, this process corresponds to the Compton scattering of a quasi-real photon on an incident electron [8]:

$$e + \gamma^* \to e + \gamma$$

The dominant contribution to the Compton scattering, which is sometimes called wide angle bremsstrahlung is due to the elastic channel ($ep \to ep\gamma$). The scattered electron and the photon are observed in the central detector ($\theta_{e(\gamma)} \geq \theta_{cd1}$). As $-q^2$ is small, the proton (hadronic final state) and the $(e - \gamma)$ system have transverse momenta close to zero. The hadronic final state remains undetected in most of the cases ($\theta_{p(h)} \leq \theta_{cd2}$).

Note that in the Compton process the corrections of the order α^4, where α is fine-structure constant, (i.e. second order radiative corrections) have to be taken into account, in particular the dominant one corresponded to hard photon emission in the direction of the incoming electron. A more detail discussion of the three channels of the quasi-real QED Compton is the subject of the next section.

2.2 QED Compton Scattering in Electron-Proton Collisions

2.2.1 Exact Analytic Expression of QED Compton Event Cross Section

In this section the exact analytic expression of the QED Compton event cross section is presented. According to [11] we start with the exact factorization formula, based on the

helicity calculation, see Appendix A, for the process shown in Fig. 2.1:

$$\frac{d^4\sigma(ep \to e\gamma X)}{dx\, dx_\gamma\, dQ^2\, d\Omega^*} = f^T_{\gamma^*/p}(x, x_\gamma, Q^2)\left(\frac{d\sigma}{d\Omega^*}\right)^T + f^L_{\gamma^*/p}(x, x_\gamma, Q^2)\left(\frac{d\sigma}{d\Omega^*}\right)^L \qquad (2.20)$$

with

$$\left(\frac{d\sigma}{d\Omega^*}\right)^T = \frac{d\sigma_T}{d\Omega^*} + \epsilon\frac{d\sigma_L}{d\Omega^*} + \sqrt{2\epsilon(1+\epsilon)}\frac{d\sigma_{TL}}{d\Omega^*}\cos\phi^* + \epsilon\frac{d\sigma_{TT}}{d\Omega^*}\cos 2\phi^*, \qquad (2.21)$$

$$\left(\frac{d\sigma}{d\Omega^*}\right)^L = \frac{d\sigma_T}{d\Omega^*} + \frac{1+\epsilon}{2\epsilon}\frac{d\sigma_L}{d\Omega^*} + \sqrt{2\frac{1+\epsilon}{\epsilon}}\frac{d\sigma_{TL}}{d\Omega^*}\cos\phi^* + \frac{d\sigma_{TT}}{d\Omega^*}\cos 2\phi^*, \qquad (2.22)$$

where $d\Omega^* = du^* d\phi^*$, with $u^* = \cos\theta^*$, and θ^*, ϕ^* being the orbital and azimuthal scattering angles in the center-of-mass frame of the virtual Compton process. Whilst the upper subscript (T, L) refers to the polarization (transverse or longitudinal) of the virtual photon at the hadron vertex, the lower subscript (T, L, TL, TT) represents the polarization at the lepton vertex, i.e. defines the transverse and longitudinal cross sections, and the transverse-longitudinal and transverse-transverse interference terms of the virtual Compton scattering process $\gamma^* e \to \gamma e$. The flux functions $f^{T,L}$ in formula (2.20), which represent the virtual photon spectra (transverse or longitudinal) at the hadron vertex are given by:

$$f^T_{\gamma/p}(x, x_\gamma, Q^2) = \frac{1-x}{4\pi^3 x x_\gamma}g^T(x, x_\gamma, Q^2)\sigma^T_{\gamma^* p}, \qquad (2.23)$$

$$f^L_{\gamma^*/p}(x, x_\gamma, Q^2) = \frac{1-x}{4\pi^3 x x_\gamma}g^L(x, x_\gamma, Q^2)\sigma^L_{\gamma^* p} \qquad (2.24)$$

with

$$g^L(x, x_\gamma, Q^2) = g^T(x, x_\gamma, Q^2) - \frac{x_\gamma^2}{2x^2} = \qquad (2.25)$$

$$= \frac{(1 - x_\gamma/x)Q^2 - x_\gamma^2 m_p^2}{Q^2 + 4x^2 m_p^2} \qquad (2.26)$$

where the variables x, x_γ are defined as:

$$x = \frac{-q^2}{2pq} \qquad (2.27)$$

$$x_\gamma = \frac{qk}{pk} \qquad (2.28)$$

calling m_p, m_e, m_X the masses of proton, electron and hadronic system, respectively, and defining the squared invariant mass the $(e - \gamma)$ system, $W^2 = (q + k)^2$ and $s = (p + k)^2$. The cross sections $\sigma^{T,L}_{\gamma^* p}$ pertain to the virtual process $\gamma^* p \to X$; their expressions will be given below. In formulas (2.21) and (2.22) the virtual photon polarization parameter ϵ is given by $\epsilon = g^L/g^T$, see [60]. The differential cross sections of the virtual Compton effect

for various polarization of the photon are given by [11]:

$$\frac{d\sigma_T}{d\Omega^*} = \frac{\alpha^2}{W^2 + Q^2}\left[\frac{W^2}{(W^2 + Q^2)(1 + u^* + \eta)} + \frac{(W^2 + Q^2)(1 + u^*)}{4W^2} + \right.$$
$$\left. + \frac{Q^2}{W^2}\frac{1 - u^*}{(1 + u^* + \eta)} + \frac{Q^2(1 - u^*)}{2(W^2 + Q^2)}\right] \qquad (2.29)$$

$$\frac{d\sigma_L}{d\Omega^*} = \frac{\alpha^2}{W^2 + Q^2}\left[\frac{Q^2(1 - u^*)}{W^2 + Q^2}\right] \qquad (2.30)$$

$$\frac{d\sigma_{TL}}{d\Omega^*} = \frac{\alpha^2}{W^2 + Q^2}\left[\frac{QW}{2(W^2 + Q^2)}\sqrt{1 - u^{*2}}\left(1 + \frac{Q^2}{W^2}\frac{1 - u^*}{1 + u^* + \eta}\right)\right] \qquad (2.31)$$

$$\frac{d\sigma_{TT}}{d\Omega^*} = \frac{\alpha^2}{W^2 + Q^2}\left[\frac{Q^2(1 - u^*)}{2(W^2 + Q^2)}\right], \qquad (2.32)$$

where

$$\eta = 2m_e^2 W^2/(W^2 + Q^2)^2. \qquad (2.33)$$

Notice, that the electron mass, m_e, is taken into account only where it is required in order to avoid a divergency in the formulas.

In order to specify $\sigma^{T,L}_{\gamma^* p}$ we shall consider various separate contributions depending on the value (range) of the m_X involved [60].

2.2.1.1 Elastic Contribution: $m_X = m_p$

$$\sigma^T_{\gamma^* p} = \frac{4\pi^2\alpha}{Q^2}G_M^2(Q^2)\frac{\delta(1-x)}{1-x}, \qquad (2.34)$$

$$\sigma^L_{\gamma^* p} = \frac{16\pi^2\alpha m_p^2}{Q^4}G_E^2(Q^2)\frac{\delta(1-x)}{1-x}, \qquad (2.35)$$

where α is the fine-structure constant and the conventional expressions of the proton's electromagnetic form factors were used:

$$G_E^2(Q^2) = \frac{G_M^2(Q^2)}{2.79} = \left(1 + \frac{Q^2}{Q_0^2}\right)^{-2} \qquad (2.36)$$

with $Q_0^2 = 0.71$ GeV^2.

2.2.1.2 Resonant contribution[4]: $m_p + m_\pi < m_X < 1.8$ GeV

In [11] is assumed that the range is to be saturated by the contribution of the three resonances $\Delta(1260)$, $N^*(1520)$, $N^*(1688)$. From the experimental data on electro-production, see e.g. [58], can be written:

$$\sigma^T = \sum_R \sigma_R\frac{m_R^2\Gamma_R^2}{(m_X^2 - m_R^2)^2 + m_R^2\Gamma_R^2\left(1 + \frac{Q^2}{Q_R^2}\right)^{-2}}, \qquad (2.37)$$

$$\sigma^L = 0 \ \mu b, \qquad (2.38)$$

where the values of the parameters m_R, σ_R, Γ_R, Q_R^2 are given in Tab. 2.2.

---

[4]Here m_π is a pion mass.

	Δ	N^*	N^*
$m_R(\text{GeV})$	1236	1520	1688
$\sigma_R(\mu\text{b})$	550	280	220
$\Gamma_R(\text{GeV})$	0.12	0.12	0.12
$Q^2_R(\text{GeV}^2)$	2.5	3.0	3.0

Tab. 2.2: Characteristics of the three resonances here considered.

2.2.1.3   Continuum Inelastic Contribution: $m_X > 1.8$ GeV

Following the discussion in [11], we treat separately the two regions in Q^2:

1. For large values of Q^2, with the assumption (justified by the quark-parton model) $\sigma_L = (Q^2/\nu^2)\sigma_T$, defining $\nu = Q^2/(2m_p x)$, one can get:

$$\sigma_T = \frac{4\pi^2\alpha}{(1-x)Q^2}F_2(x,Q^2),\qquad(2.39)$$

$$\sigma_L = \frac{4\pi^2\alpha}{(1-x)Q^2}\frac{4x^2m_p^2}{Q^2}F_2(x,Q^2),\qquad(2.40)$$

where $F_2(x,Q^2)$ is the proton structure function.

2. For Q^2 tending to zero one is led to the cross section of real-photon production:

$$\lim_{Q^2\to 0\ \text{GeV}^2}\sigma_T \simeq 100\,\mu\text{b},\qquad(2.41)$$

$$\sigma_L = 0\,\mu\text{b}.\qquad(2.42)$$

Finally, over the full Q^2 range is set:

$$\sigma_T = \frac{4\pi^2\alpha}{(1-x)Q^2}F_2(x,Q^2)\phi(x,Q^2),\qquad(2.43)$$

$$\sigma_L = \frac{4\pi^2\alpha}{(1-x)Q^2}\frac{4x^2m_p^2}{Q^2}F_2(x,Q^2)\phi(x,Q^2),\qquad(2.44)$$

where the interpolation function $\phi(x,Q^2)$ is defined as:

$$\phi(x,Q^2) = \frac{Q^2(\text{GeV}^2)}{Q^2(\text{GeV}^2) + F_2(x,Q^2)\,(1\,\text{GeV}^2)}\qquad(2.45)$$

noticing that with $Q^2 \to 0$ GeV^2

$$x \to 0,$$

while x/Q^2 stays finite and

$$\frac{4\pi^2\alpha}{(1\text{GeV}^2)} \simeq 100\,\mu\text{b}.$$

2.3   Kinematics of QED Compton Event

The kinematical relations which characterize the QED Compton process defined in Sec. 2.1.3 are reviewed[5].

- the coplanarity $\Delta\phi$ – absolute value of angle between the projection of the electron and the photon momentum in the xy-plane, i.e. to the plane orthogonal to the beam direction,

$$\Delta\phi = |\phi_e - \phi_\gamma|,\qquad(2.46)$$

- the four-momentum squared

$$Q^2 = -q^2,\qquad(2.47)$$

- the Bjorken scaling variable x

$$x = \frac{-Q^2}{2\,pq},\qquad(2.48)$$

- the scaling variable x_γ

$$x_\gamma = \frac{qk}{pk},\qquad(2.49)$$

- the invariant mass of the final hadronic system

$$W_h^2 = (p-q)^2 = m_p^2 - 2pq - Q^2,\qquad(2.50)$$

- the invariant mass of the $(e-\gamma)$ system

$$W^2 = (k+q)^2 = 4E_eE_\gamma - \left(1 - \frac{E_e}{xE_p}\right)Q^2,\qquad(2.51)$$

where E_e, E_γ, E_p is the energy of the incoming electron, photon and proton, respectively,

- the visible energy of the $(e-\gamma)$ system

$$E_{\text{vis}} = E_e + E_\gamma = E_e' + E_\gamma'\qquad(2.52)$$

- the transverse momentum of the $(e-\gamma)$ system

$$p_t^2 = |\vec{K}_\perp + \vec{k}_\perp|^2 = \left(1 - \frac{W^2 + Q^2}{sx}\right)Q^2\qquad(2.53)$$

---

[5]If not mentioned otherwise the variables are defined in laboratory frame.

- the velocity $\vec{\beta}$ of the center-of-mass of the $(e - \gamma)$ system in the laboratory frame

$$\vec{\beta} = \vec{\beta}_\| + \vec{\beta}_\perp == \frac{\vec{k} + \vec{q}}{E_e + E_\gamma} = \frac{\vec{K} + \vec{k}'}{E'_e + E'_\gamma}, \tag{2.54}$$

where $\vec{\beta}_\|$ and $\vec{\beta}_\perp$ are the longitudinal and transversal components of the $\vec{\beta}$ to the direction of incoming beams, respectively.

$$\beta_\| = |\vec{\beta}_\|| = \frac{\sin(\theta_e + \theta_\gamma)}{\sin\theta_e + \sin\theta_\gamma} \tag{2.55}$$

$$\beta_\perp = |\vec{\beta}_\perp| = \frac{|\vec{p}_t|}{E_{\text{vis}}} \tag{2.56}$$

According to the definition of the QED Compton process, see Sec. 2.1.3, the squared four-momentum transfered is close to zero, $Q^2 \to 0$ GeV^2. Due to Eq. (2.53) and (2.56), the squared transverse momentum of the $(e - \gamma)$ system and the transversal component of the velocity of the center of mass of the $(e - \gamma)$ system in the laboratory frame are negligible. Consequentially the scaling variable x is equal to one. Thus, the elastic channel is dominating and the kinematical formulae listed above are reduced:

$$W^2 = 4E_e E_\gamma \tag{2.57}$$

$$E_{\text{vis}} = E_e \left[1 + \left(\frac{W}{2E_e} \right)^2 \right] \tag{2.58}$$

$$\beta = |\vec{\beta}| = |\vec{\beta}_\|| = \frac{E_e - E_\gamma}{E_e + E_\gamma}, \tag{2.59}$$

and using Eq. (2.57) and Eq. (2.59) the invariant mass of the $(e - \gamma)$ system is given:

$$W \simeq 2E_e \sqrt{\frac{1 + \beta}{1 - \beta}} \tag{2.60}$$

Finally, for these elastic events characterized with $Q^2 \to 0$ GeV^2, i.e. when the quasi-real photon is emitted colinearly to the direction of the incoming proton, one can derive following formulae:

$$2E_e = E'_e(1 - \cos\theta_e) + E'_\gamma(1 - \cos\theta_\gamma) \tag{2.61}$$

$$E'_{e(\gamma)}(\theta_e, \theta_\gamma) = \frac{2E_e \sin\theta_{\gamma(e)}}{\sin\theta_e + \sin\theta_\gamma - \sin(\theta_e + \theta_\gamma)} \tag{2.62}$$

2.4   COMPTON - a Monte Carlo Generator

2.4.1   Description of COMPTON Monte Carlo Program

Since it is practically impossible to generate a reasonably accurate Monte Carlo program, which would be reasonably accurate in all phase space due to the presence of *various* poles in the expressions given in the previous section the solution to generate specific QED Compton events was chosen [11]. Those specific processes are those which are dominated by quasi-real photon exchange $q^2 \ll q'^2, q''^2$ with the final electron and photon nearly coplanar and observable at finite angle are meant. The consequence of the kinematical limitations of acoplanarity and polar acceptance of the scattered angles result in $Q^2 < W^2$ and $\eta \ll 1 + u^*$. Each single event is generated in the two following steps:

1. The event are generated according to an equivalent-photon-type approximation of the cross section given by formulas Eq. (2.29) to Eq. (2.32) where terms of order $\mathcal{O}(Q/W)$ are neglected. Consequently, η given by Eq. (2.33) is neglected as well.

   Since these are only dynamic approximations all kinematic / physical quantities are treated exactly during the generation performed over the phase space defined by the angular acceptances of the detector at the beginning of the program.

2. Already generated events are weighted by comparing the exact value of the differential cross section defined Eq. (2.20) to the approximate one used in the first step.

Despite this two-steps procedure providing an exact Monte Carlo simulation over the whole phase space available, the weights of the events become larger when increasing Q^2/W^2. This corresponds to moving from the "QED Compton" to the "radiative correction" configuration. Such large weight events are rejected due to the two following reasons:

1. Their statistical accuracy becomes small.

2. A limited increase of the cross section normalization should get a weight factor smaller than 1, and thus provide an output of individual (unweighted) events.

In order to select small values of Q^2/W^2 a cut on the $\Delta\phi$ angle between the transverse momenta of outgoing electron and photon, so-called acoplanarity angle, is defined. The elimination of large Q^2 values even at high W is controlled by introducing an additional cut on the transverse momenta. The restriction to relatively small Q^2 has two advantages: any contribution from weak interactions (i.e. virtual Z exchange) had not to be taken in to account; a scale-invariant expression of the photon's electromagnetic structure function cloud have been chosen [11], such as:

$$F_2(x) = 35/32 \sqrt{x}(1 - x)^3 + 0.2(1 - x)^7. \tag{2.63}$$

The most significant radiative corrections to the lowest-order diagrams in Fig. 2.1, which proceed via a contribution from radiation emitted by the incoming electron, see Fig. 2.2, are taken into account using so-called peaking approximation. This procedure is justified by the fact that the radiated photon and the scattered one are essentially emitted at different angles and thus can be distinguished, so that interference terms are suppressed.
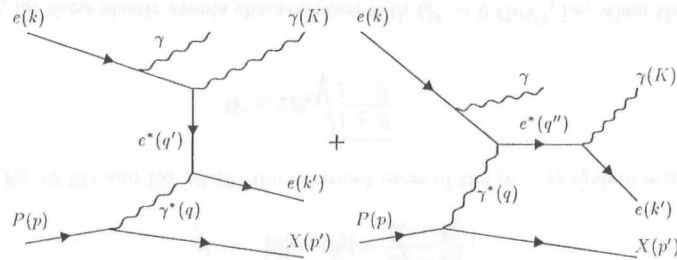
Fig. 2.2: The radiative correction on the incident electron line for the QED Compton process.

As the authors in [11] mentioned, despite the total outgoing hadron invariant mass being generated by the program, the possible hadron components inside the detector are not. As far as the elastic contribution is concerned, the outgoing proton does not enter the finite-angle detector. This feature sets limits for exploring the inelastic channel of QED Compton, where for the analysis the kinematical variables based on the measurement of $(e - \gamma)$ system could be only used [61].

The input values for the kinematical variables used for generating the Monte Carlo samples used in analysis presented here are summarized in the Tab. 2.3. For the gener-

kinematical variable		1994	1995
incoming electron energy	E_e	27.52 GeV	27.52 GeV
incoming proton energy	E_p	820 GeV	820 GeV
scattered electron energy	E'_e	> 2 GeV	> 2 GeV
scattered photon energy	E'_γ	> 2 GeV	> 2 GeV
visible energy	$E'_e + E'_\gamma$	> 20 GeV	> 20 GeV
polar angles	θ_e, θ_γ	$3.6° < \theta_{e'}, \theta_\gamma < 178°$	$3.6° < \theta_{e'}, \theta_\gamma < 178.5°$
coplanarity	$\pi - \Delta\phi$	< 45°	< 45°
transversal momentum	$|\vec{p}_t|$	< 20 GeV	< 20 GeV
simulation program	h1sim	version 3.06/41	version 3.06/45
reconstruction program	h1rec	version 6.04/01	version 7.17/00

Tab. 2.3: Input values of the kinematical variables.

ated events the detector response was simulated in detail [12] using a program based on GEANT [110]. The simulated Monte Carlo events were subjected to the same reconstruction and analysis chain as the real data.

2.4.2 COMPTON Monte Carlo Program Predictions

In the following the predictions of the distributions and correlations of the basic kinematical variables defined above are presented. In order to study the QED Compton process a sample of one hundred thousand events was generated using the COMPTON Monte Carlo program, see Sec. 2.4.1. The input values for the kinematical variables used in the 1995 data analysis, see Tab. 2.3, were used.

As it was discussed in previous section, the weight of generated events becomes larger for larger value of ratio Q^2/W^2, i.e. when moving from elastic to the inelastic channel. The correlation between the event weight and the ratio Q^2/W^2 is shown in Fig. 2.3. Experimentally, the cut on coplanarity has to be imposed in order to eliminate these events. In the following the contribution of the inelastic events[6] to the distributions is explicitly shown.
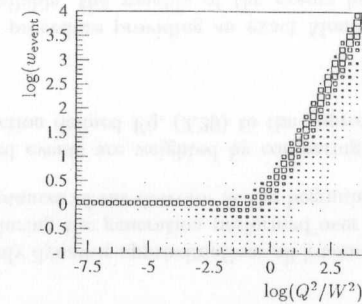
Fig. 2.3: The correlation between the event weight, $\log(w_{event})$, and the ratio $\log(Q^2/W^2)$ for the Monte Carlo QED Compton event sample produced using the COMPTON generator.

The distributions of the energy $E'_{e(\gamma)}$ and the polar angle $\theta_{e(\gamma)}$ of the scattered electron (photon) are shown in Fig. 2.4.

The correlation between the energy of the scattered electron E'_e and photon E'_γ, which is depicted in Fig. 2.5.a, shows a very strong correlation corresponding to the $E_{vis} = E'_e + E'_\gamma = E_e$. The events with a lower E_{vis}, are due to radiative correction. In Fig. 2.5.b, where correlation of the polar angle of the scattered electron, θ_e, and photon, θ_γ, is shown, one observes, that both the electron and photon (especially the later) tend to be emitted backwards, i.e. in the direction of the incident electron, in the laboratory frame. The full lines indicate the lower limit of the geometrical acceptance of the backward electromagnetic calorimeter, for description see Sec. 3.3.2 and 3.4.2.1. Although the finite detector resolution effect are not taken into account, it is shown that most of the events will be detected by the backward electromagnetic calorimeter.

The distributions of the acoplanarity $|\Delta\phi|$, shown in Fig. 2.6.a, shows a clear peak around 180° for all sample, while the inelastic contribution is homogeneously distributed.
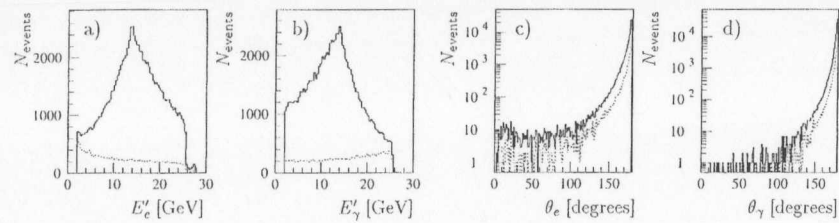
Fig. 2.4: The distributions of the energy (a, b) and the polar angle (c, d) of the scattered electron and photon for the Monte Carlo QED Compton event sample produced using the COMPTON generator. The full line stands for the all events the dotted line shows only the inelastic contribution.
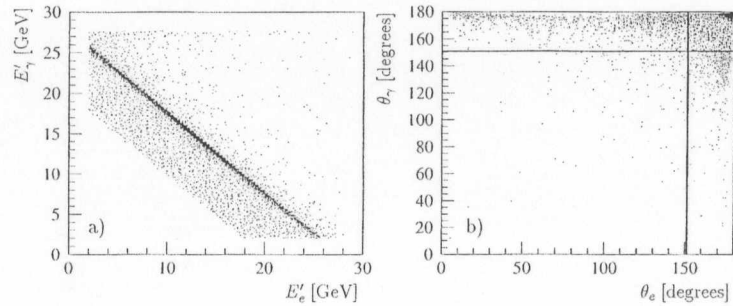
Fig. 2.5: The correlation between the energy (a) of the scattered electron E'_e and photon E'_γ and the polar angle (b) of the scattered electron θ_e and photon θ_γ for the Monte Carlo QED Compton event sample produced using the COMPTON generator. The full lines indicate the lower limit of the geometrical acceptance of the backward electromagnetic calorimeter.
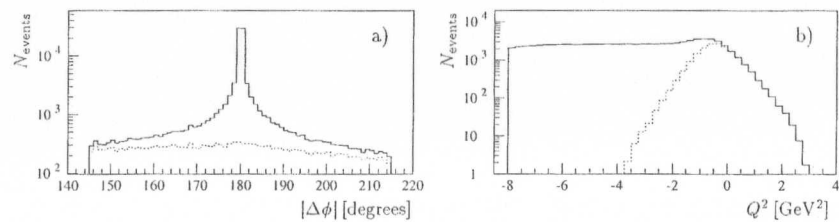
Fig. 2.6: The distributions of the acoplanarity (a) and the squared momentum transfered (b) for the Monte Carlo QED Compton event sample produced using the COMPTON generator. The full line stands for the all events the dotted line shows only the inelastic contribution.

In addition, from the distribution of the squared momentum transfered Q^2 see Fig. 2.6.b., one can see, that the inelastic events dominate at higher values of Q^2.

The distributions of the absolute value of the transversal momentum, shown in Fig. 2.7.a, is clearly peaked for the elastic channel towards at its minimum value, in contrary to the inelastic contribution. Finally, Fig. 2.7.b shows the distribution of the invariant mass of the $(e-\gamma)$ system, which is strongly decreasing with rising values of W for both the elastic and inelastic contribution.
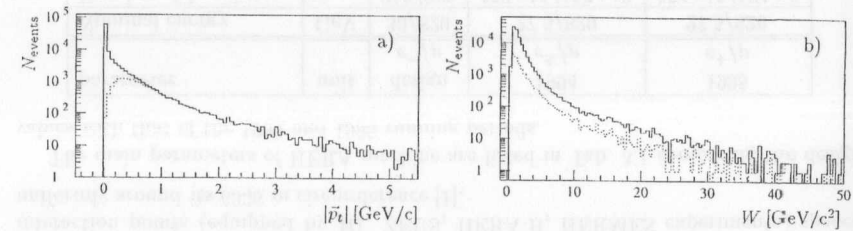
Fig. 2.7: The distributions of the absolute value of the transversal momentum (a) and the invariant mass of the $(e-\gamma)$ system (b) for the Monte Carlo QED Compton event sample produced using the COMPTON generator. The full line stands for the all events the dotted line shows only the inelastic contribution.

---

[6]Here the adjective "inelastic" for both resonant and inelastic contribution is used.

Chapter 3

H1 Detector at HERA

Whilst the first part of this chapter contains a brief description of the HERA accelerator the second is concerned with a review of the components of the H1 detector. The description of the H1 backward scattering region, which is mainly relevant for the presented analysis, is divided in two sections to follow its upgrade which was undertaken in order to provide the improved measurement of the scattered particles in the new kinematical region during the winter shutdown 1994/95.

3.1 HERA Accelerator

The electron-proton beam facility HERA, shown in Fig. 3.1 [17], consists of two independent accelerators designed to store 820 GeV protons and 30 GeV electrons (or positrons) respectively and to collide the two counter-rotating beams head on in four interaction points (equipped by H1, ZEUS, HERA-B, HERMES experiments) spaced uniformly around its 6336 m circumference [1].

The main parameters of HERA machine are listed in Tab. 3.1 comparing the design values with that of the 1994 and 1995 running periods.

parameter	unit	design e^-/p	1994 $e^\pm/p$	1995 e^+/p
Nominal energy	GeV	30/820	27.5/820	27.5/820
Number of bunches		210/210	153+15/153+17	174+15/174+6
Currents	mA	58/159	17.0/41.0	18.0/54.0
Bunch separation	ns	96	96	96
HERA int. luminosity	nb^{-1}	10^5	5590	10100
H1 gated luminosity	nb^{-1}	-	3983	5540
Circumference	m	6336		
Interaction points		4		

Tab. 3.1: HERA parameters.

At the beginning electrons (positrons) are pre-accelerated in the Linac II (450 MeV) which is used to fill the small storage ring PIA. The single e^- (e^+) bunches are injected
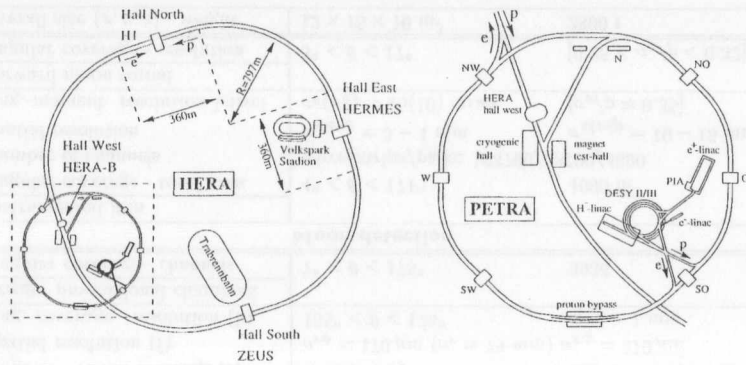
Fig. 3.1: The layout of HERA accelerating facilities.

into DESY II (7 GeV) and transfered to PETRA II (12 GeV) where they are stored, accelerated to the HERA injection energy (14 GeV) and transfered to HERA (27.5 GeV).

The proton injection starts with a negatively charged hydrogen ions linear accelerator H^--Linac III (310 GeV). After stripping off the two electrons, the protons are injected and accumulated into DESY III (7.5 GeV). The proton bunches are then transfered to PETRA II (40 GeV), and finally to the HERA (820 GeV).

3.2 H1 Detector

The H1 detector [12], is a a nearly hermetic multipurpose apparatus built to investigate the high-energy interactions of electrons and protons at HERA. The experimental program requires a detector having a good identification of electron, high degree of hermeticity, with a high granularity and excellent energy resolution, as well as the best possible hadron calorimeter. In addition a large solid angle tracking is demanded. The efficient use of all these components is provided by a sophisticated trigger and read out systems.

In the following, firstly a general overview of the H1 detector in the status of 1994 data taking is given which is later completed with the more detailed description of the backward scattering region for both 1994 and 1995 (i.e. upgraded) experimental configurations.

The main elements of the detector which parameters are summarized in Tab. 3.2, are shown in Fig. 3.2 along with the coordinate systems adopted in the H1 experiment.

3.2.1 Calorimetry

Since the H1 detector was designed to provide clear identification and precise measurement of electrons, muons and penetrating neutral particles together with a good performance
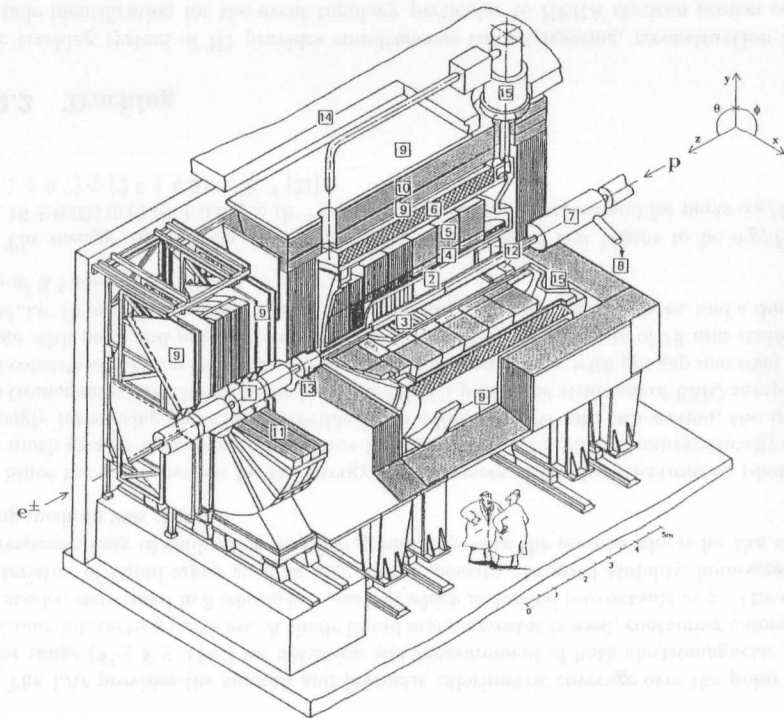
Fig. 3.2: The overall view of the H1 detector. Beam pipe and beam magnets (1), central tracking chambers (2), forward tracking and transition radiators (3), liquid argon electromagnetic (4) and hadronic (5) calorimeters, super-conducting coil (6), compensating magnet (7), helium cryogenics (8), muon chambers (9), instrumented iron (10), muon toroid magnet (11), backward electromagnetic calorimeter (12), plug calorimeter (13), concrete shielding (14), liquid argon cryostat (15).

Calorimetry		
LAr calorimeter	Electromagnetic part	Hadronic part
Granularity	10 to 100 cm^2	50 to 2000 cm^2
Depth (number of channels)	20 to 30 X_0 (30784)	4.7 to 7 λ_{abs} (13568)
Resolution $\sigma(E_{e,h})/E_{e,h}$	$\approx 11\%/\sqrt{E_e} \oplus 1\%$	$\approx 50\%/\sqrt{E_h} \oplus 2\%$
Stability of electronic calibration	$\leq 0.2\%$ over one month	
LAr purity (decrease of signal)	$\leq 0.2\%$ over one year	
Noise per channel	10 to 30 MeV	
Ang. coverage - dead channels	$4° < \theta < 153°$	$< 0.3\%$
BEMC: Pb-scintillator		
Angular coverage - granularity	$151° < \theta < 176°$	16×16 cm^2
Depth - resolution $\sigma(E_e)/E_e$	21.7 X_0 (1 λ_{abs})	$10\%/\sqrt{E_e} \oplus 1.7 [1]\%$
Tail catcher: iron-streamer tubes		
Angular coverage	$4° < \theta < 176°$	
Depth - resolution $\sigma(E_h)/E_h$	4.5 λ_{abs}	$100\%/\sqrt{E_h}$
PLUG calorimeter: Cu-Si		
Angular coverage - granularity	$0.7° < \theta < 3.3°$	5×5 cm^2
Depth - resolution $\sigma(E_h)/E_h$	4.25 λ (44.6 X_0)	$\approx 150\%/\sqrt{E_h}$
Electron tagger: Tl(Cl/Br)		
Angular coverage - granularity	$\theta > 179.7°$	2.2×2.2 cm^2
Depth - resolution $\sigma(E_e)/E_e$	21 X_0	$\approx 10\%/\sqrt{E_e} \oplus 1\%$
Tracking		
Coil: radius - field	3 m - $B = 1.15$ T, $\Delta B/B \leq 2\%$	
Central tracking		
Angular - radial coverage	$25° < \theta < 155°$	$150 < r < 850$ mm
Jet chamber: spatial resolution	$\sigma_{r\phi} = 170 \,\mu$m	$\sigma_z = 22.0$ mm
z-chambers: spatial resolution	$\sigma_{r\phi} = 25$ and 58 mm	$\sigma_z \approx 350 \,\mu$m
Momentum - dE/dx resolution	$\sigma_p/p^2 < 0.01 [0.003]$ GeV^{-1}	$\sigma(dE)/dE = 10 [6]\%$
Forward (f)/backward (b)		
Angular - radial coverage (f)	$7° < \theta < 25°$	$120 < r < 800$ mm
Spatial resolution (f)	$\sigma_{r\phi} = 170 \,\mu$m ($\sigma_r = 29$ mm)	$\sigma_{x,y} = 210 \,\mu$m
Ang. coverage - resolution (b)	$155° < \theta < 175°$	$\sigma_{x,y} = 1$ mm
Trigger proportional chambers		
Angular coverage - channels	$7° < \theta < 175°$	3936
Muon detection		
Instrumented iron		
Angular coverage - total area	$4° < \theta < 171°$	4000 m^2
Number of channels	wires/strips/pads: 103700/28700/4000	
Spatial resolution	$\sigma_{wire} = 3 - 4$ mm	$\sigma_{strip} = 10 - 15$ mm
Ang.-moment. resolution barrel	$\sigma_\theta (\sigma_\phi) = 15(10)$ mrad	$[\sigma_p/p \approx 0.35]$
Forward muon toroid		
Angular coverage - resolution	$3° < \theta < 17°$	$[0.25 < \sigma_p/p < 0.32]$
Overall size (x,y,z) - weight	$12 \times 15 \times 10$ m^3	2800 t

Tab. 3.2: Summary of H1 detector parameters. Alternatively, design and test beam figures are given in brackets. Energies are given in GeV.

in the measurement of jets with high particle densities, a calorimeter inside a large coil was chosen [16].

The H1 calorimeter is composed of four separate units. The liquid argon calorimeter (LAr) [21] is completed with a small copper-silicon sampling plug calorimeter (PLUG) covering the region between the beam pipe and the liquid argon cryostat ($\theta < 4°$) with an energy resolution $1.5/\sqrt{E}$ [12] and the lead-scintillator backward electromagnetic calorimeter (BEMC) (see Sec. 3.3.2 and 3.3.3).

The tail catcher (TC) as a part of muon system (see also Sec. 3.2.4), measures any hadronic energy leaking out the LAr and BEMC with an energy resolution $\sigma_E/E \simeq 1.0/\sqrt{E}$ [12].

The LAr provides the smooth and hermetic calorimetric coverage over the polar angular range ($4° \leq \theta \leq 154°$) for detection and measurement of both electromagnetic and hadronic interacting particles. A single liquid argon cryostat is used, containing calorimeter stacks, structured in 8 wheels in z, each of which is divided into octants in ϕ. The characteristics of liquid argon such as high atomic density, the good stability, homogeneity of response, easy of calibration and fine granularity were the reasons why it for the sampling medium was chosen.

Since the cross sections for the energy loss processes of incident electrons or photons are much greater than those for hadrons the separation between electromagnetically and strongly interacting particles is possible by dividing the LAr into two section, the inner electromagnetic (EMC) and outer hadronic (HAC) part. The structure of EMC sampling cell consists of 2.4 mm lead absorber and 2.35 mm liquid argon with per gap one read out plane with pads and one high voltage plane. The HAC cell consists of 19 mm stainless steel, i.e. 16 mm absorber and twice 1.5 mm independent read out cell plates, and a double gap of 2.4 mm liquid argon.

The energy distribution of LAr has beam measured in test beams to be $\sigma_E/E = (11.16 \pm 0.05) \oplus (0.64 \pm 0.07) \times 10^{-2}$ (with E in GeV) for electrons and for pions $\sigma_E/E = (46.1 \pm 0.7) \oplus (2.6 \pm 0.2) \times 10^{-2}$ [21].

3.2.2 Tracking

The tracking system of H1 provides simultaneous track triggering, reconstruction and particle identification for the event topology particular to HERA electron proton collisions [12].

In order to fullfil these tasks over the whole solid angle, the tracking system, shown in Fig. 3.3, was split into three physically separate components, i.e. the forward tracking detector (FTD), the central tracking detector (CTD) and the backward multi-wire proportional chamber (BPC).

The main components of the CTD are the two concentric drift chambers (CJC1 and CJC2). Both have wires strung parallel to the beam axes with the drift cell inclined by 30° with respect to the radial direction giving optimum track resolution with additional advantages such as easy resolving of chamber ambiguity by connecting different
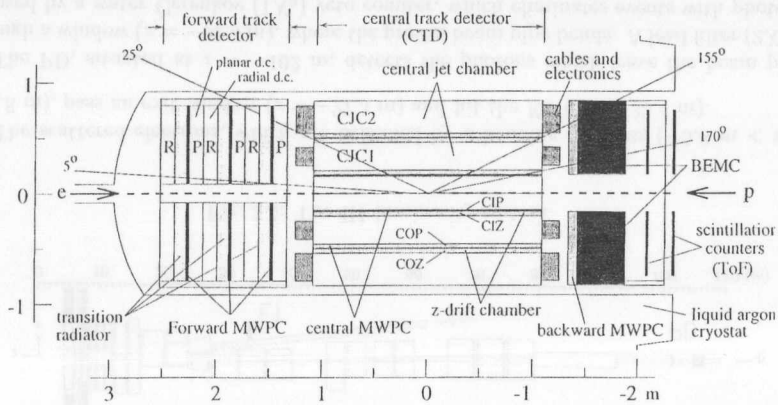
Fig. 3.3: An r-z projection of the H1 trackers.

cells track segments, suppression of obstruction of real tracks by wrong mirror track segments, easy separation of tracks coming from different bunch crossing (the passing time of a particle to an accuracy of ≈ 0.5 us can be determined, since each stiff track crosses more than one drift cell).

Two thin layers of drift chambers, with sense wires perpendicular to and drift direction parallel to the beam axis enhancing the z measurement of the charged tracks in central region [20]. As it is shown in Fig. 3.4 the central inner z-chamber (CIZ) is located inside CJC1, the central outer z-chamber fits in between CJC1 and CJC2.

For triggering on tracks coming from interaction point (IP) the CTD is equipped by two multi-wire proportional chambers, which both contain two concentric chambers with pad readout. The central inner proportional chamber (CIP) is the innermost component of the CTD and its outer partner, the (COP) is positioned between the COZ and CJC2.

The FTD is realized as three identical super-modules. Seen from the IP each super-module consist of planar wire drift chamber (PWDC), a forward multi-wire proportional chamber (FMWPC), transition radiator material and a radial wire drift chamber (RWDC).

The planar module consists of three drift chambers each four wires plane deep in z and oriented $0°$, $+60°$ and $-60°$to the vertical. In order to maximize the geometrical trigger efficiency of the FTD and for practical reasons such as sharing the same gas mixture the FMWPC is mounted directly behind the PWDC. The FMWPC is followed by transition radiator consisting of 400 polypropylene foils contained in its own gas volume. The RWDC consists of 12 planes each containing 48 radially strung wires. The interleaving of the PWDC and RWDC improves the momentum measurement. The track finding and fitting procedure is fully discussed in [25].

In the backward direction the BPC (see Sec. 3.3.1), offers accurate spatial reconstruction and additional fast triggering information on charged particles.
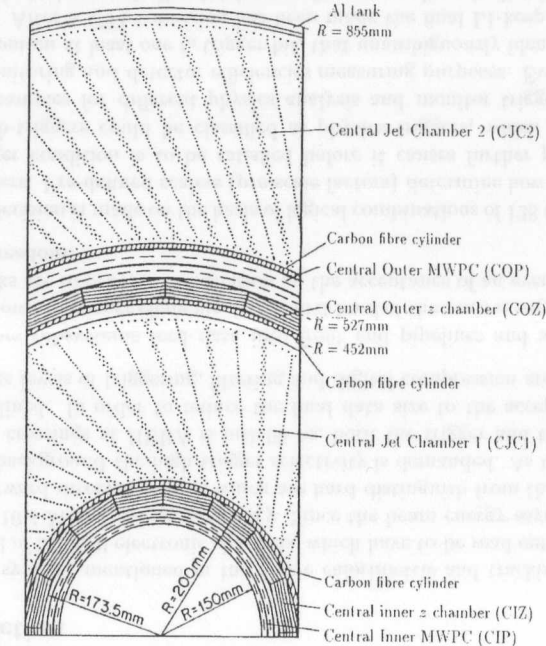
Fig. 3.4: A section through the central tracking system, perpendicular to the beam. The drift cells are tilted at an angle of 30°to the radial direction. The CJC wires are parallel to the beam.

3.2.3 Scintillators

Different scintillator based detectors providing a good timing resolution for the removal of background at first level trigger are used. In the 1994 data taking period the time of flight system (ToF), described in Sec. 3.3.4, was combined by its forward counterpart (FToF).

The FToF is a pair of scintillators with a cross section of 200×600 mm² separated by 7.5 mm lead sheet read out by two standard photo-multiplier tubes and installed perpendicular to the beam axis between muon toroid and the first forward muon layer ($z = 7$ m). Since it lies 50 mm from the beam axis, its primary task is the detection secondary scattering from the proton remnant, beam gas, beam wall or an ep collision [22].

In order to remove from proton-beam induced hard penetrating background particles two double scintillator veto walls are installed at a distance of 6.5 and 8.1 m, respectively, upstream from the IP.

3.2.4   Muon System

The iron yoke of the main solenoid magnet, which surrounds all major sub-detectors of H1, is instrumented with limited streamer tubes (LST). It provides the identification and tracking of penetrating muons and using eleven of the sixteen limited streamer tube with read out pads of size and $50 \text{cm} \times 40 \text{cm}$ and $28 \text{cm} \times 28 \text{cm}$ in the barrel and end-caps, respectively, serves as a tail catcher for the LAr calorimeter and BEMC.

In the forward direction the instrumented iron detection is supported by forward muon detector (FMD) giving an independent muon momentum measurement in the range $5 \leq p \leq 200$ GeV/c, with the angular range $3° \leq \theta \leq 17°$. The FMD consists of an additional toroidal magnet sandwiched by three layers of drift cells, which are 200 mm deep and 120 mm wide.

3.2.5   Luminosity System

The tasks of H1 luminosity system are fast relative luminosity measurement, electron beam monitoring for the HERA machine, absolute luminosity measurement in the interaction region, tagging of quasi-real photoproduction events with $Q^2 < 0.01$ GeV^2 and energy measurement of electrons scattered under small angles and for photons emitted collinearly to the incoming electron [12].

Since the luminosity system, see Fig. 3.5, detects scattered electrons and outgoing photons in coincide, it contains two arms: the electron tagger (ET) and the photon detector (PD).
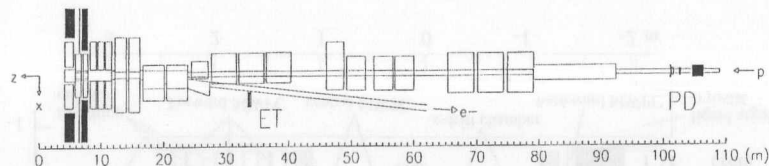
Fig. 3.5: The H1 luminosity system.

The scattered electrons, which are deflected by a bending magnets (-5.8 m $< z <$ -23.8 m), pass an exit window ($z = -27.3$ m) and hit the ET ($z = -33.4$ m).

The PD, situated at $z = -102$ m, detects the photons which leave the beam pipe through a window ($z = -92.3$ m), where the proton beam pipe bends. A lead filter $(2X_0)^1$ followed by a water Čerenkov $(1X_0)$ veto counter, which eliminates events with photons interacting with the filter, protects the PD calorimeter from the synchrotron radiation. During the injection both the ET and PD are moved from the median plane of electron beam.

---

[1] X_0 stands for radiation length.

The ET as well as PD calorimeters are crystal Čerenkov counters, made of a 7×7 array of 154 mm $\times 154$ mm and a 5×5 array of 100 mm $\times 100$ mm crystals, respectively, which are read out by photo-multipliers. They have an energy resolution of $\sigma_E/E = 0.1/\sqrt{E} \oplus 0.01$ and a spatial resolution less than 1 mm.

The method of luminosity measurement based on the detection of bremsstrahlung reaction $ep \rightarrow ep\gamma$ is described in Sec. 6.3.

3.2.6   Slow Control

The slow control (SC) of H1 is designed to take care of different parameters of the experiment. All sub-detectors described above are equipped with a SC system, which uses VME crates controlled by Macintosh, OS-9 computers, or a VME-controlled multi-channel SC system [12]. The subsystems are integrated either by a simple alarm system, or by a computer control network. The SC data are maintained by a rational database management system.

3.2.7   Triggering, Data Acquisition and Off-line Data Reconstruction

The electronic systems mentioned in the above calorimetric and tracking sub-detectors produce in total of 270,000 electronic channels, which have to be read out with additional constraint of a 10.4 MHz collision frequency. Since the beam energy asymmetry leads to the strongly forward directed events, which are hard distinguish from the intense proton beam induced background the high trigger selectivity is demanded. As the time interval between bunch crossings at HERA is just 96 ns, both the trigger and the readout data had to be pipelined. In order to reduce the final data size to the acceptable recording rates the various levels of triggering, filtering and digital compression are employed.

The detectors subsystems feed data into front end pipelines and send fast trigger information, known as trigger elements, to the first level of the central trigger (CTL1) [27], which main tasks are to provide the decision on the acceptance of an event and to control the subsystem readout.

The CTL1 decision is made on the basis of logical combinations of 128 trigger elements, called sub-triggers. Pre-defined scalers (pre-scale factors) determine how many times the single sub-trigger condition is to be satisfied before it causes further processing of an event. The sub-triggers could be classified as physics triggers, which are constructed for extracting samples for different physics analysis and monitor triggers designed for background monitoring and detector efficiencies measuring purposes. Every physics sub-trigger has to contain at least one t_0 trigger bit, that unambiguously identifies the correct bunch crossing. After a CTL1 decision has been made the final L1-keep signal, which is defined by the logical sum of all sub-triggers after pre-scaling, is distributed to the all subsystems front end electronics.

When a positive L1-keep signal is returned by CTL1 all pipelines are stopped and the contained data are processed. At this point the accumulation of the primary dead

time (PDT) is started. During it the two intermediate trigger levels 2 and 3 using the sub-triggers derived in the level 1 system can operate. For the level 2 trigger, which provides a signal after 20 μs, the complex topological correlator [29] and a neural network approach have been developed [30]. If the event is accepted at level 2 the time consuming readout tasks are initiated and the level 3 system with the software algorithm's running on a RISC microprocessor can potentially abort the readout [31]. Its decision time is less then 800 μs.

The front end processed and compressed data are placed in multi-event buffers and from each subsystem collected by a dedicated processor, the event builder (EB). For the data transfer an optical fiber ring is used [33]. The PDT ends when the EB assembles the full event and the front end pipelines are released again. The primary readout of one single event takes about 1-2 ms.

From the EB events are passed to the level 4 trigger (L4), i.e. to a software filter farm based on thirty-two RISC processor boards run in parallel. Performing a limited reconstruction and using specifically designed fast algorithms each board processes one event is processed until a decision is made. A small fraction (1 %) of all L4 rejected events is kept for monitoring purposes.

The final event records are sent to the SGI Challenge computer some 3 km distant [32], and via SCSI interface stored by an Ampex DST800 tape robot.

In the off-line reconstruction procedure the full reconstruction of all H1 sub-detectors is followed by the linking of charged particles track segments and the energy clusters and thus results in the final overall event picture. The data filtering chain is finished by the level five trigger (L5), where the events are classified according to various selection procedures mirroring the request of various physics working groups. At this level the data containing the full information are stored on tapes in the physics output tape (POT) format. In order to offer the simultaneous access for further physics analyses the data are finally compressed to the data summary tape (DST) format and written to the discs.

3.3   Backward Part of the H1 Detector

The primary tasks of the sub-detectors placed in the backward scattering region of the H1 detector, see Fig. 3.6 [24], are triggering on electrons, measuring their energy and position, contributing to the reconstruction of hadronic final states emerging either from DIS (at low values of x) or photoproduction processes, and suppression of proton induced background.

In this section the parameters and characteristics of the backward tracker, calorimeter, its electron trigger and the time of flight system used untill the 1994/95 shutdown, when the backward scattering region was upgraded, are summarized in more detail.

3.3.1   Backward Proportional Chamber

The backward multi-wire proportional chamber (BPC), which was mounted directly on the backward electromagnetic calorimeter front face was supporting the CTD in the region
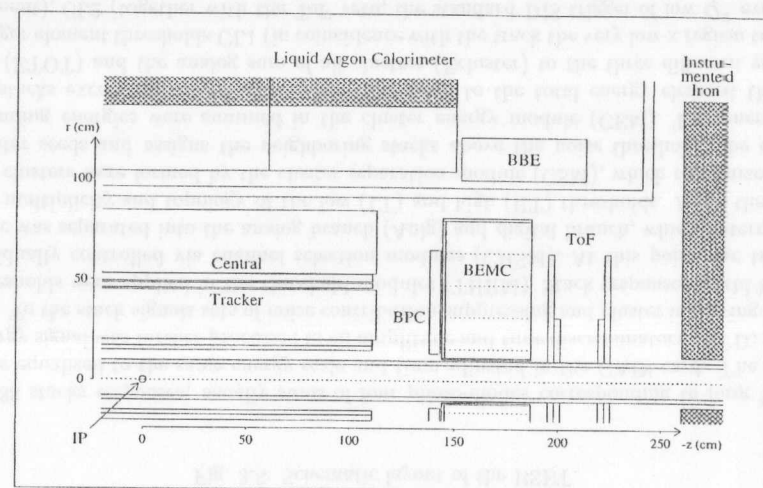
Fig. 3.6: Longitudinal view of the backward region of H1 detector.

where its ability to reconstruct tracks was either limited ($\theta > 154°$) or just impossible (the CIZ and CIP lower acceptance boundary, $\theta > 170°$).

The BPC was equipped with five graphited cathode planes and four anode wire planes providing the active region from an inner radius of 135 mm to 650 mm, which corresponded to the angular coverage $155.5° < \theta < 174.5°$ [12]. Since the anode wires were read out and the wire orientations were different for each wire plane (vertical, horizontal and $\pm 45°$) the combined information of the four planes allows an accurate spatial reconstruction with a space resolution of $\sigma_{x,y} \approx 1.5$ mm which corresponded to an angular resolution of ≈ 0.5 mrad for the particle arising from the nominal IP. The measurement of the impact position of charged particles hitting the BEMC was important for improving the BEMC energy measurement. Both the correction for the passive material of approximately 1 X_0 in front of BPC/BEMC system, known as dead material corrections, and the correction for particles which were depositing energy in between the BEMC stacks, called crack correction, which were calculated in the off-line event reconstruction, were position dependent.

3.3.2   Backward Electromagnetic Calorimeter

The BEMC in mounted inside the H1 solenoid coil at a distance of $z = -144$ cm from the interaction point. It covers polar angles θ in the range $151° < \theta < 176°$ and gave the full azimuthal coverage.

The BEMC consisted of 88 calorimeter modules, so-called stacks, which were arranged in 10 rows and 10 columns and mounted inside the aluminum barrel with a radial range $10.8 \leq r \leq 81.1$cm.

56 of the 88 stacks had a square cross section of 15.9 cm × 15.9 cm. The cross sections of the remaining 32 stacks were chosen to be trapezoid or triangular so that the outer and inner regions of the barrel were instrumented in the most effective way. Viewed from the H1 interaction point each stack (Fig. 3.7) consists of an 8 mm thick aluminum front plate with a pin on top, a first 4 mm scintillator plate followed by 49 sampling layers composed of 2.5 mm lead ($PbSb_6$), 0.2 mm paper, 4 mm scintillator and 0.2 mm paper provided up to 21.7 radiation lengths X_0. In order to improve the homogeneity of the optical response the paper sheets with the stack dependent grey pattern were used. The 8 mm aluminum end plate followed by the electronics housing fixed the sampling structure inside stainless steel boxes.
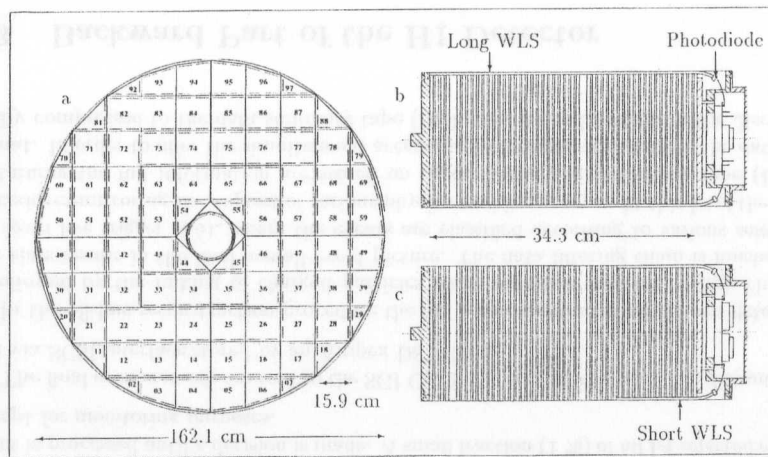
Fig. 3.7: Transverse view of the BEMC barrel (with the numbering scheme) and longitudinal cross sections of BEMC stacks. The eight trigger big towers by white and shaded areas were indicated and the positions of all long WLS in the whole BEMC (a), and the long (b) and short (c) WLS bars arrangement in BEMC square and trapezoid stacks are shown.

The SCSN-38 [19] scintillation light was shifted by dye to the blue region and read out via Y-7 [19] wavelength shifters (WLS). Whilst two pairs of long WLS bars cover two opposite sides of a BEMC stack, the light signal of last 15 sampling layers of all square and large trapezoid stacks was read out by short WLS bars which were twice as broad as the long ones. Each WLS was covered by white reflecting paper to achieve a better optical response. The photo-diodes glued to the end face of each WLS receive the light emitted by the WLS.

Each pair of long WLS and each short WLS as well was assigned to one electronic channel. In total there were 472 readout channels.

A nitrogen laser monitoring system producing light pulses for test purposes was developed and installed [23].

3.3.3 BEMC Single Electron Trigger

The basic function of the BEMC single electron trigger (BSET), Fig. 3.8, was to select events with localized energy depositions in the BEMC stacks [28, 24]. Therefore for building the trigger quantities the lowest granularity (individual stacks) was used.
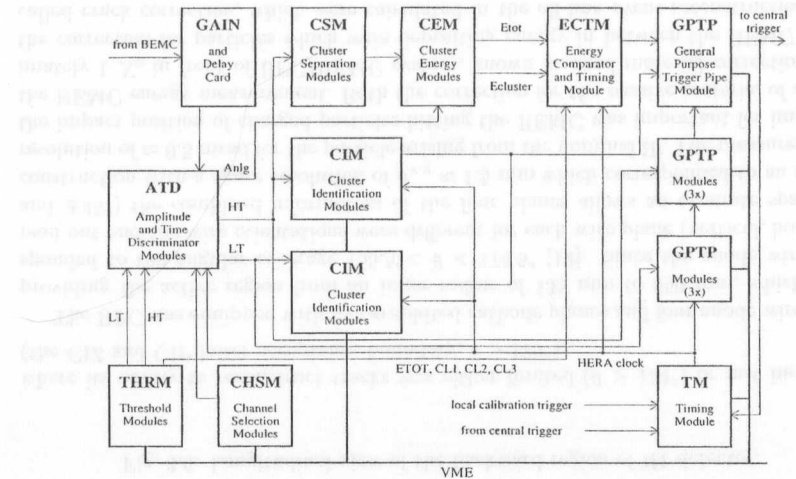
Fig. 3.8: Schematic layout of the BSET.

88 stacks responses, usually sums of four photo-diodes corresponding to long WLS, were equalized to the same energy scale and time adjusted in the GAIN card. The stack energy signal was further processed in an amplitude and time discriminatory (ATD) module. To the stack signals sets of noise contribution suppressing and cluster initiating stack thresholds were applied in the threshold modules (THRM). Stack responses could be individually controlled via channel selection modules (CHSM). At this point the trigger logic was separated into the analog branch (Anlg) and digital branch, which determined the multiplicity and topology of the low (LT) and high (HT) thresholds. After the trigger clusters were formed by the cluster separation module (CSM), which recognized the cluster seeds and assigns the neighboring stacks above the noise threshold, the corresponding energies were summed in the cluster energy module (CEM). The energy of all stacks exceeding the LT (Etot) was compared to the total energy element threshold (ETOT) and the analog sum of all clusters (Ecluster) to the three different energy trigger element thresholds CL1 (in coincidence with the track the very low-x region trigger element), CL2 (together with the ToF veto, the standard DIS trigger of low Q^2 events), and CL3 (high-x region trigger for BEMC calibration and ToF monitoring purposes).

The programmable look-up tables of the cluster identification modules (CIM) provided cluster multiplicity trigger elements.

In total 189 bits were fed into the digital shift register module (GPTP) [26]. In order to keep the possibility of identifying possible pile-up events and simultaneously minimize the volume of data a readout of the nominal bunch crossing and two bunch crossings before and after was chosen.

At the input to the H1 central trigger the BEMC trigger response according by the slowest trigger elements entering the CTL1 was delayed.

Since the sensitivity of the photo-diodes to the passage of particles directly through their depletion layer was recognized (so-called nuclear counter effect) the additional comparison of energy depositions in the individual photo-diodes after noise suppression with a sufficiently high energy threshold was used to suppress this type of fake trigger, for more detailed study of this effect see Chapter 4.

3.3.4   Time of Flight System

The time of flight hodoscope (ToF), see Fig. 3.6, consisted of two walls made up of a sandwich of 30 mm thick scintillator and the 6.5 mm synchrotron radiation absorbing lead sheets. The plane nearest to the IP lied at $z = -1.95$ m and had 16 counter, each matching the size of four BEMC stacks. Eight larger planes form the outer plane located at $z = -2.25$ m. In order to operate inside a 1.14 T magnetic field, the ToF utilizes 24 high field photo-multiplier tubes (PM), which were housed in non-magnetic holders perpendicular to the ToF planes. Pre-amplified PM's signals were discriminated and strobed in three predefined time windows: background, interaction and global before being sent and used in the CTL1 decision.

In order to remove proton-beam induced hard penetrating background particles two additional double scintillator veto walls were installed at a distance of 6.5 and 8.1 m, respectively, upstream from the IP.

3.4   Upgraded H1 Backward Region

In order to lower the systematic errors which dominated the 1994 low x data analyses the H1 collaboration undertook an extensive upgrade program by constructing a new detectors: central (CST) and backward (BST) silicon trackers, backward planar drift chamber (BDC), and lead/scintillating-fibre calorimeter (SPACAL), see Fig 3.9.

In this section the BDC and the SPACAL detector together with its inclusive electron trigger are described. The description of the silicon trackers can be found in [46, 45].

3.4.1   Backward Drift Chamber

The backward drift chamber, which covers the front face of electromagnetic section of SPACAL, consists of four octagonal layers, each containing two half plates of drift chambers perpendicular to the beam axis. For a good polar angle resolution the anode wires are arranged like the strings in cobweb describing its concentric circles. In the two planes
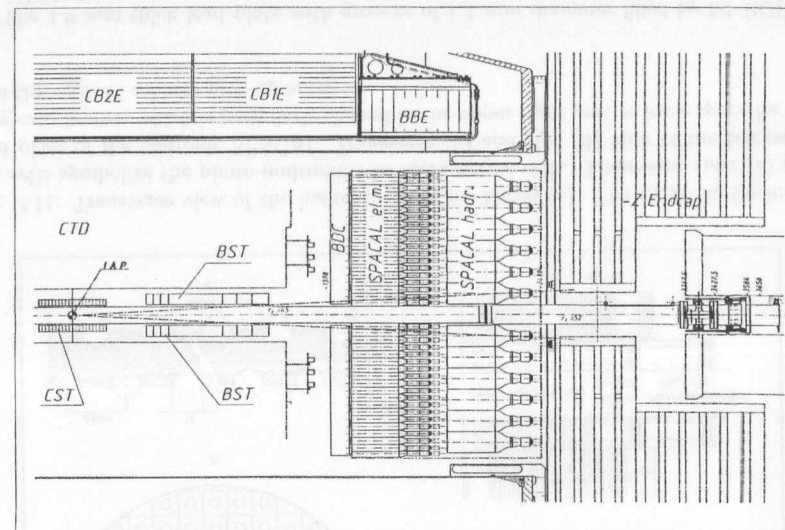
Fig. 3.9: Longitudinal view of the upgraded backward region of H1 detector.

of one layer the anodes are stretched parallel but shifted against each other by one drift space in radial direction. The four layers are turned one by one with an azimuthal angle of 18°. This minimizes the effect of dead areas and guarantees that each track is measured by at least six out of eight possible hits, which results to an angular resolution of better than 0.5 mrad, and a double track resolution of 3 mm [37].

3.4.2   Lead/Scintillating-Fibre Calorimeter

The lead/scintillating-fibre calorimeter consists of two separate sections, an inner electromagnetic and outer hadronic section. The hadronic section is completed by the backward plug calorimeter which is located in the iron return yoke. The separation into two calorimeters allows optimization of the electromagnetic energy resolution whilst maintaining coverage of hadronic particles and longitudinal segmentation [10].

3.4.2.1   Electromagnetic Section

The electromagnetic section of SPACAL detector consists of sixty 16-cell modules, formed by 2-cell modules each, see Fig 3.10. The 16-cell module cross section is 16.26 cm × 16.26 cm. The 2-cell module consists of a stack of 52 lead plates equipped with 90 fibres, see Fig. 3.10.c,d. The fibre ends form 70 mm long fibre bundles ending in an aluminum collar. The cross section of each cell is 40.5×40.5 mm^2. The 2-cell modules within 16-cell module are oriented with their lead plates running either horizontally or vertically depending on the 16-cell modules' detector position. The orientation is chosen to minimize

the signal dependence on the particle's impact position caused by the lead/fibre structure, so-called "channeling", which leads to a reduced energy resolution [38].

The innermost module of the electromagnetic calorimeter is called the insert module. Its cells are not rectangularly shaped in order to allow for the space needed for the beam pipe, see Fig. 3.10b. The four inner cells surrounding the beam pipe, the veto layer cells, are 8 mm thick. They are installed to identify the beam-gas and beam-wall background and to detect the energy leakage of the neighboring cells into the beam pipe. A 2 mm thick tantalum layer protects the active detector elements from synchrotron radiation.
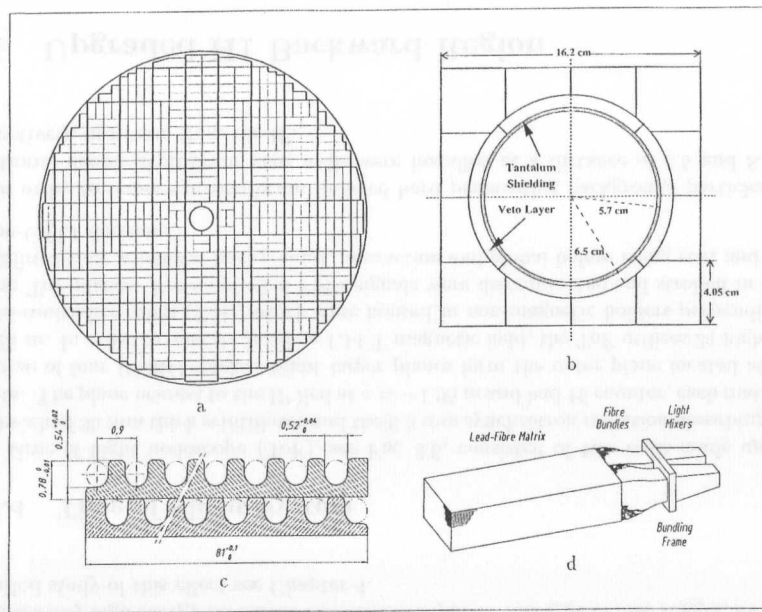
Fig. 3.10: Transverse view of the electromagnetic SPACAL barrel (a). The borders of the 16-cell modules are given by bold lines. The arrangement of the 2-cell modules is indicated by thin lines. The transverse view of the insert module (b). The cross section of two lead plates of the electromagnetic SPACAL (c). 2-cell module showing lead-fibre matrix, fibre bundles and light mixers (d).

The fibre diameter is 0.5 mm, with a lead to fibre ratio of 2.3:1 by volume. Due to the small fibre diameter a high sampling frequency is obtained, which results in an energy resolution with a sampling term close to $7\%/\sqrt{E(\text{GeV})}$ [39]. The active volume of the electromagnetic calorimeter is 250 mm deep, corresponding to a 28 radiation lengths. The high granularity is well matched to the Molièr radius of 25.5 mm to ensure good spatial resolution and electron pion separation.

The scintillation light is read out by photo-multipliers to achieve 1 ns time resolution and low noise level. The Hamamatsu R2490-06 fine-mesh photo-multipliers [40] capable operating within a strong magnetic field were chosen.

3.4.2.2 Hadronic Section and Backward Plug Calorimeter

The hadronic section of SPACAL calorimeter consists of 136 detector modules surrounding the beam pipe. The cross section of the 120 square modules is 119.3×119.0 mm^2. The remaining 16 edge modules are specially shaped in order to instrument the aluminium barrel of circular shape which holds the whole calorimeter in most effective way, see Fig. 3.11.a.
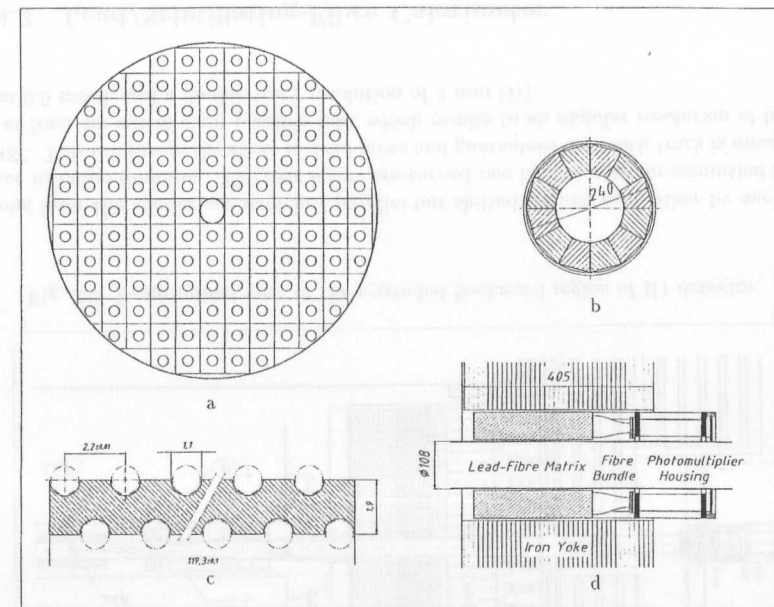
Fig. 3.11: Transverse view of the hadronic SPACAL barrel (a). The small circles inside the cells symbolize the photo-multipliers to mark active cells. Transverse view (c) of a lead plate of the hadronic SPACAL. Transverse (b) and side (d) view of the backward plug calorimeter, which is irregularly shaped in the upper right part to leave space for the feed-throughs of a beam pick-up antenna.

The 1.9 mm thick lead plate with grooves of 1.1 mm diameter filled by 54 BCF-12 fibres [42] of 1 mm diameter is shown 3.11.c. A module contains in total 3510 fibres, which are bundled and held by an aluminium frame. Each fibre bundle is coupled via an 80 mm long acrylic light mixer to a 2 inch photo-multiplier.

The fibre diameter for the hadronic calorimeter is 1 mm and the lead fibre ratio is 3.4:1 by volume. The hadronic section of SPACAL detector adds 1.02 interaction lengths of material to the electromagnetic section, which is 1.0 interaction lengths deep. Again the mash type photo-multipliers were used.

The angular coverage of the SPACAL calorimeter near the beam pipe is extended additional backward plug lead/scintillating-fibre calorimeter situated in the iron return yoke, see 3.11.b,d. Since the backward plug calorimeter was installed after the 1995 data taking it was not used in this analysis.

3.4.3 SPACAL Inclusive Electron Trigger

The SPACAL Inclusive Electron Trigger (IET), see Fig. 3.12, is designed to compare the deposited energy inside a group of 4×4 electromagnetic SPACAL towers with each of three thresholds [44].
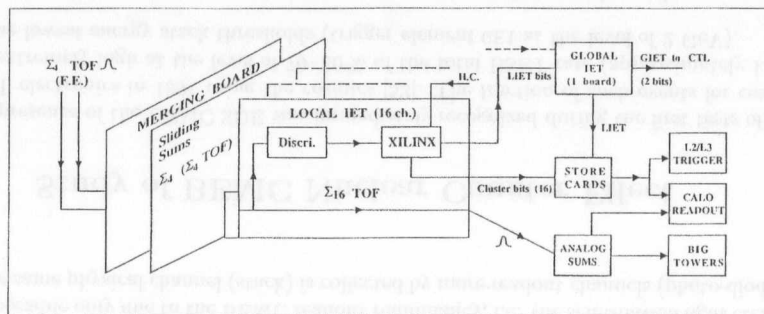
Fig. 3.12: Schematic layout of a IET trigger card.

The analog pulses from front-end cards are transmitted to the IET per groups of 16 trigger elements through multi-twisted-pair shielded cables, which are dispatched from the merging board to the sliding window (SW) board. The SW board receives the differential pulses with a gain unity and performes the analog sliding sums. According to the comparison of the amplitude of the trigger tower pulse with the three thresholds and the synchronization of the discriminator outputs three so-called "cluster bits" are generated in the local IET (LIET) card, which is plugged in the SW board. The LIET bits are sent to the global IET card (GIET), where for each threshold the logical sum of the LIET bits is performed resulting in the three GIET trigger bits. These are afterwards encoded in two bits, which are sent to the CTL1.

In addition the LIET provides analog sum outputs for time-of-flight calculations and makes available the the cluster bits for L2/L3 trigger.

Chapter 4

BEMC Nuclear Counter Effect

The photo-diode calorimeter readout has some advantages, such as the excellent short and long term stability, no need for magnetic shielding and high voltage, in comparison with the more conventional photo-multiplier readout. On the other hand photo-diodes have no internal amplification, which necessitates very low noise charge sensitive pre-amplifiers with a field effect transistor (FET) input stage. In addition photo-diodes have a very thin depletion layer resulting in a high source capacitance, which is one of the main contributions to the noise. Large area photo-diodes have substantial leakage currents contributing to the noise, too.

As it was described before the BEMC utilize 600 silicon photo-diodes in combination with wavelength shifters (WLS) to read out 88 lead-scintillator shower counters (stacks) [24]. Signals of the 344 photo-diodes corresponding to the full longitudinal readout of the stacks are summed (mostly 4 channels) to provide 88 stack inputs of the BSET [28]. Silicon PIN photo-diodes type Hamamatsu S2575 are used in the BEMC. The junction capacitance is 80 pF for a 30 V bias-voltage applied. The maximum dark current is 5 nA at 30 V bias-voltage and the temperature of 25°C. The dark current increases with rising temperature by a factor of 1.15/°C [48].

Already in the first studies of the photo-diode readouts [49], the sensitivity of the photo-diodes to the passage of the charged particles directly through the depletion layer of the photo-diode was recognized. This effect is in literature usually refereed as *nuclear counter effect* or *semiconductor effect*[1]. In the conclusion of [49] the protection of the photo-diodes from high background particle fluxes was stated. In the back region of the BEMC, i.e. near the photo-diodes, the WLS, which are longer than the covered sampling structure, are slightly bent to the center of the stack in order to reduce the direct semiconductor effects in the photo-diodes produced by particles originating from the IP and penetrating trough the cracks between the stacks. There is no protection at all for the significantly more intensive flux of particles from the backside (beam-gas and beam-wall interaction) and as our experience clearly shows for the direct and scattered synchrotron radiation.

Total number of $(e + e_{\text{pilot}})/(p + p_{\text{pilot}})$-bunches filled in HERA during the 1994 luminosity period was increased from $(84 + 10)/(84 + 6)$ to $(153 + 15)/(153 + 17)$ with

---

[1]Inside the H1 collaboration is this effect usually refereed as single diode event (SDE), reflecting the fact that only one of four readout photo-diodes was affected.

respect to 1993 luminosity period. Therefore at least partial suppression of the BEMC nuclear counter effect at the level L1 trigger was mandatory for sub-triggers containing BSET trigger elements. Special attention was required for the low Q^2 neutral current DIS events sub-trigger, which was composed of the stand-alone BEMC trigger element with a medium threshold CL2 and the ToF veto, used by H1 experiment as the standard DIS trigger during the first three years of its operation. Since the selection of the BEMC QED Compton event is based on the standard DIS trigger as well, as it will be discussed in Sec. 5.2.1, this chapter is devoted to the study of the BEMC nuclear counter effect as a source of the fake electron trigger signals.

The aim for 1994 luminosity period was to reduce the fraction of BEMC SDE events with both installing passive lead shielding and by their active hardware recognition already at the L1 trigger level at least for the most affected (inner) BEMC stacks.

Note, that the recognition of such a type of the events at the early stage of triggering was possible only due to the BEMC readout redundancy, i.e. the scintillation light created in the same physical channel (stack) is collected by more readout channels (photo-diodes).

4.1   Study of BEMC Nuclear Counter Effect

The presence of the BEMC SDE was immediately recognized during the first tests of the BSET electronics in 1991 using the cosmics [52]. The fraction of such events for cosmic was extremely high at the level of 70-80 % of the total BSET rate (approximately 1 Hz) for the lowest energy stack thresholds (trigger element GE1 at the level of 2 GeV).

In the HERA environment the three main sources of these spurious triggers are possible:

• intensive mainly charged particle flux originating from the proton induced background (beam-gas and beam-wall interaction);

• direct and scattered synchrotron radiation;

• due to the bending of the WLS quite small, but for the physics analysis most important fraction of the rest shower particles originating from the interaction point.

The L4 trigger level rejects the BEMC SDE after the full reconstruction of the BEMC energy depositions. Event was rejected only if no other sub-trigger besides the BSET sub-triggers (i.e. sub-triggers #0 → #12) was accepted. In order to monitor the L4 performance generally 1 % of the rejected events are kept. The sample of the L4 rejected events was reconstructed using the standard reconstruction program and stored on the separated tapes.

For the study of the BEMC SDE five data samples in 1993 luminosity data taking were selected. Tab. 4.1 defines the run periods and presents the number of BEMC SDE events collecting during them.

Data	Run period		Number of	Comments
sample	from	to	events	
1	55863	57115	5246	
2	61398	62663	11668	Up to run 62575 no field
3	64138	64474	1723	Collimator C3 opened
4	65458	65964	5401	
5	66306	66440	2314	Vertex shifted

Tab. 4.1: Selected run periods.

The composition of the accepted sub-triggers for the SDE events in the above indicated periods, see Fig. 4.1.a verifies the presence of only BSET sub-triggers, whereas the composition of the raw sub-trigger, in Fig. 4.1.b besides the proper predefined down-scaling for all sub-triggers indicates the substantial fraction of events with the ToF (#96, 98, 101 → 103), central and partly also forward trackers (#36, 38, 39, 41, 100, 104 → 113) and some fraction of the LAr (#114, 115) monitoring sub-triggers.
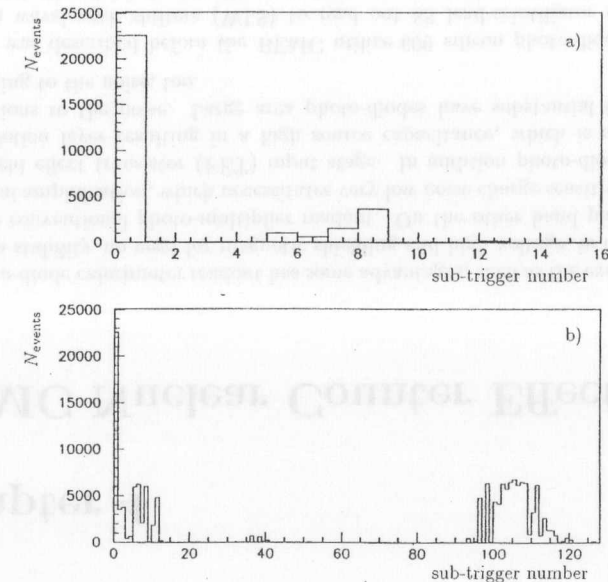
Fig. 4.1: Accepted (a) and raw (b) sub-trigger compositions.

The first information concerning the timing of the BEMC SDE at the level of HERA bunch crossings is as it is depicted in bunch number distributions, see Fig. 4.2.

During the 1993 luminosity period the standard bunch configuration used to be: 8 ×
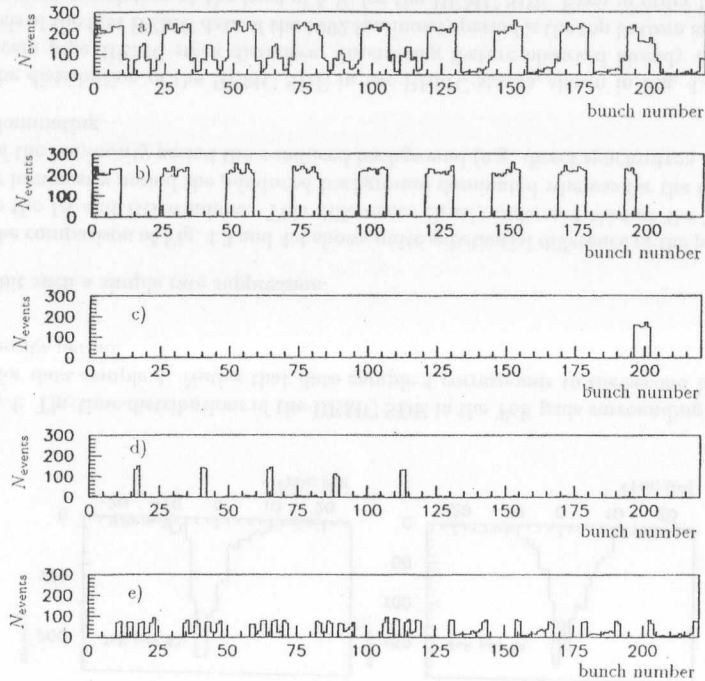
Fig. 4.2: Bunch number distribution of the BEMC single diode events for all (a), only colliding (b), p-pilot (c), e-pilot (d) and empty (e) bunches.

$10 + 4$ colliding, 5×2 e-pilot and 1×6 p-pilot bunches. These plots indicate the filled bunches (i.e. direct synchrotron radiation and the passage of the charged particles from the p-induced background) are the main sources of the BEMC SDE, but the non-negligible amount of the BSET triggers inside the empty bunches indicates also the presence of the very late particles with respect to beam particles.

The fraction of events triggered by BSET trigger elements inside the empty bunches suggests the trivial suppression of the BEMC SDE rates at the CTL to allow to the BSET trigger elements to trigger only during the filled bunches. On the other hand taking into account increase of the number of filled bunches for the 1994 luminosity period this option brought only marginal effect.

More detailed information on the timing of the BEMC SDE provides the discriminated NIM standard[2] output pulses of the individual ToF pads put into the FADC system of the drift chamber readout [50] available in the reconstruction program (TOFT bank).

---

[2]Nuclear Instrumentation Module, conforming to the mechanical and electrical standards outlined in AEC Report No. TID-20893 [41].

The zero of the timing distribution is adjusted to the genuine ep events in the backward region (DIS sample selection [87, 88]). The interaction window (IA) stretches from about -5 ns to +20 ns and the background window (BG) is roughly -30 ns to -5 ns. The timing precision is expected to be at the level of 1 or 2 ns [51]. The time distributions of the BEMC SDE in the ToF pads surrounding the beam pipe during the two run periods represented by data sample 2 and 4, (see Tab. 4.1) are shown in the Fig. 4.3 and 4.4, respectively.

Fig. 4.3: The time distributions of the BEMC SDE in the ToF pads surrounding the beam pipe for data sample 2. Note, that data sample 2 corresponds to the beginning of the luminosity period.

The striking difference of the time distributions for the ToF wall pads # 1 and # 0 is absence of the BG peak in the ToF wall # 0 (further from BEMC) which is of course the consequence of the ToF veto logics requiring the presence of the signals in the BG windows in both walls in order to veto the events. One more trivial additional suppression of the BEMC SDE could be achieved requiring the veto to be constructed only of the ToF wall pads closer to the BEMC (ToF 1), but the very non-trivial and potentially dangerous effect of the spurious early or late particles (see the distribution of the BEMC SDE inside the empty bunches Fig. 4.2) and partly also the cosmics overlayed with physics events
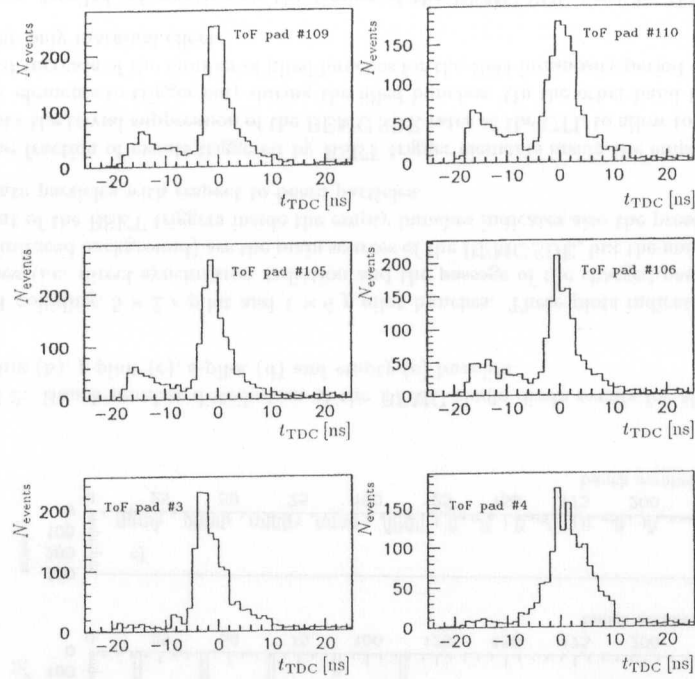
Fig. 4.4: The time distributions of the BEMC SDE in the ToF pads surrounding the beam pipe for data sample 4. Notice that data sample 4 corresponds to the second half of the luminosity period.

prohibit such a simple rate suppression.

The comparison of Fig. 4.3 and 4.4 shows quite substantial difference of the population inside the IA and BG windows. This differences clearly indicated that at the beginning of the luminosity period the p-induced background dominated whereas for the the second half of the luminosity period the e-induced background (e.g. direct synchrotron radiation) was dominating.

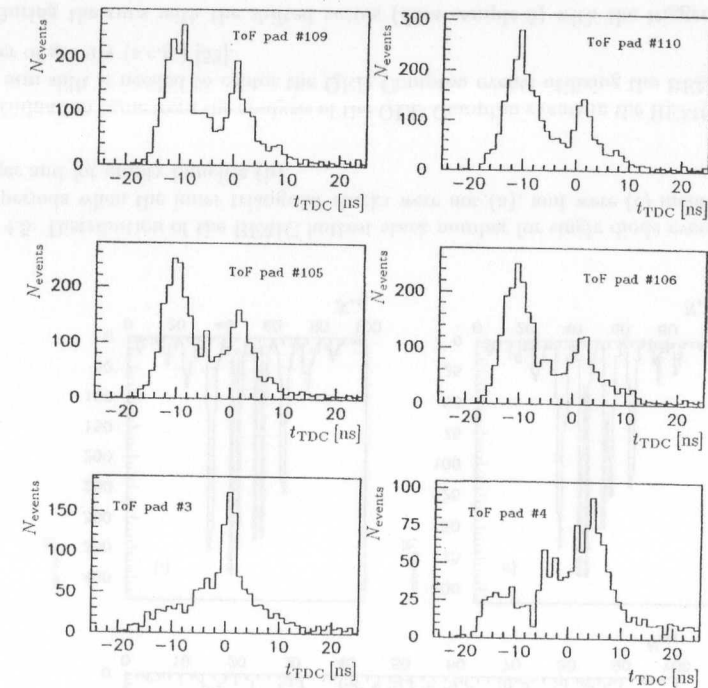The distribution of the BEMC SDE in the BEMC stacks, shown in Fig. 4.5.a, maps the beam pipe–BEMC-stack distances. Interesting feature observed already during the analysis of the first BEMC data of the 1992 luminosity period is the top bottom asymmetry of the event population at the level of 5 % for the BEMC SDE. Even in order to exclude the possible effect of slightly different BSET trigger thresholds for the different BEMC regions the off-line reconstructed stack energy was required to be greater then 8 GeV the asymmetry was still at the level of 3 %. An explanation of this effect was a few mm (4 mm) shift of the BEMC position vertically down (i.e. in -y direction). The precise
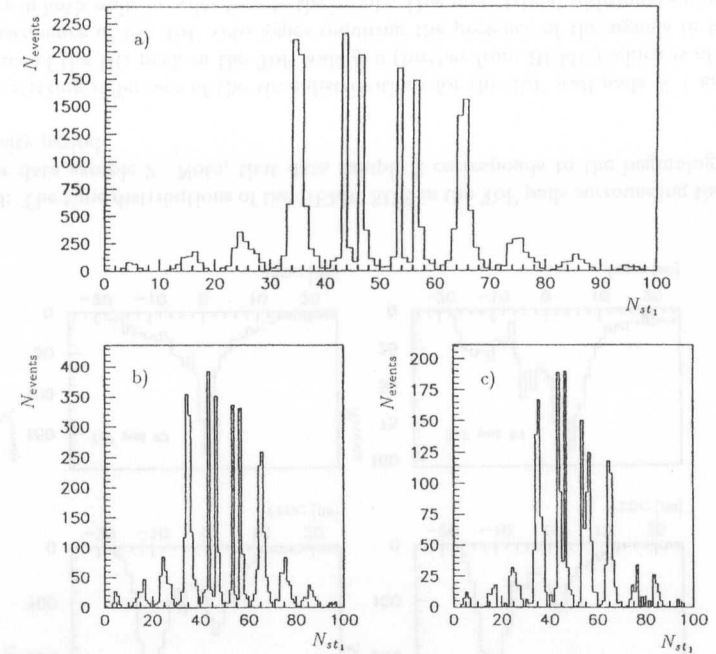
Fig. 4.5: Distribution of the BEMC hottest stack number for single diode events, for the run periods when the inner triangular stacks were not (a), and were (c) included in the trigger and for empty bunches (b).

determination came from the analysis of the QED Compton events in the BEMC. (4.6 +/-1.6) mm shift is needed to center the QED Compton events utilizing the BEMC shower center of gravity (s.c.g.) [53].

During the runs with the shifted vertex (data sample 5) with the trigger setup restricted to the BSET sub-triggers we opened the inner triangles of the trigger, i.e. the high stack thresholds [28] were lowered essentially from the infinity (DAC counts 255) to the same level as for all other stacks (5 DAC counts corresponding approximately to 2.3 GeV). In this way the cluster was allowed to be initiated also by the energy depositions in side stacks. Unexpected effect was only very low increase of the SDE in the inner triangles, which demonstrates Fig. 4.5.c.

The difference of the geometrical layout of the triangular and quadratic stacks results in the different optical properties. The light attenuation was for triangular stacks lower by factor of 2.5 [52] with respect to the neighboring quadratic ones. On the other side the signal amplitude due to SDE events is independent on the optical properties only by the physical properties of the photo-diodes (depletion layer). This results effectively in suppression of the SDE in triangular stacks by approximately the same factor 2.5.

The stack distribution of the BEMC SDE for the empty bunches, see Fig. 4.5.b again exhibits the beam pipe pattern as it is in the case of colliding bunches. The detailed timing distributions of the BEMC SDE inside the empty bunches for the beam pipe surrounding ToF pads are in the Fig. 4.6. The missing population of the BG window indicates the correlated activity inside both ToF walls.
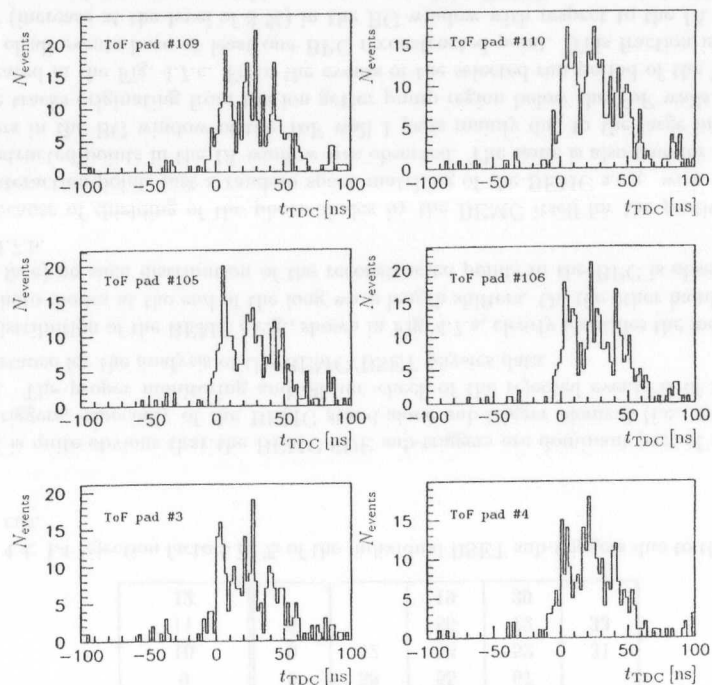
Fig. 4.6: The time distributions of the empty bunches in the ToF pads surrounding the beam pipe.

In order to quantitatively illustrate the effect of the BEMC SDE on the BSET sub-trigger rate typical runs from the data samples 1 to 5 (see Tab. 4.1) were arbitrarily selected.

The dead time corrected L1 rates of the individual BSET sub-triggers (st #0 → #12) are in Tab. 4.3. Note the changing meaning and pre-scale factors of some BSET sub-triggers especially at the beginning of the luminosity period.

The L1 rates presented in Tab. 4.3 are for the BSET sub-triggers suppressed at the L4 trigger level on the basis of the algorithm in the Appendix A. The rejections of the BEMC SDE triggers for the individual BSET sub-triggers in the selected runs are summarized in Tab. 4.4.

Run number	data sample	I_e [mA]	I_p [mA]	Luminosity $[mb^{-1}s^{-1}]$	Dead time [%]	Comments
57062	1	11.8	12.2	375	30.3	BPC partly off
62009	2	12.5	10.9	404	4.1	No magnetic field
64431	3	14.2	9.8	163	6.8	Collimator C3 opened
65458	4	14.2	9.8	544	12.7	–
66306	5	13.1	7.7	228	3.6	Vertex shifted open triangular stacks

Tab. 4.2: Selected runs from the indicated run periods, being defined in 4.1.

Sub-trigger number	Run number				
	57062	62009	64431	65458	66306
0	8.3	10.5	3.7	4.6	6.6
1	0.02		0.01	0.03	
2	0.02		0.008	0.01	
3	0.003		0.004	0.003	
4	0.005		0.004	0.004	
5	0.47	0.41	0.27	0.49	
6	0.27	0.002	0.11	0.16	
7	0.001	0.06	0.84	0.90	2.9
8		0.05	1.67	2.5	
9	0.03	0.002	0.005	0.008	
10	0.03	0.002	0.005	0.007	0.02
11		0.0	0.01	0.001	0.01
12		0.01	0.14	0.11	

Tab. 4.3: Dead time corrected L1 rates in Hz of the BSET sub-triggers.

Sub-trigger	Run number				
number	57062	62009	64431	65458	66306
0	65	88	78	83	59
1	13		67	79	
2	24		48	63	
3	0		7	17	
4	0		47	25	
5	43	83	83	86	
6	26	33	52	60	
7	19	60	29	41	17
8	28		48	55	
9	0	58	55	67	
10	0	52	53	52	31
11	0		86	72	33
12			19	39	

Tab. 4.4: L4 rejection factors in % of the individual BSET sub-triggers due to the BEMC SDE cut.

It is quite obvious that the BEMC SDE sub-triggers are dominant part of all BSET sub-triggers, especially of the BEMC stand-alone sub-trigger element (i.e. sub-trigger # 0). The proper monitoring and off-line check of the rejected events is of the great importance for the analysis of the BEMC/BSET physics data.

Distribution of the BEMC s.c.g., shown in Fig. 4.7.a, clearly identifies the locations of the photo-diodes at the end of the long wave length shifters. On the other hand (BEMC front face) no such distribution of the reconstructed points in the BPC is observed, see Fig. 4.7.b.

Because of shielding of the photo-diodes by the BEMC itself for the particles from the interaction point, just a random space matching of the BEMC s.c.g. with the BPC reconstructed points in the IA window was observed. The same is also true for the SDE triggers in the BG window of the ToF wall 1 pads mainly due to the large inclination of the tracks originating from the ion getter pump region below the ToF walls. This is illustrated in the Fig. 4.7.c. From the events of the selected run period of the Table 4.1 56 % of all events have at least one BPC reconstructed point. This fraction is slightly larger (increase at the level of 8 %) in the BG window with respect to the IA window. Even very moderate space matching requirement of the BEMC s.c.g. and the BPC point at the level of the stack dimensions (approx. 16 cm), will cut 55 % of the SDE triggers with the associated BPC point. The total suppression factor of the BEMC SDE triggers up to 4 can be expected using the BPC information.

The stack energy spectrum of the BEMC SDE in the Fig. 4.8.a demonstrates an equivalent energy scale of the SDE is in the range of the scattered electron energies and therefore its potentially danger.

The hottest stack energy spectrum of the leading cluster for the BEMC SDE triggers is equivalent to the one channel energy spectrum scaled down by the number of corresponding channels (WLS) in stack (in most cases 4) and smeared by the noise contributions
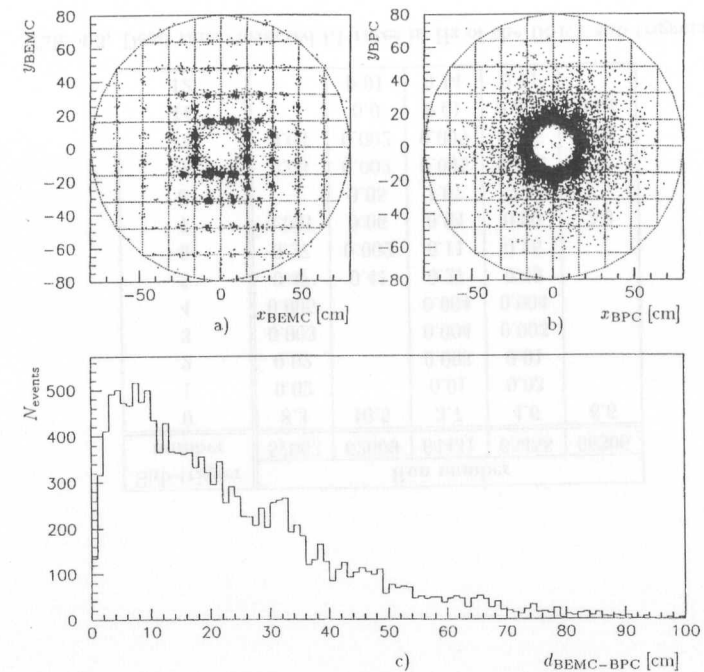
Fig. 4.7: BEMC s. c. g. distribution (a); BPC reconstructed point distribution (b); and the distribution of distance between the BEMC s. c. g. and the closest BPC reconstructed point (c) are shown.

of the other channels (WLS) of the same stack. This is demonstrated on the Fig. 4.8.c, where the single diode spectrum after the suppression of the pedestal is drawn. These energy spectra have two energy components (low and high). High energy component is predominantly due to the p-induced background as it is shown on the Fig. 4.8.b.

In order to understand the influence and the equivalent energy scale of the γ-radiation on the BEMC photo-diodes we used the Co^{60} radioactive source (two cascade γ-lines with energy 1.173 and 1.333 MeV) with activity of 1.8 MBq to irradiate the spare small trapezoid stack connected to the position of the BEMC stack # 96. Beside the missing high energy tail component the one channel spectrum of the radioactive source (Fig. 4.8.d) match quite reasonable the shape of the spectrum of the BEMC SDE triggers (Fig. 4.8.c) beside approximately four times increased energy scale of the SDE triggers.
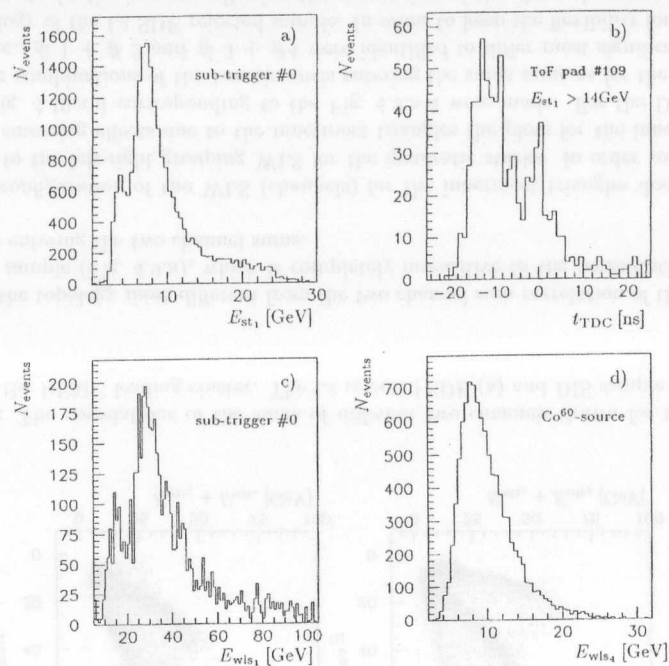
Fig. 4.8: The hottest stack energy spectrum of the BEMC SDE (a), TDC timing information for the hottest stack with energy above 14 GeV (b), the one channel SDE spectrum after the suppression of the pedestal (c), the one channel spectrum of the radioactive source (d).

4.2   L1 Trigger Suppression of BEMC Nuclear Counter Effect

Taking into account the beam dominated profile of the SDE triggers we installed the beam pipe lead shielding, covering the region between the BEMC and the shutters of the ToF 1 wall (8.5 cm).

On the top of the improved passive lead shielding, which suppressed fraction of the direct and scattered synchrotron radiation the active recognition of such type of SDE events at the L1 trigger level was designed and installed. For the design of the electronics the 3 constrains were taken into account:

Having in mind that the 1994 luminosity period was the last one for the BEMC/BSET system, the electronics was required to be ready within the limited time period of the 1993 winter shutdown. The following compromise between the highest possible suppression of the SDE triggers at the L1 trigger level and the available time constrain was found:

1. to equip only the two innermost BEMC "rings" (i.e. stacks 33 → 36, 43 → 46, 53 → 56, 63 → 66) containing the mostly affected stacks with active recognition of the SDE triggers;

2. to use only the intermediate granularity, i.e. the sum of the two channels (= WLS) instead of the full available granularity, (each single channel) for the recognition of the SDE.

Two inner BEMC "rings" represent 12 stacks[3], which are just 14 % of the total number of BEMC stacks. Based on the Fig. 4.5.a the suppression factor up to 3.6 can be reached, i.e. 72 % of the BEMC SDE are contained in these stacks. The relative suppression factor is slightly higher in the case of the open inner triangular stacks for the total triggering, see Fig. 4.5.c.

The characteristic feature of the BEMC SDE, is the high energy deposit just in one channel and essentially the noise in the others of the same stack. Therefore for identification of the SDE it was sufficient to use the intermediate granularity of stacks, i.e. to compare the two channel sums. This decreased the number of necessary trigger channels by factor 2.

This is illustrated on the series of the two channel sum correlation plots in Fig. 4.9.a-d for the hottest stack in the leading BEMC cluster. Fig. 4.9.a is based on the L4 rejected SDE sample (see Tab 4.1), whereas Fig. 4.9.b-d are for the part of the DIS sample [87, 88].

Fig. 4.9.a shows the presence of the non-SDE stacks in the L4 SDE reject sample based on the off-line SDE identification algorithm, which is searching for the hottest stack in the leading BEMC cluster. The presence of these non-SDE stacks slightly smears also the space distribution of the BEMC s.c.g. in the Fig. 4.7.a. In contrary, the L4 flagging algorithm (see Appendix B) is trying to identify the SDE trigger only on the basis of the BEMC leading stack. Comparing these discrepancies we concluded the necessity of the L4 BEMC SDE flagging routine update for the 1994 luminosity period in the following way:

All BEMC stacks should be checked to determine the SDE feature, but instead of the immediate setting of the rejection flag the energy of all SDE identified channels (WLS) were set to zero and the event was rejected only if the leading BEMC energy cluster (if any) after such "rescaling" procedure was below the activated trigger threshold (i.e. CL1, CL2 or CL3).

In the two channel sum correlations of the DIS sample, shown in Fig. 4.9.b-d, we can clearly identify the admixture of the SDE triggers, which were not rejected on the level L4 trigger due to the presence of other sub-trigger elements and passed to the DIS events sample selection satisfying all selection criteria, such as presence of vertex, corresponding BPC spatial hit to the BEMC cluster, etc.

Comparing the 3 possible combinations of the two channel sums for the DIS sample (Fig. 4.9.b-c) the correlation of the sums of the channels #1+#2 and #3+#4 forming the left-right (or top-bottom) trigger channel correlation for the quadratic stacks was found

---

[3]In case of inner triangular stack are included the two inner BEMC "rings" represents 16 stacks.
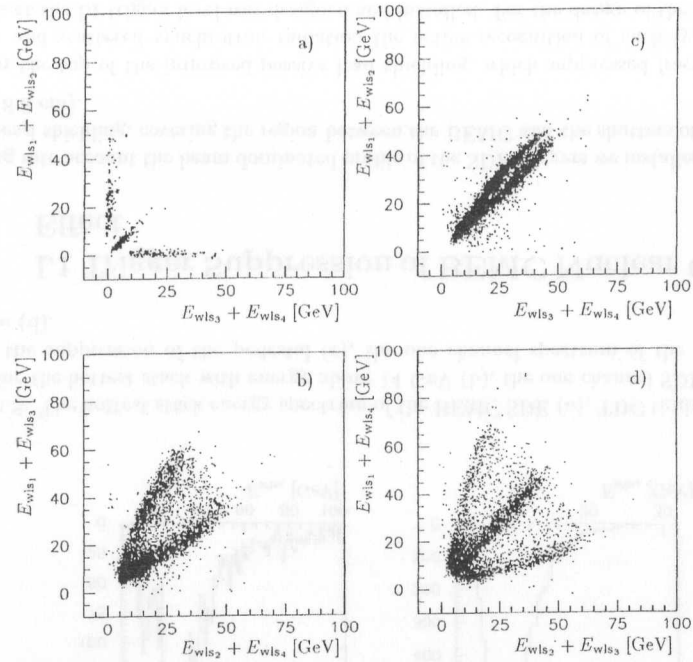
Fig. 4.9: The correlations of the sums of different two channels drawn for the hottest stack of the BEMC leading cluster. The L4 rejected SDE (a) and DIS sample (b-d) were used.

to have the topology most different from the two channel sum correlation of the L4 SDE rejected sample (Fig. 4.9.a), which is completely insensitive to the permutations of the channels entering the two channel sums.

The configuration of the WLS (channels) for the innermost triangles does not correspond to the left-right grouping WLS for the quadratic stacks. In order to check the possible smearing effects due to the innermost triangles the plots for the innermost triangles Fig. 4.10.a-d corresponding to the Fig. 4.9.a-d were made. For the DIS sample again the combinations of the two channels entering the sums same as for the quadratic stacks, i.e. # 1 + # 2 and # 3 + #4 were identified to differ most significantly from the topology of the L4 SDE rejected sample. In order to keep the flexibility for the inner triangular stacks the jumpers allowing the regrouping of the channels entering the two channels sums were installed.

The block scheme of the electronics and the SDE trigger suppression logics is in Fig. 4.11.
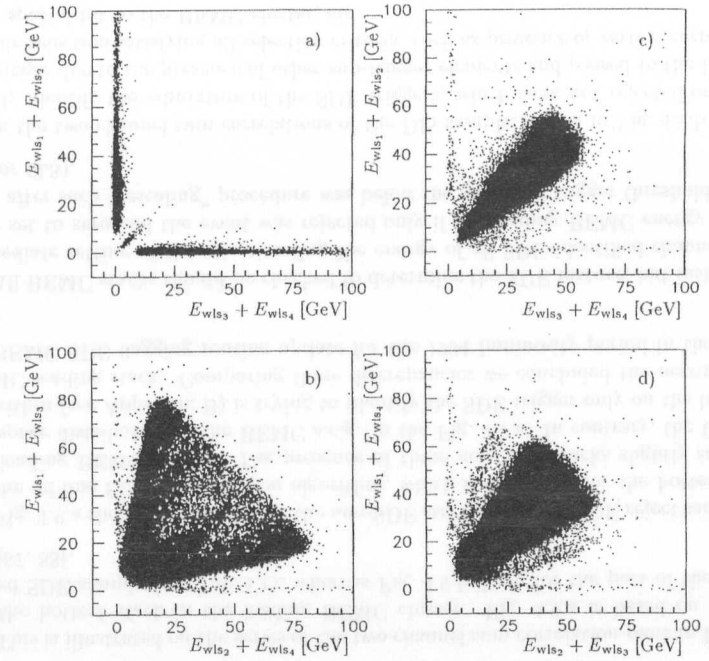
Fig. 4.10: The correlations of the sums of different two channels drawn for the hottest *triangular* stack of the BEMC leading cluster. The L4 rejected SDE (a) and DIS events sample (b-d), were used.

The analog sums (SUM) of the 2 photo-diodes are shaped (SHAPER) and put into the comparators (COMP.) with manually adjustable thresholds LT1 for the analog sum of the photo-diodes #1 and # 2 and LT2 for the analog sum of the photo-diodes #3 and #4. The purpose of the thresholds LT1 and LT2 is to suppress safely the noise in the two channel sums. The shaped signals of the two channel sums are split in order to create the additional sum of four channels which is subsequently compared to the high stack threshold HT and to the comparators with low two channel thresholds (LT1, LT2). The purpose of the HT is to provide the additional tool for the separation of the L4 rejected (Fig. 4.9.a) and the DIS sample (Fig. 4.9.b) topologies.

The resulting SDE veto signal for particular stack is set if the following condition is fulfilled:

$$HT = On \text{ and } (LT1 = Off \text{ or } LT2 = Off)$$

The t_0 was determined on the basis of the additional summing (SUM) and subsequent differentiation (DIFF.) of the splitœ two channel sum signals and is synchronized (SYNC.)
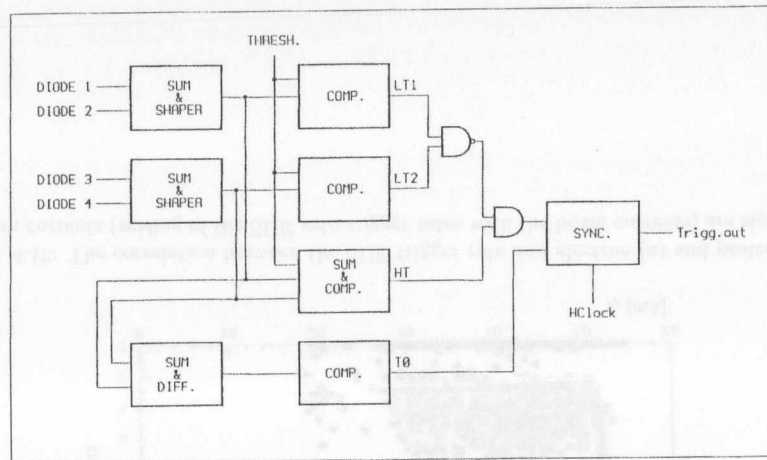
Fig. 4.11: Block scheme of the single diode event trigger electronics for single stack.

with the result of the digital pattern logics together with the HERA clock (HClock). The final SDE veto for event (Trigg.out) was built as the logical OR of all involved stack and put into the BEMC Timing Module [28], where the adjustable delay was installed to ensure the simultaneous output of the SDE veto trigger element with all other BSET bits to the CTL.

The fraction of events with more then one BSET high threshold in the nominal time slice for the sample of L4 rejected events (Table 4.1) is 4 %. The hardware design of the BSET did not provide the possibility to identify the leading cluster and due to the restriction of the active recognition to the two inner BEMC "rings" it was obvious to limit the application of the SDE veto only for the events with exactly one BSET high stack threshold (2.3 GeV). In order to provide this information to L1 level trigger counting of the number of high thresholds was introduced. The final veto applied for the particular BSET sub-triggers was then the coincidence of the two BSET trigger elements EQ1 (exactly one high threshold found) and SDE.

The adjustment strategy for the low thresholds LT1 and LT2 closely followed the regions depicted on Fig. 4.9.a trying to suppress the maximum of the L4 SDE rejected sample taking into account the necessity not to reject the DIS events of Fig. 4.9.b. The non-trivial threshold adjustment procedure was made in a few iterations. For the noise threshold LT1 and LT2 the scope was used to set the first approximation and afterwards the procedure was repeated using the calibration system. The final adjustment and the check was made on the basis of the off-line analysis of the cosmics and HERA background activity triggered by BSET, where the SDE veto trigger element was monitored.

The complete electronics was installed in the four independent boxes (for each CDU module containing four stacks one SDE module) and plugged in between the BEMC CDU output and BEMC analog box input. The fine adjustable delay (1 bunch crossing range) was used for the HERA clock in order to compensate the different paths of the BSET trigger signals and SDE veto.

4.3   Conclusion

The sensitivity of the BEMC photo-diode readout to the the passage of charged particles or photons through the photo-diode depletion layer causes another type of background, known as nuclear counter effect, or "single diode events" [24] which significantly increased the rate of the BEMC trigger. The three main sources of the these spurious triggers were identified as:

1. beam-gas and beam-wall interactions,

2. direct and scattered synchrotron radiation,

3. leaking shower particles originating from the the interaction point.

Since the p-induced background, beam-wall and beam-gas collisions were effectively vetoed by the ToF system, the following action were taken to suppress the increase of the trigger rates mainly due to synchrotron radiation:

1. The accelerator synchrotron radiation was reduced by lead shielding of the beam pipe in the BEMC region.

2. During the shutdown 1993/94 the sixteen inner most BEMC stacks were equipped by the L1 trigger veto logic. To identify an SDE the comparison of energy deposition in the individual photo-diodes after noise suppression with a sufficiently high energy threshold was used.

3. The L4 trigger level of the H1 trigger system was used for suppressing the triggers due to the nuclear counter effect especially in the stacks not equipped with veto logic.

The correlation between the SDE trigger rate and electron (a) and proton (b) beam currents (scaling of the SDE veto trigger rates with the beam currents) are shown in Fig. 4.12. Whilst there is no dependence of the trigger rate on the proton current there is a clear correlation between trigger rate and the electron beam current.
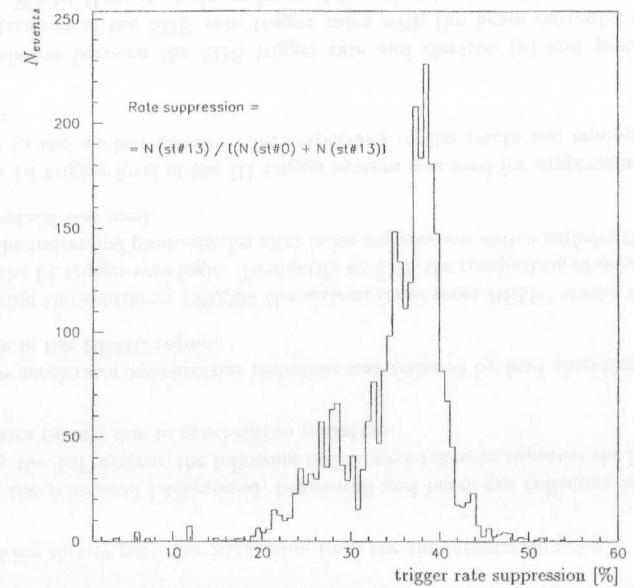
The effect of BEMC SDE L1 trigger is presented in the distribution of sub-trigger # 0 rate suppression. This figure proves the 40 % decrease of the trigger rate applying the SDE veto (sub-trigger # 13) to the BSET stand-alone CL2 trigger element (sub-trigger # 0), shown in Fig. 4.13.

Chapter 5
QED Compton Event Selection

This chapter contains the experimental techniques used to select the QED Compton event samples in both 1994 and 1995 data taking. In order to follow the various configurations of HERA machine and H1 experiment the different classification routines and selection procedures were employed. The corresponding sets of appropriate detector and kinematical cuts to isolate the clean QED Compton event samples were imposed. The trigger elements used in collecting the data samples were studied.

5.1 1994 Data Sample

The data used in the BEMC QED Compton event sample analysis were collected during the run period in 1994 ($77325 <$ run number < 90419), with electrons of energy $E_e = 27.52$ GeV colliding with protons of energy $E_p = 820$ GeV, resulting in a total center of mass energy of $\sqrt{s} \simeq 300$ GeV . HERA operated with e^-p collision in 1992, 1993 and the start of 1994, and e^+p collision for the major part of 1994 and for the whole 1995[1].

The majority of events was produced with the IP centered around zero in z, called the "nominal vertex" data sample. The IP was also shifted in the forward direction to an average position of $z = +67$ cm which permits measurement of the scattered electron up to $\theta_e \simeq 176.5°$. This sample is referred to as the "shifted vertex" data sample to distinguish it from the data with a nominal event vertex.

To reduce the systematic error of the here presented analysis a strict data selection was performed based on the behavior of the main detector components. From the detector status definition point of view only the data taken during the periods when the CJC1, FTD, LAr, BEMC, ToF, LS (see the corresponding Sec. 3.2.2, 3.2.1, 3.3.2, 3.3.4 and 3.2.5) components were according the SC system (see Sec. 3.2.6) information fully operational are considered.

During the low and stable accelerator background condition the four innermost triangular stacks of BEMC were included in the trigger. These data will be referred as the "open triangle" data sample in contrary with the data triggered without those four innermost BEMC elements further referred as "close triangle" data sample. Data samples definitions corresponding to the different HERA and H1 configuration are surveyed in Tab. 5.1.

---

[1] Further-on the incident and scattered lepton will be referred to as an "electron".

| Data | Run range | | HERA | z-vertex | BEMC |
sample	first	last	mode	position	triangular stacks
1.	77325	82005	e^-	nominal	closed
2.	82961	87556	e^+	nominal	closed
3.	87586	89412	e^+	nominal	closed
4.a	89413	89912	e^+	nominal	open
4.b	90101	90419	e^+	nominal	open
5.	89929	90025	e^+	shifted	open

Tab. 5.1: 1994 data samples definitions corresponding to different HERA and H1 configurations.

5.2 BEMC QED Compton Event Sample

The analysis presented here is based upon a sample of QED Compton events, which are characterized by an electron and a photon coplanarly scattered. As it was described in Sec. 2 the cross section of the quasi-real QED Compton events is a strongly rising function of the polar angles of the scattered particles. Therefore the majority of the whole sample have both outgoing particles scattered to the backward part of the H1 detector, which was covered by the BEMC [34]. In order to minimalize the systematics for the luminosity measurement and improve understanding of the BEMC only the sample of QED Compton events with both scattered particles measured in the BEMC, so called BEMC QED Compton events were used.

The BEMC QED Compton candidate was identified by searching for two most energetic electromagnetic clusters with the back-to-back topology in the BEMC. The electromagnetic clusters penetrate less deeply into the calorimeter and tend to exhibit less lateral dispersion than the hadronic clusters. Thus, using a cut on the cluster radius, calculated as the energy weighted radial distance of the calorimetric cells from the cluster center-of-gravity, allows to distinguish between these two. The calorimetric signal could be associated at most by three reconstructed central tracks pointing to the BEMC clusters and/or a few spatial points in the BPC grouped within a small distance in $r - \phi$ plane from the clusters center-of-gravity and without any other detected activity. The number of reconstructed tracks and spatial points depends on the acceptances and efficiencies of the central tracker and BPC and the probability of the γ-conversion into e^+e^--pair whereas penetrating the dead material in front of the active areas of the tracking devices.

The possible background processes are DIS[2], photo-production interactions, vector meson production and the collisions of the beam particles with either the beam-pipe material, so-called "beam-wall" interactions, or the residual gas particle, "beam-gas" and synchrotron radiation.

5.2.1 BEMC QED Compton Event Trigger

The selection of BEMC QED Compton events was based on the low-Q^2 neutral current DIS event sub-trigger [36], which was composed of the BSET CL2 cluster trig-

---

[2]Only DIS events with the specified event topology were considered, see Sec. 6.3.2.2.

ger element (BSET_CL2) in coincidence with BSET single diode events veto trigger element (BSET_SDV) and ToF veto, so-called s0 sub-trigger[3]:

$$\text{s0:} \quad \text{BSET\_CL2 \&\& BSET\_SDV \&\& !ToF\_BG \&\& (FToF\_IA || !FToF\_BG)} \quad (5.1)$$

The trigger element combination BSET_CL2 && BSET_SDV triggered the most energetic electromagnetic cluster in BEMC, simultaneously vetoing the SDE and thus lowering the rate of the whole sub-trigger. The combination of veto trigger elements !ToF_BG && (FToF_IA || !FToF_BG) rejected the majority of the beam-gas and beam-wall interactions using the time information provided by ToF and FToF systems.

5.2.1.1   Trigger Efficiencies

In order to evaluate the trigger efficiency and to study the influence of excluding the BEMC four innermost triangular stacks from the BSET trigger on its efficiency the events triggered by other trigger elements than BSET (e.g. z-vertex trigger, ToF) were selected. At least one reconstructed BPC spatial hit was required to ensure some energy deposit in BEMC. The two data samples for both the "open triangle" data sample ($89444 \leq$ run number ≤ 89928) and "closed triangle" data sample ($89082 \leq$ run number ≤ 89412) were studied.

Here one should keep in mind that the BSET trigger was not a truly inclusive electron trigger since in the case when more trigger clusters were found, the resulting trigger cluster energy was the total energy sum of all such clusters [36]. Hence, the trigger efficiency had to be estimated from the two dimensional distribution for the leading cluster and the total cluster energy. For cluster energies above 10 GeV the one dimensional dependence on the leading cluster energy turned out to be a good approximation [36].

The BSET_CL2 trigger efficiency as a function of the BEMC leading cluster is shown in Fig. 5.1.a. The cluster energy dependence shows a characteristic feature of a good trigger, i.e. the narrow transition region, steep efficiency rise, and full efficiency on the plateau above the threshold. The fit by modified 3-parameter Fermi-Dirac distribution function[4] yields the threshold value of 6.9 ± 1.6 GeV, and shows that the BSET_CL2 is 100% efficient above the 10 GeV. Requiring the BEMC leading cluster energy higher than 10 GeV the efficiency distribution in the BPC plane for the innermost region was drawn, see Fig. 5.1.b. It proves the full efficiency in the BEMC triangular stacks region. The same distribution drawn for the closed triangular data, see Fig. 5.2.a, indicates inefficiencies caused due to exclusion of the triangular stacks from the trigger. To get rid of them the energy restriction ($E_{\text{cl}_1} > 10$ GeV) was accompanied with a following fiducial cut: The hottest stack of the leading BEMC cluster was not allowed to be one of the triangular

---

[3]For the logical operations among different trigger elements the C language operators are used.

[4]Modified 3-parameter Fermi-Dirac distribution function [36]:

$$\epsilon(E_i) = \frac{p_3}{1 + \exp\frac{p_1 - E_i}{p_2}},$$

where p_1 is the threshold value, defined as the energy at which trigger efficiency reaches 50%, p_2, is the width of the transition region, so-called threshold width, at $\pm 3p_2$ the efficiency reaches 95% and 5%, respectively, and p_3 is the maximal reached efficiency.
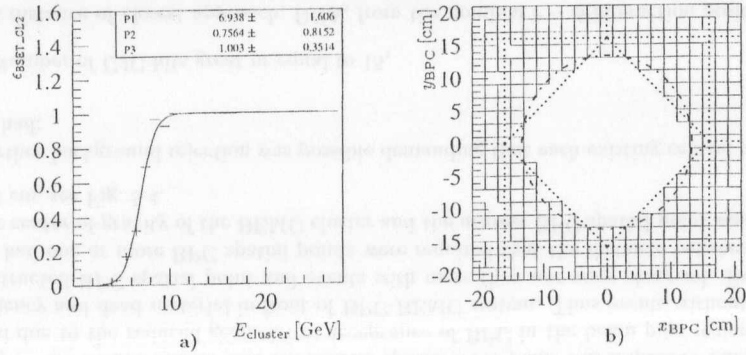
Fig. 5.1: The BSET cluster trigger CL2 efficiencies for leading cluster energies (a) fitted with Fermi-Dirac function and requiring the BEMC leading cluster energy higher than 10 GeV in the BPC plane for the innermost region for run period with "open" triangular stacks (b). The inner sensitive radius of BPC is sketched by dashed and dotted line, whilst the dotted lines show the innermost BEMC stack structure.

stacks, i.e. the stack with the stack number 44, 45, 54, 55 in the BEMC numbering scheme, see Sec. 3.3.2. Imposing this cut on the "closed triangular" data samples, the efficiency distribution shown in Fig. 5.2.b was improved.

The BSET trigger (i.e.BSET_CL2 && BSET_SDV) efficiency for the leading cluster in BEMC ($E_{cl_1} > 10$ GeV) was $99.8 \pm 0.6\%$ and $100 \pm 0.4\%$, for "open" and "closed triangle" data sample, respectively.

The BToF and FToF trigger efficiencies were evaluated using the data triggered by monitor triggers, i.e. sub-triggers with one or more conditions missing (here the BToF and FToF trigger elements) with the pre-set down-scaling, used for measurement of efficiencies and monitoring of the sub-trigger elements that they made redundant. The sample of events with an electron candidate (leading cluster energy in BEMC more than 11 GeV, cluster radius less than 5 cm, z coordinate of the reconstructed vertex from the interval 36 cm $\leq z \leq$ 96 cm, the distance between the shower center-of-gravity of the BEMC cluster and the nearest spatial BPC point less than 5 cm) in BEMC was selected and the BToF and FToF trigger elements were tested. The study showed that the BToF and FToF had the efficiency of $99.6 \pm 0.7\%$ and $99.5 \pm 0.6\%$ respectively, which gave in total the final efficiency of $99.1 \pm 1.1\%$.

On the L4 of H1 trigger system further non-ep beam-wall and beam-pipe background, as well as single diode events suppression was performed.

5.2.2　L5 Classification and POT/MPOT Selection

We used the sample of QED Compton event candidates identified by the event L5 classification algorithm. The QED Compton event sample (QEDCOM) together with the initial
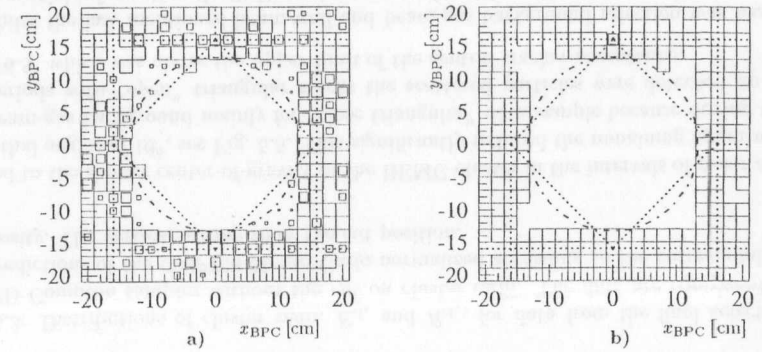
Fig. 5.2: The BSET cluster trigger CL2 efficiencies for leading cluster energies requiring the BEMC leading cluster energy higher than 10 GeV in the BPC plane for the innermost region for run periods with the "closed" triangular stacks. Inefficiencies caused due to exclusion of the triangular stacks from the trigger (a). The effect of imposing a fiducial cut which required that the hottest stack of the leading BEMC cluster was not one of the triangular stacks (b). The inner sensitive radius of BPC is sketched by dashed and dotted line, whilst the dotted lines show the innermost BEMC stack structure.

and final state radiative event samples were grouped in the class of radiative physics candidates (F-pack class 12).

The BEMC QED Compton selection part of the L5 classification routine EQEDC demanded:

1. The existence of at least two BEMC clusters,

2. first three most energetic BEMC clusters energies:

   (a) $E_{cl_1} \geq 8$ GeV

   (b) $E_{cl_2} \geq 4$ GeV

   (c) $E_{cl3} \leq 2$ GeV

3. the total visible energy $E_{vis} = E_{cl_1} + E_{cl_2}$: 18 GeV $\leq E_{vis} \leq$ 32 GeV,

4. the acoplanarity of the first two most energetic BEMC cluster: $180° - |\phi_{cl_1} - \phi_{cl_2}| < 45°$,

5. the number of all reconstructed CJC tracks which have:

   (a) Number of CJC hits great or equal to 10,

   (b) a distance of closest approach, DCA, from the nominal $r - \phi$ interaction position, i.e. the absolute value of vertex corrected DCA less then 2 cm,

(c) a distance in z from the nominal interaction point of the point where the DCA is defined, $|z_{DCA} - z_0| < 50$ cm,

(d) radius at which track starts less than 30 cm.

less or equal 3,

6. the absolute value of z coordinate of the vertex: $|z| < 100$ cm.

During the classification and selection step of the analysis the dead material in front of the BEMC and BEMC crack correction values were not used (i.e. the BCLR bank instead of BCFR bank information was explored) to allow the re-processing starting from physics output tapes (POT) level after further refinements of the reconstruction and correction routines. In order to allow faster access for analysis and more flexible data handling in the re-processing procedure a sample containing only the events classified only as QED Compton events candidates was stored on cartridges, called mini-pots (MPOT's).

5.2.3 Background Rejection

In order to reject as far as remaining background and consequently get a clean sample of BEMC QED Compton events additional selection criteria had to be imposed.

Better identification of final electron and photon in BEMC was based on the fact that the electromagnetic clusters tend to exhibit less lateral dispersion than the hadronic clusters. Events were required to have lateral spread of cluster, which was energy weighted cluster radius, less than 5 cm, see Fig. 5.3.

Despite of knowing that the final state of QED Compton events consist of one charged and one neutral particle the restriction on the distance between the shower center-of-gravity of the BEMC cluster and the nearest spatial BPC point was imposed. This was limited due to the reduced geometrical acceptance of BPC in the beam pipe region, its inefficiency and dead material in front of BPC-BEMC system. Thus events without any reconstructed BPC spatial point and events with more than one were observed. Events which had one or more BPC spatial points were required that the distance between the shower center-of-gravity of the BEMC cluster and the nearest BPC spatial point was less than 8 cm, see Fig. 5.4.

Further background rejection was possible demanding that each existing central track which had:

1. Number of CJC hits great or equal to 15,

2. a distance of closest approach, DCA, from the nominal $r - \phi$ interaction position, i.e. the absolute value of vertex corrected DCA less then 2 cm,

3. a distance in z from the nominal interaction point of the point where the DCA is defined, $|z_{DCA} - z_0| < 100$ cm,

4. radius at which track starts less than 30 cm,
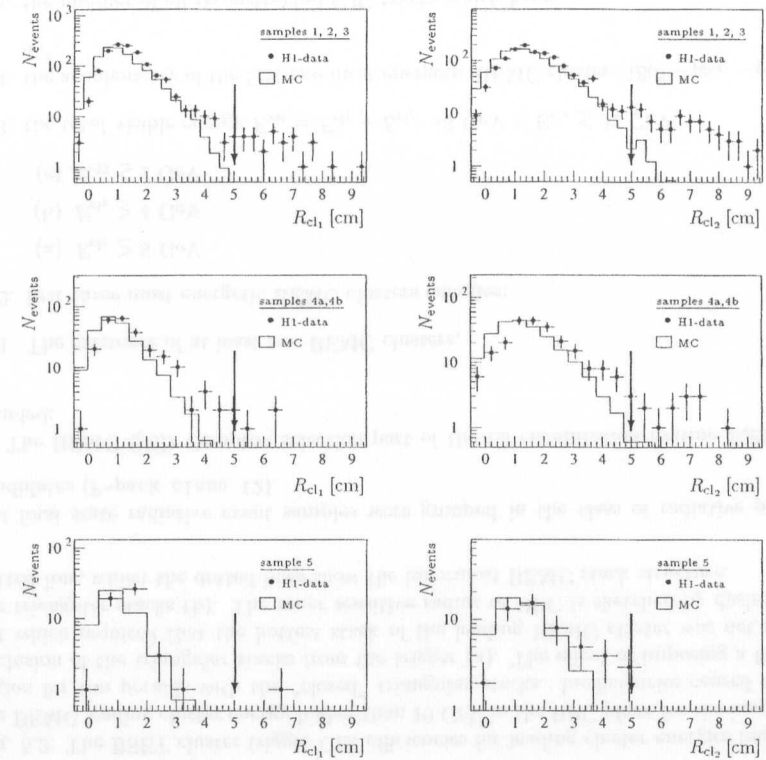
Fig. 5.3: Distributions of cluster radii, R_{cl_1} and R_{cl_2}, for data from the final selection of QED Compton samples without the cut on cluster radii. The data are compared to the predictions of the COMPTON Monte Carlo normalized according to the corresponding luminosity. The vertical arrows show the cut position.

pointed to the shower center-of-gravity of the BEMC cluster in the intervals of polar and azimuthal angles of 10°, see Fig. 5.5. This significantly reduced the remaining beam-wall and beam-gas background mainly for "close triangular" data sample because during the run periods with "open" triangular stacks the scattered particles were detected up to $\theta \simeq 176.5°$ which was above the upper limit of the central tracker acceptance.

Whilst the last mentioned beam-wall and beam-gas background rejection was based on the spatial information the ToF requirement profitted from the ToF time information. Because of the limited geometrical acceptance the right ToF ep-collision timing ($t_{ToF} > -5$ ns) for both first and second most energetic cluster was required only for events from "closed triangle" data samples.

Allowing electronic noise of the level of three times the average noise of the BEMC
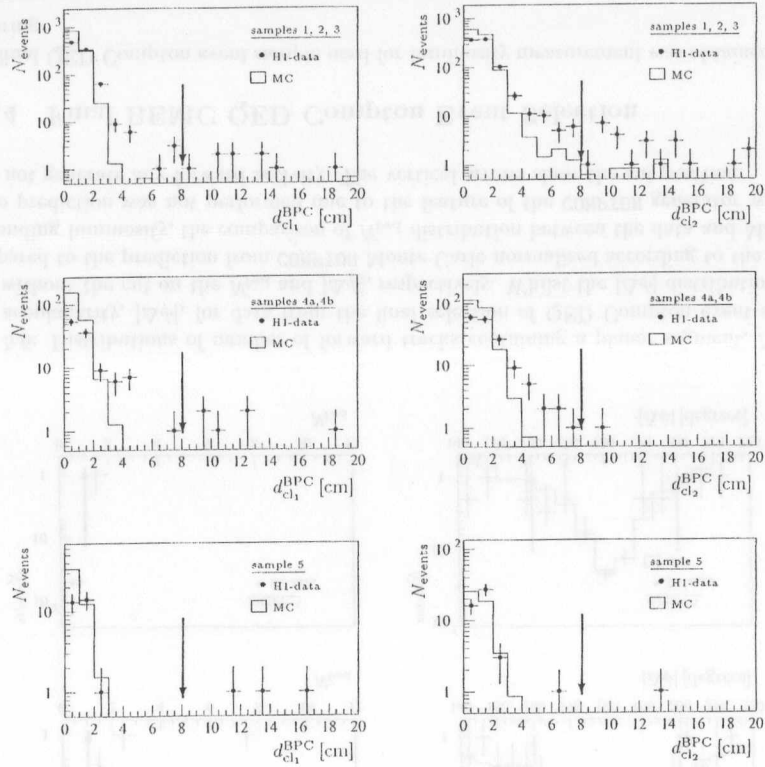
Fig. 5.4: Distributions of distances between the shower center-of-gravity of the BEMC cluster and the nearest spatial BPC point, $d_{cl_1}^{BPC}$ and $d_{cl_2}^{BPC}$, for data from the final selection of QED Compton samples without the cut on these distances. The data are compared to the predictions of the COMPTON Monte Carlo normalized according to the corresponding luminosity. The vertical arrows show the cut position.

cluster the total energy in the BEMC was limited to be contained in the two cluster identified as the QED Compton candidate.

Further off-line rejection of single diode events, was based on the BEMC redundancy as it was described in Sec. 4.2.

All kind of background processes which showed any activity in the forward scattering region of H1 detector was suppressed demanding:

1. no forward track containing a planar segment,
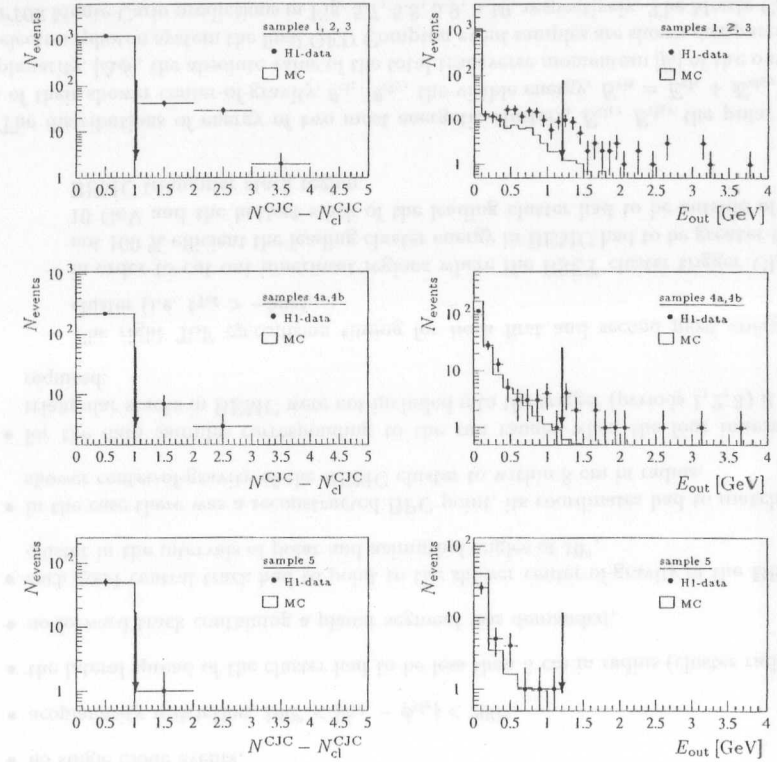
Fig. 5.5: Distributions of $N^{CJC} - N_{cl}^{CJC}$, where N^{CJC} is the number of good central tracks (for definition of a good central track see the text) and N_{cl}^{CJC} is the number of good central tracks pointing to the shower center-of-gravity of the BEMC cluster in the intervals of polar and azimuthal angles of 10°, for data from the final selection of QED Compton event samples without the cut on the number of good central tracks. Distribution of energy in BEMC outside of the first two clusters $E_{out} = \sum_i E_{cl_i} - (E_{cl_1} + E_{cl_2})$, for data from the final selection of QED Compton event sample without the cut on E_{out}. The data are compared to the predictions of the COMPTON Monte Carlo normalized according to the corresponding luminosity. The vertical arrows show the cut position.

2. the total LAr energy in forward region defined by the conus covering 45° area from the nominal interaction point had to be less than certain limit. The higher value of 2 GeV was chosen in order not to be affected by electronic noise.

Finally, the selection was finished imposing the tighten acoplanarity restriction, $180° - |\phi_{cl_1} - \phi_{cl_2}| < 20°$, see Fig. 5.6.
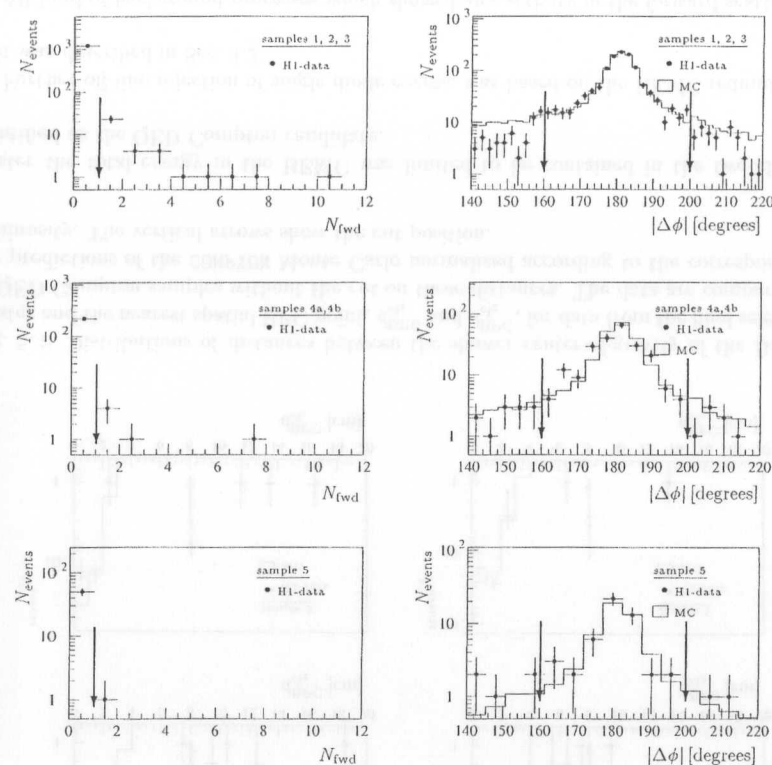
Fig. 5.6: Distributions of number of forward tracks containing a planar segment, N_{fwd}, and acoplanarity, $|\Delta\phi|$, for data from the final selection of QED Compton event samples without the cut on the N_{fwd} and $|\Delta\phi|$, respectively. Whilst the $|\Delta\phi|$ distribution, is compared to the prediction from COMPTON Monte Carlo normalized according to the corresponding luminosity, the comparison of N_{fwd} distribution between the data and Monte Carlo prediction was not performed due to the feature of the COMPTON generator which does not generate any forward activity. The vertical arrows show the cut position.

5.2.4   Final BEMC QED Compton Event Selection

The final QED Compton event sample used for luminosity measurement was obtained by requiring:

- Only good and medium runs (according the H1 ep-classification),

- well defined H1 detector status (requiring the HV bit of all relevant components to be on),

- the sub-trigger s0 requirement,

- the energy requirements on the first three most energetic clusters in BEMC (BCLR bank) were $E_{\text{cl}_1} \geq 8$ GeV, $E_{\text{cl}_2} \geq 4$ GeV, $E_{\text{cl}3} \leq 2$ GeV, respectively, and the cut on the sum of the energy of the first two BEMC clusters was 20 GeV $\leq E_{\text{cl}_1} + E_{\text{cl}_2} \leq$ 32 GeV,

- the right ToF ep-collision timing for both first and second most energetic cluster (i.e. $t_{\text{Tof}} > -5$ns),

- the total LAr energy in forward region defined by the conus covering 45° area from the nominal interaction point had to be less than 2 GeV,

- the sum of all BEMC cluster energies minus energy of both leading and second most energetic cluster had to be less than 1.20 GeV, which is approximately three times the average noise,

- no single diode events,

- acoplanarity restriction, $160° < |\phi_{\text{cl}_1} - \phi_{\text{cl}_2}| < 200°$,

- the lateral spread of the cluster had to be less than 5 cm in radius (cluster radius),

- no forward track containing a planar segment was demanded,

- each good central track had to point to the shower center-of-gravity of the BEMC cluster in the intervals of polar and azimuthal angles of 10°,

- in the case there was a reconstructed BPC point, its coordinates had to match the shower center-of-gravity of the BEMC cluster to within 8 cm in radius,

- for the data samples corresponding to the run ranges when the four innermost triangular stacks in BEMC were not included into the trigger (periods 1, 2, 3) it was required:

    – The right ToF ep-collision timing for both first and second most energetic cluster (i.e. $t_{\text{Tof}} > -5$ns),

    – in order to cut out innermost regions where the BSET cluster trigger CL2 is not 100 % efficient the leading cluster energy in BEMC had to be greater than 10 GeV and the hottest stack of the leading cluster had to be outside of the BEMC triangular stack region.

The distributions of energy of two most energetic clusters, E_{cl_1}, E_{cl_2}, the polar angles of their shower center-of-gravity, θ_{cl_1}, θ_{cl_2}, the visible energy, $E_{\text{vis}} = E_{\text{cl}_1} + E_{\text{cl}_2}$, the acoplanarity, $|\Delta\phi|$, the absolute value of the total transverse momentum $|\vec{p}_t|$ of the outgoing electron-photon system the final QED Compton event samples are shown compared to COMPTON Monte Carlo predictions in Fig. 5.7, 5.8, 5.9, 5.10, respectively. The Monte Carlo simulations describe data very well for the "closed triangle" data samples which are the most significant. The distributions for "open triangle" data samples (i.e. samples 4, 5) suffer due to the more complex / difficult optics in the triangular stacks compared to the rectangular ones. Different mirror effects resulted not only in a higher absolute signal of

factor 2.5 compared to the rectangular stacks, which was corrected in the reconstruction, but in addition in difficulties in the determination of the shower center-of-gravity. Therefore the most influenced is the distribution of the polar angle θ_{cl_1} (and consequentially $|\vec{p}_t|$ of the outgoing electron-photon system). Since the second most energetic cluster was not concentrated in the innermost BEMC region (where the triangular stacks were located) the distribution of the polar angle θ_{cl_2} is better described by the Monte Carlo simulation compared to the θ_{cl_1} distribution.
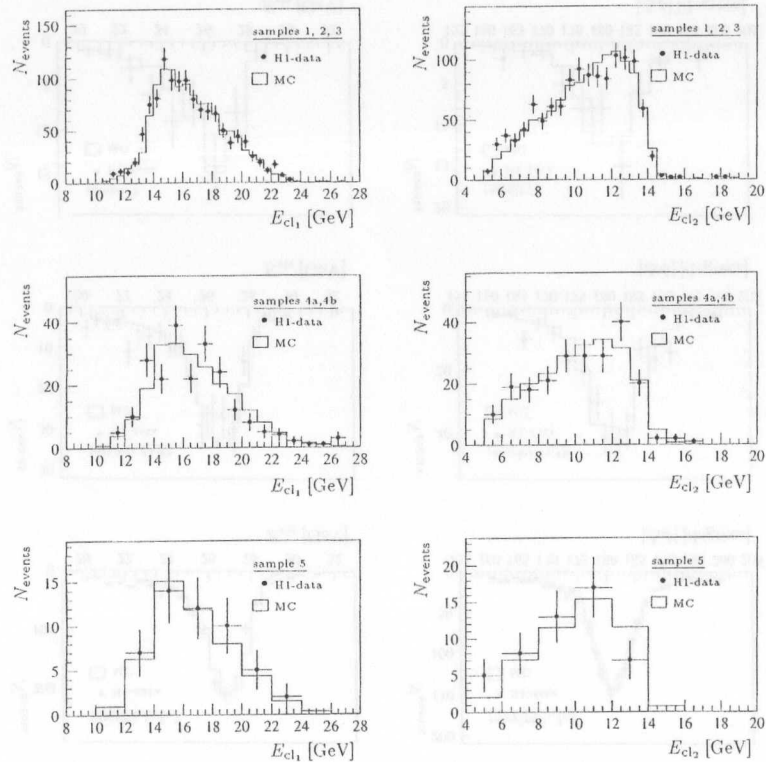
Fig. 5.7: Distributions of the cluster energies, E_{cl_1} and E_{cl_2}, for data from the final QED Compton samples. The data are compared to the predictions of the COMPTON Monte Carlo normalized according to the corresponding luminosity.

Fig. 5.8: Distributions of the polar angles, θ_{cl_1} and θ_{cl_2}, for data from the final QED Compton samples. The data are compared to the predictions of the COMPTON Monte Carlo normalized according to the corresponding luminosity.

5.3   1995 Data Sample

The analysis of the SPACAL QED Compton event sample is based on the data collected in 1995, with electron of energy $E_e = 27.54$ GeV colliding with protons of energy $E_p =$
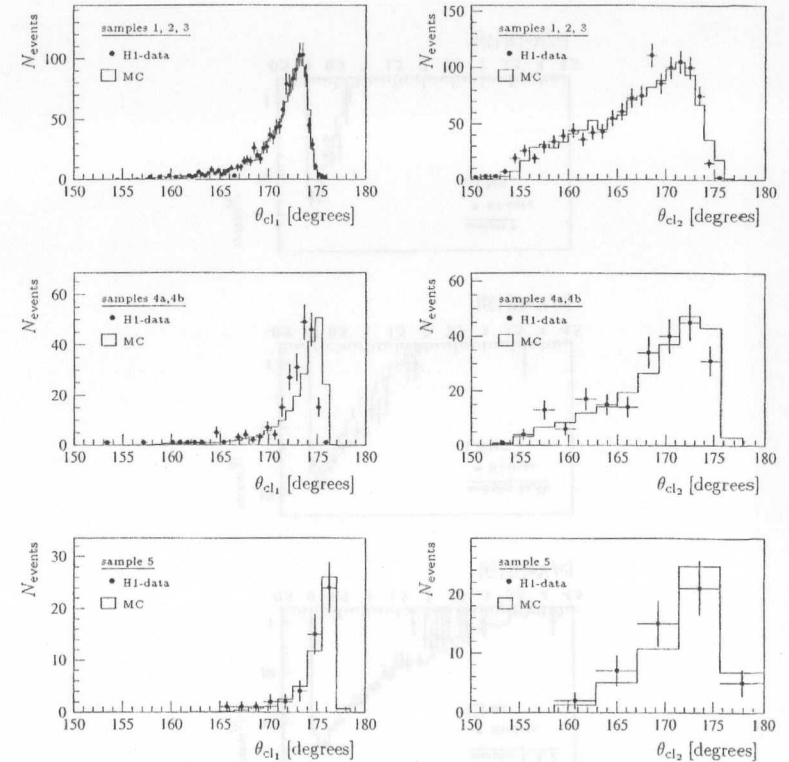
Fig. 5.9: Distributions of visible energy, E_{vis}, and acoplanarity, $|\Delta\phi|$, for data from the final QED Compton samples. The data are compared to the predictions of the COMPTON Monte Carlo normalized according to the corresponding luminosity.

Fig. 5.10: Distributions of the absolute value of the total transverse momentum, $|\vec{p}_t|$, of the outgoing electron-photon system for data from the final QED Compton samples. The data are compared to the predictions of the COMPTON Monte Carlo normalized according to the corresponding luminosity.
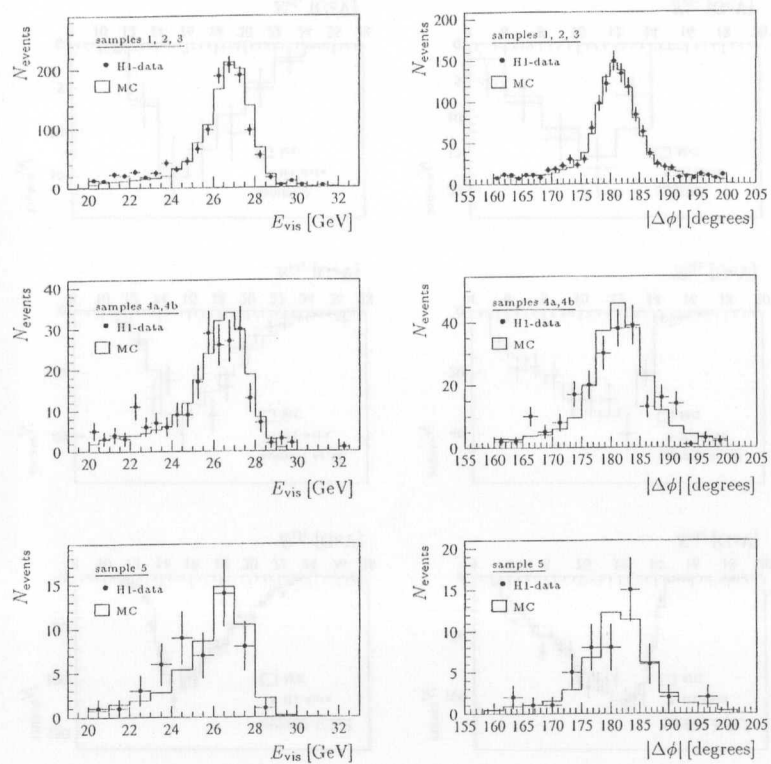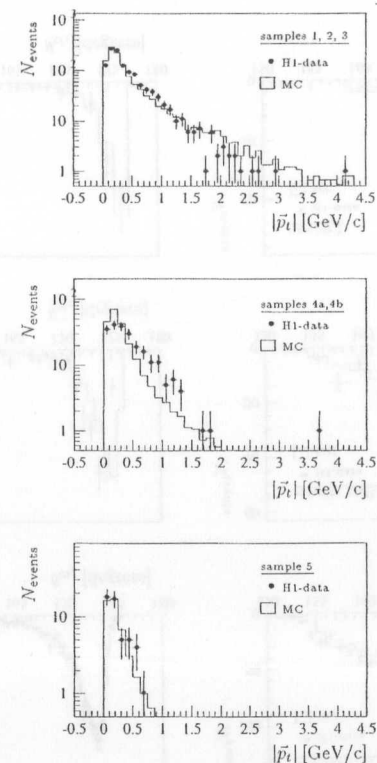
820 GeV.

As in previous years of data taking the interaction vertex was not always centered in its nominal position. The IP was shifted in the forward direction to an average position of $z = +70$ cm which together with the higher geometrical acceptance of a new electromagnetic calorimeter permits measurement of the scattered electron up to $\theta_e \simeq 178.6°$.

To insure a well-defined status of the detector components only the data taken during the periods when the CJC1, FTD, LAr, SPACAL, LS (see Sec. 3.2.2, 3.2.1, 3.4.2 and 3.2.5) components were according the SC system (see Sec. 3.2.6) information fully operational are considered.

The Tab. 5.2 presents the data samples definitions corresponding to different HERA and H1 configurations.

Data	Run range		z-vertex
sample	first	last	position
1.a	125960	129464	nominal
1.b	129934	131045	nominal
2.a	129473	129800	shifted
2.b	129801	129933	shifted

Tab. 5.2: 1995 Data samples definitions corresponding to different HERA and H1 configuration.

5.4　SPACAL QED Compton Event Sample

From the same reasons as in the 1994 data the ongoing analysis was based upon a sample of QED Compton events with both scattered particles measured in the electromagnetic part of SPACAL, so called SPACAL QED Compton events.

From the point of view of event topology, identification and possible background processes the SPACAL QED Compton events were the same nature as BEMC QED Compton events, see Sec. 5.2. On the other hand the experimental techniques used in measuring the SPACAL QED Compton events could profit from features provided by the new components in the upgraded H1 detector, in terms of better energy and space resolution, enlarged geometrical acceptance closer to the beam-pipe, reconstructed BDC track information (not only a single BPC spatial point) fully covering the electromagnetic part of SPACAL.

Despite the larger geometrical acceptance of the SPACAL compared to the BEMC and the higher instantaneous luminosity in 1995 with respect to the one reached during the 1994 data taking a significantly higher amount of detected QED Compton events was not stored mainly due to following reasons:

- The broadly upgraded H1 detector required a considerable amount of time invested in understanding of newly installed detectors and systems. Therefore the reasonable data were accumulated only during the short time period, i.e. autumn 1995 (125960 $\leq$ run number $\leq$ 131045).

- The 1995 on-line selection of the SPACAL QED Compton events was based on the low-Q^2 NC DIS sub-trigger, see Sec. 5.4.1, which was down-scaled by a large pre-scale factors, especially during the difficult background conditions. In order not to bias the on-going analysis the events with large weight (≥ 3) were excluded. This affected at most the majority of the data sample 1b, which will not be considered in the further analysis, where the absolute number of events is relevant.

5.4.1　SPACAL QED Compton Event Trigger

The on-line selection of 1995 SPACAL QED Compton events was based on the low-Q^2 neutral current DIS event sub-trigger, which was composed of the SPACAL IET trigger element SPCLe_IET>1 in coincidence with ToF veto trigger elements.

The trigger element SPCLe_IET>1 triggered the most energetic electromagnetic cluster in electromagnetic part of SPACAL detector, whilst the combination of the veto trigger elements (FToF_IA || !FToF_BG) && PLUG_VETO in coincidence with !BToF_BG && !VETO_inner_BG && !VETO_Outer_BG by means of time information from FToF, Plug ToF, BToF and VETO systems rejected any non-ep background.

In the 1995 shifted vertex running period there was a misprint in the L4 trigger steering file which affected the sub-trigger s0 treatment for runs 129801-130385. As a consequence a low-$|\vec{p}_t|$ track ($|\vec{p}_t| < 250$ MeV) was required for sub-trigger s0 and a single event was rejected if no other sub-trigger survived the L4 farm trigger algorithm [47]. The possibility to use events triggered by a sub-trigger not suffering from this misprint error was investigated. As a suitable candidate the sub-trigger s3, which was based on the trigger element SPCLe_IET>2, was chosen. Its trigger efficiency curve, see Fig. 5.11, unfortunately did not show a desired characteristic features such as the narrow transition region, steep efficiency rise, and full efficiency on the plateau above the threshold of $\simeq 9 - 10$ GeV. Therefore the sub-trigger s3 was not considered in further analysis.
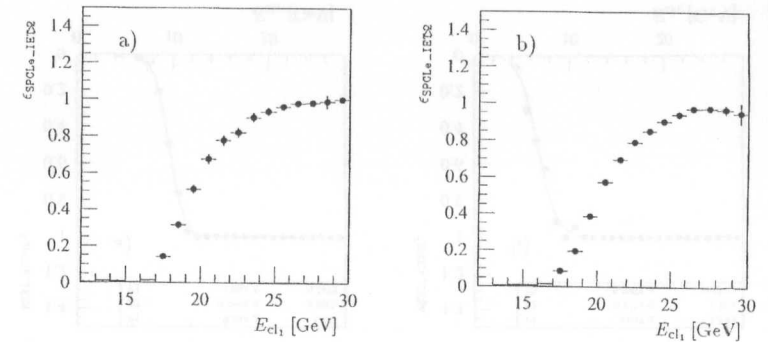
Fig. 5.11: The SPCLe_IET>2 cluster trigger efficiencies for leading cluster energies (a) for "nominal vertex" and (b) for "shifted vertex" data sample.

5.4.1.1   SPACAL IET Trigger Element Efficiencies

In order to evaluate the SPACAL trigger element SPCLe_IET>1 efficiency the events triggered by its monitor sub-trigger were selected.

Since the trigger rate had to be lower to the reasonable level already on the L1 trigger the different threshold values in the inner and outer region in SPACAL were used. The inner, covered by the central card, SPACAL region was defined by the square $x, y \in \langle -16, 8 \rangle \times \langle -16, 8 \rangle \mathrm{cm}^2$, see Fig. 5.12.
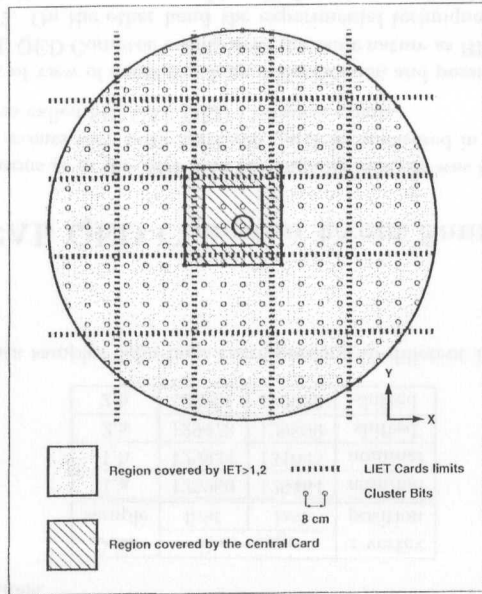
Fig. 5.12: The transversal view of the electromagnetic section of SPACAL with cluster bits positions and LIET regions. The borders of inner and outer regions are shown.

The SPCLe_IET>1 trigger efficiency as a function of the SPACAL leading cluster energy is shown for both inner and outer SPACAL region for "nominal vertex" data sample in Fig. 5.13.a,b and for "shifted vertex" data sample in Fig. 5.13.c,d.

The fit by modified 3-parameter Fermi-Dirac distribution function, see Sec. 5.2.1.1, yields for "nominal vertex" ("shifted vertex") data the threshold values of 9.6 ± 1.6 GeV (9.4 ± 2.2 GeV) for inner region and 6.7 ± 1.8 GeV (5.3 ± 3.8 GeV) for outer region. Comparing the trigger efficiency curves one can see that the SPCLe_IET>1 trigger starts to be fully efficient above the value of cluster energy of 12 GeV for inner and outer region. The IET trigger efficiencies for the SPACAL leading cluster energy ($E_{\mathrm{cl}_1} > 12$ GeV) in the inner and outer region calculated for the "nominal" and "shifted" vertex data are summarized in Tab. 5.3.
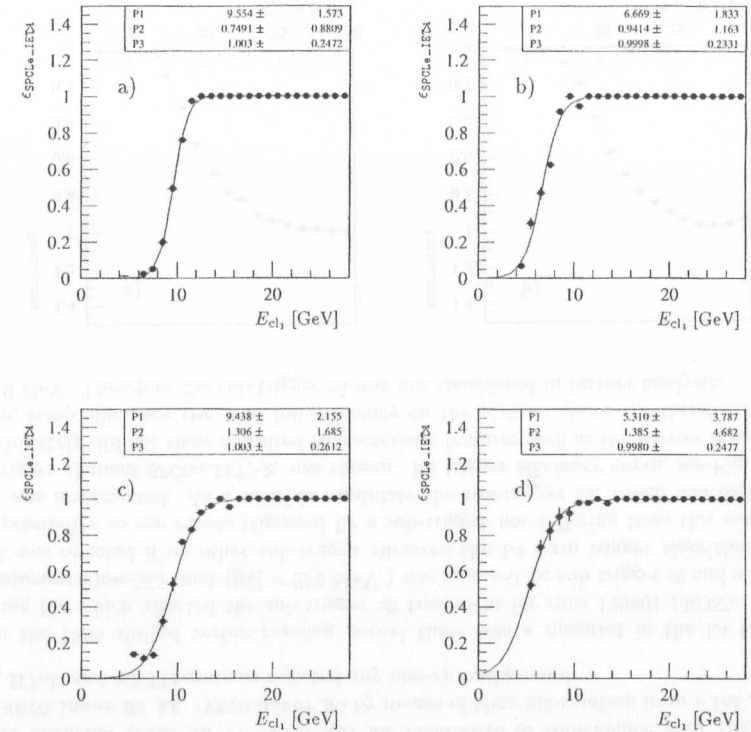
Fig. 5.13: The SPCLe_IET>1 cluster trigger efficiencies as a functions of the SPACAL leading cluster energies fitted with Fermi-Dirac function for (a, c) inner and (b, d) outer region of SPACAL and for (a, b) "nominal vertex" and for (c, d) "shifted vertex" data sample.

data	SPCLe_IET>1 efficiencies [%]	
sample	inner SPACAL region	outer SPACAL region
1.	100 ± 0.3	100 ± 0.4
2.	99.6 ± 0.6	99.8 ± 0.7

Tab. 5.3: The IET trigger efficiencies for the leading cluster energies $E_{\mathrm{cl}} > 12$ GeV in inner and outer SPACAL region.

Since the SPACAL trigger element was combined with the different scintillating veto and timing trigger elements their corresponding inefficiencies were calculated in order to obtain the efficiency of the sub-trigger s0. The BToF, FToF, PToF and Veto wall trigger element inefficiencies were evaluated using the data triggered by corresponding monitor triggers. The obtained inefficiencies are summarized in Tab. 5.4.

data	run range		trigger elements inefficiencies [%]		
sample	first	last	FToF	BToF, PToF	Veto wall
1.a	125960	129464	0.4 ± 0.1	1.4 ± 0.3	< 0.1
1.b	129934	131045	0.3 ± 0.1	1.2 ± 0.5	< 0.1
2.	129473	129933	0.3 ± 0.1	0.9 ± 0.4	< 0.1

Tab. 5.4: Scintillating veto trigger elements inefficiencies.

5.4.2   L5 Classification and DST Selection

In the 1995 data taking the events were selected for data summary tapes (DST) according to the L5 event classification algorithm. By means of it the QED Compton event sample (QEDCOM) together with the initial and final state radiative event samples was grouped in the class of radiative physics candidates (F-pack class 12).

The 1995 SPACAL QED Compton events were classified using two event classification routines, i.e. EQEDC and SQCFLA. The single event was accept as a candidate if it was classified by at least one of the two flagging routines.

The SPACAL QED Compton selection part of the EQEDC routine demanded:

1. The existence of at least two electromagnetic SPACAL clusters,

2. first two most energetic SPACAL clusters energies:

    (a) $E_{cl_1} \geq 8$ GeV,

    (b) $E_{cl_2} \geq 4$ GeV,

3. the total visible energy $E_{vis} = E_{cl_1} + E_{cl_2}$: 18 GeV $\leq E_{vis} \leq$ 32 GeV,

4. the acoplanarity of the first two most energetic SPACAL cluster: $180° - |\phi_{cl_1} - \phi_{cl_2}| < 45°$,

5. the number of all reconstructed CJC tracks which have:

    (a) Number of CJC hits great or equal to 10,

    (b) a distance of closest approach, DCA, from the nominal $r - \phi$ interaction position, i.e. the absolute value of vertex corrected DCA less then 2 cm,

    (c) a distance in z from the nominal interaction point of the point where the DCA is defined, $|z_{DCA} - z_0| < 50$ cm,

    (d) radius at which track starts less than 30 cm.

    less or equal 3,

6. the value of z coordinate of the vertex: -100 cm $< z <$ 150 cm.

7. a logical summation of the result of energy calibration and luminosity measurement oriented selection branches [43]:

(a) the energy calibration oriented part, which rejected all events which had more than two clusters with the energy of 2 GeV,

(b) the luminosity measurement oriented part, in which the events which might have been rejected due to presence of a third cluster (or more clusters) produced by clusterizing electronic noise were treated in the following way: Four electromagnetic clusters having more than 2 GeV in the SPACAL were accepted, and tested whether all two-by-two combinations of them pass the described above cuts on the energies and the acoplanarity, certainly without requiring the limit on the energy of the third cluster. In order to suppress any background processes with hadronic activity the lateral spread of cluster, cluster radius, was demanded to be less than 6 cm. The huge background contribution of DIS events was suppressed imposing a cut on an QED Compton event estimator[5]: $\chi^2 < 25$.

Since at the beginning of the commissioning of the new detectors the energy scale of the SPACAL detector was understood with a lower precision another classification routine SQCFLA with less demanding limits on the cluster energies was used. The SPACAL QED Compton event flagging routine SQCFLA demanded:

1. The existence of at least two electromagnetic SPACAL clusters,

2. first two most energetic SPACAL clusters energies:

    (a) $E_{cl_1} \geq 5$ GeV

    (b) $E_{cl_2} \geq 1$ GeV

3. the total visible energy $E_{vis} = E_{cl_1} + E_{cl_2}$: 12 GeV $\leq E_{vis} \leq$ 52 GeV,

4. the acoplanarity of the first two most energetic SPACAL cluster: $180° - |\phi_{cl_1} - \phi_{cl_2}| < 45°$.

5.4.3   Background Rejection

In order to reject as far as remaining background the similar procedure as for BEMC QED Compton events selection was used.

Since the L5 classification was based upon the logical sum of two routines, which one had too descriptive energy cuts the energy requirements on the first two most energetic

---

[5]The QED Compton estimator was based upon the energy-angular constraints [34]:

$$\chi^2 = \left(\frac{E_{cl_1}^{SCLR} - E_{cl_1}(\theta_1, \theta_2)}{0.3\sqrt{E_{cl_1}(\theta_1, \theta_2)}} \right)^2 - \left(\frac{E_{cl_2}^{SCLR} - E_{cl_2}(\theta_1, \theta_2)}{0.3\sqrt{E_{cl_2}(\theta_1, \theta_2)}} \right)^2$$

where:

$$E_{cl_1(cl_2)}(\theta_1, \theta_2) = \frac{2E_e \sin\theta_{2(1)}}{\sin\theta_1 + \sin\theta_2 + \sin(\theta_1 + \theta_2)}$$

is the energy of the first (second) cluster calculated using the polar angles of the two clusters, see Sec. 2.3.

cluster in electromagnetic SPACAL were tighten to be $E_{cl_1} > 8$ GeV, $E_{cl_2} > 4$ GeV, respectively, and the cut on the sum of the energy of the first two electromagnetic SPACAL clusters was required to be 22 GeV $< E_{cl_1} + E_{cl_2} < 32$ GeV.

Better identification of final electron and photon, in SPACAL was based on the fact that the electromagnetic clusters tend to exhibit less lateral dispersion than the hadronic clusters. Events were required to have lateral spread of cluster, i.e. cluster radius, less than 3.2 cm, see Fig. 5.14.
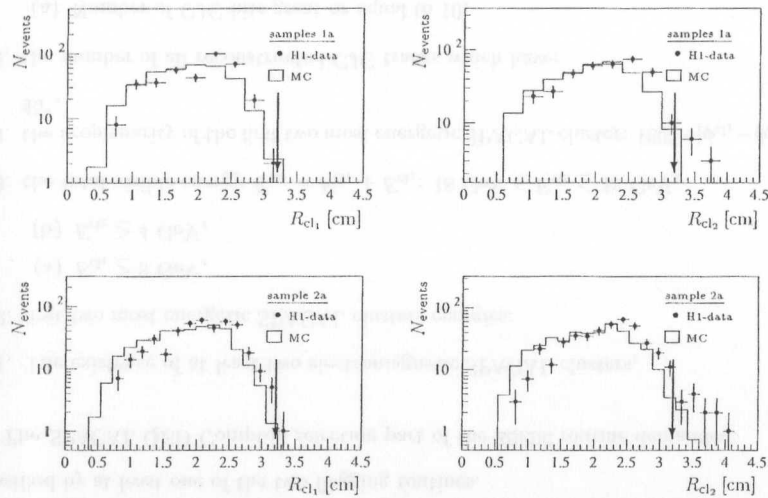
Fig. 5.14: Distributions of cluster radii, R_{cl_1} and R_{cl_2}, for data from the final selection of QED Compton event samples without the cut on the cluster radii. The data are compared to the predictions of the COMPTON Monte Carlo normalized according to the corresponding luminosity. The vertical arrows show the cut position.

The total energy in the SPACAL was limited to be contained in the two most energetic clusters identified as the QED Compton event candidate respecting the following: (i) Energy deposit in each of the veto layers was treated in the reconstruction procedure as a separate cluster; (ii) energy deposit in each of the veto layers could be affected by the energy leakage from the neighboring cells; (iii) since no fiducial cut on the shower center-of-gravity of the SPACAL cluster was applied, energy deposit in each of the veto layers could be either due to the events undershooting the SPACAL or upstream proton introduced background. Fig. 5.15 shows the correlation between the energy in SPACAL outside of first two clusters, $E_{out} = \sum_i E_{cl_i} - (E_{cl_1} + E_{cl_2})$, and the energy deposited in four veto layers $E_{veto} = \sum_{i=1}^{4} E_{veto}^i$. The horizontal arrows show the position of the cut on E_{out} which had to be less then 0.5 GeV.

All kind of background processes which showed any activity in the forward scattering region of H1 detector was suppressed demanding no forward track containing a planar segment, see Fig. 5.16.
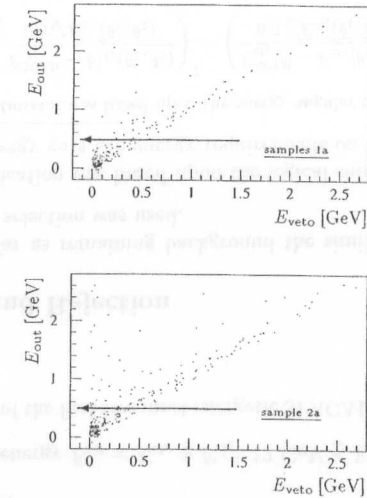
Fig. 5.15: Correlation between the energy in SPACAL outside of first two clusters, E_{out}, and the energy deposited in veto layers, E_{veto}, for data from the final selection of QED Compton event sample without the cut on E_{out} and E_{veto}. The horizontal arrows show the cut position.

Finally, the selection was finished imposing the tighten acoplanarity restriction, $180° - |\phi_{cl_1} - \phi_{cl_2}| < 15°$, see Fig. 5.16.

5.4.4   Final SPACAL QED Compton Event Selection

The final QED Compton event sample used for luminosity measurement was obtained by requiring:

- Only good and medium runs (according the H1 *ep*-classification),

- well defined H1 detector status (requiring the HV bit of all relevant components to be on),

- sub-trigger s0 requirement,

- the energy requirements on the first two most energetic cluster in SPACAL (SCLR bank) were $E_{cl_1} > 8$ GeV, $E_{cl_2} > 4$ GeV, respectively, and the sum of them had to be 22 GeV $< E_{cl_1} + E_{cl_2} < 32$ GeV,

- acoplanarity restriction, $165° < |\phi_{cl_1} - \phi_{cl_2}| < 195°$,
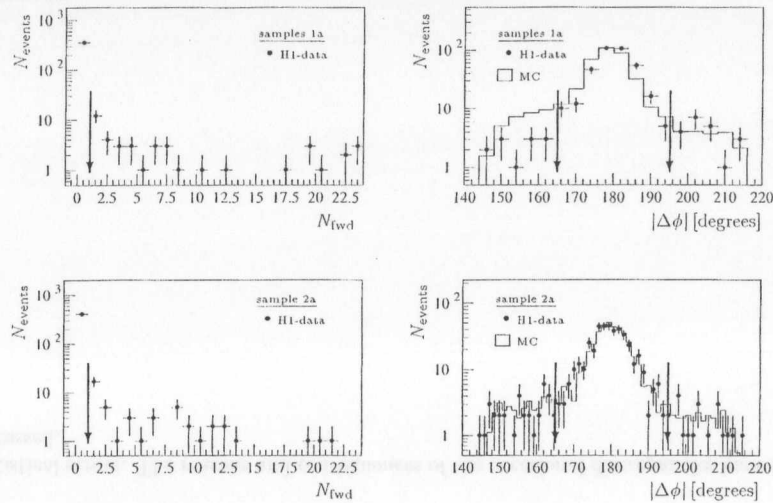
Fig. 5.16: Distributions of number of forward tracks containing a planar segment N_{fwd} and $|\Delta\phi|$ for data from the final selection of QED Compton event samples without the cut on the N_{fwd} and $|\Delta\phi|$, respectively. Whilst the $|\Delta\phi|$ distribution, is compared to the prediction from COMPTON Monte Carlo normalized according to the corresponding luminosity, the comparison of N_{fwd} distribution between the data and Monte Carlo prediction was not performed due to the feature of the COMPTON generator which does not generate any forward activity. The vertical arrows show the cut position.

- sum of all cluster energies in electromagnetic SPACAL minus energy of the first two most energetic ones had to be less then 0.5 GeV,

- the lateral spread of the cluster had to be less than 3.2 cm in radius (cluster radius),

- no forward track containing a planar segment was demanded.

The distributions of energy of two most energetic clusters, E_{cl_1} and E_{cl_2}, the polar angles of their shower center-of-gravity, θ_{cl_1} and θ_{cl_2}, the visible energy, $E_{\text{vis}} = E_{\text{cl}_1} + E_{\text{cl}_2}$, the acoplanarity, $|\Delta\phi|$, the absolute value of the total transverse momentum $|\vec{p}_t|$ of the outgoing electron-photon system the final SPACAL QED Compton event samples are shown compared to COMPTON Monte Carlo predictions in Fig. 5.17, 5.18, 5.19, 5.20, respectively.

5.5 Summary

The experimental techniques used to select the BEMC and SPACAL QED Compton event samples in both 1994 and 1995 data taking were described. Compared to [34] a new
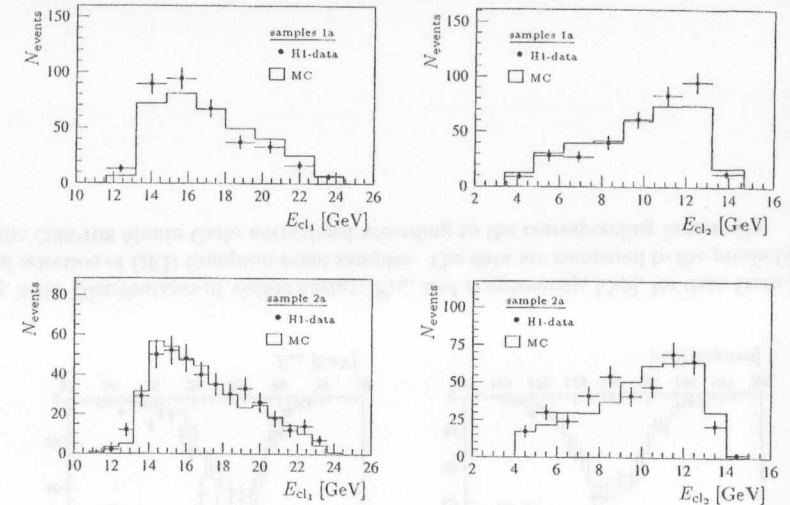
Fig. 5.17: Distributions of first two most energetic cluster energies, E_{cl_1} and E_{cl_2}, for data from the final selection of QED Compton event samples. The data are compared to the predictions of the COMPTON Monte Carlo normalized according to the corresponding luminosity.

selection procedure was designed in order to higher the efficiency of detecting BEMC and SPACAL QED Compton events. In both 1994 and 1995 several samples of QED Compton events have been analyzed following the various configurations of HERA machine and H1 experiment.

The identification of a QED Compton candidate, which is based upon searching for two most energetic electromagnetic clusters with the back-to-back topology in the BEMC in 1994 and SPACAL in 1995 has been described. The QED Compton events were triggered by an energy cluster with energy well above the trigger threshold in the BEMC in 1994 (SPACAL in 1995) which was not vetoed by the timing requirements. The trigger efficiencies for BEMC (SPACAL) and various combination of ToF trigger elements which has been determined from the data, have been presented.

The L5 classification routine EQEDC in 1994 and the 1995 classification based on two different algorithms, i.e. EQEDC and SQCFLA routines, have been discussed. In order to reject the remaining background and consequently to obtain the clean samples of BEMC and SPACAL QED Compton events in 1994 and 1995 respectively, additional selection criteria were to be imposed. The positions of the analysis cuts in the corresponding distributions have been presented.

Finally, the various distributions of basic kinematical variables for data are compared to the predictions of the COMPTON Monte Carlo. From the here presented plots it has been concluded that the Monte Carlo distributions are in a good agreement with data within
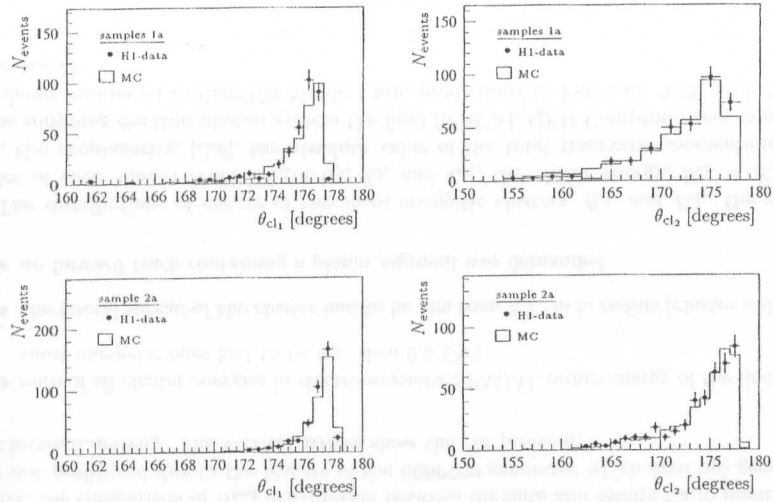
Fig. 5.18: Distributions of the polar angles of the first two most energetic clusters, θ_{cl_1} and θ_{cl_2}, for data from the final selection of QED Compton event samples. The data are compared to the predictions of the COMPTON Monte Carlo normalized according to the corresponding luminosity.

statistical errors. The reasons and consequences of the occasional discrepancies have been discussed.
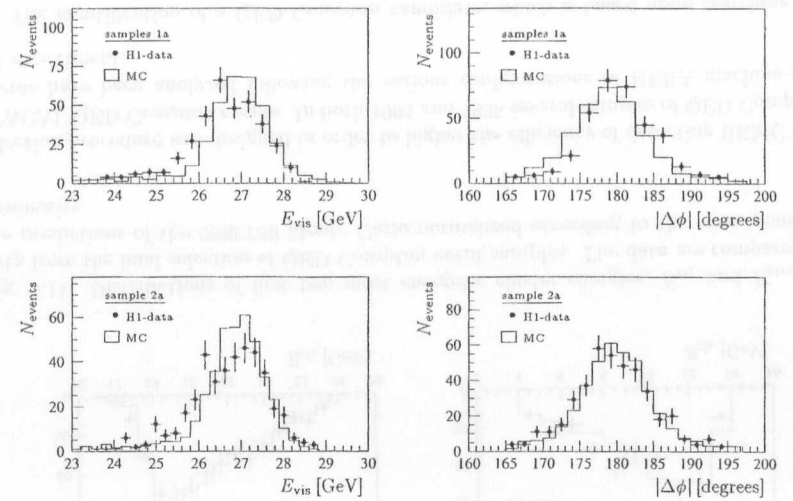
Fig. 5.19: Distributions of visible energy, E_{vis}, and acoplanarity, $|\Delta\phi|$, for data from the final selection of QED Compton event samples. The data are compared to the predictions of the COMPTON Monte Carlo normalized according to the corresponding luminosity.
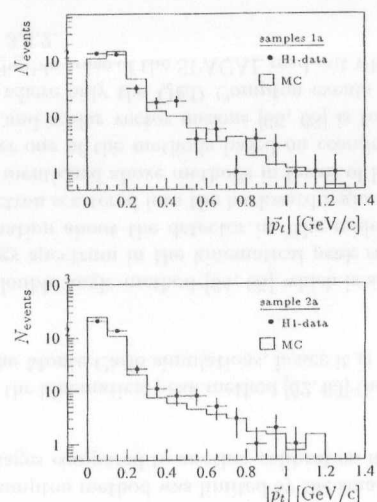
Fig. 5.20: Distributions of the absolute value of the total transverse momentum, $|\vec{p}_t|$, for data from the final selection of QED Compton event samples. The data are compared to the predictions of the COMPTON Monte Carlo normalized according to the corresponding luminosity.

Chapter 6

Experimental Results

This chapter is concerned with the analyses of the QED Compton event data samples collected during the 1994 and 1995 data taking. Due to the reasons discussed before, see Sec. 2.4.2 and 5.2, only the QED Compton event samples detected by means of the backward electromagnetic calorimeters (i.e. BEMC, SPACAL) and classified by the already described selection procedures were studied.

The QED Compton events as events with very simple final state, i.e. two coplanar electromagnetic particles scattered into the backward region with the well defined relations between the corresponding measured clusters energies and their polar angles, see Sec. 2.3, provide a very useful experimental tools for understanding some of the basic characteristics of the electromagnetic calorimeters. Therefore the first part of this chapter is devoted to the methodological studies to improve the understanding of backward electromagnetic calorimeters in terms of absolute energy scale, response linearity, relative position to the beam, the misalignment of both BPC-BEMC and BDC-SPACAL system, respectively. Here, the BPC efficiency measurement, the evaluation of the probability of γ-conversion and consequently the estimation of the amount of the dead material in front of the BPC-BEMC and BDC-SPACAL system are presented as well.

Since the cross section of the QED Compton events is well calculable in frame of QED, see Chapter 2, an independent of the H1 luminosity system measurement (cross-check) of the luminosity could be introduced. The luminosity measurement using the samples of QED Compton is the subject of the second part of this chapter.

6.1   Study of BEMC QED Compton Event Sample

Since the cross-section of the QED Compton event is rather small, (approximately two orders of magnitude smaller compared to the DIS processes), the number of events which passed the whole selection procedure is consequently small. Usually, energy calibration of the new calorimeter is based on the test beam studies. The procedure of moving the body of the detector and its electronics from the laboratory environment and its installation in the experimental apparatus such as the H1 detector is not a simple task. In addition the placement of the BEMC in the H1 environment, see Sec. 3.3, was such that a considerable amount of the dead material was in front of it. Therefore additional calibration

methods were employed to improve our knowledge of its characteristics. Those methods could be based on the different physical processes such as the DIS – kinematical peak method [62, 63]; double angle method [64, 65]; detection of cosmics [69], π^0-mesons [65], scalar vector mesons [66, 68] or the QED Compton events [34]. This kind of calibration approaches is provided by a sufficient amount of the data per "unit" of the calibrated detector limited either by a hardware segment (stack, cell) or a bin in a pre-defined grid (e.g. binning in the $r - \phi$ or xy-plane of the front face of the calorimeter). The amount of the 1994 QED Compton data did not allow neither a segmentation neither a finer division of the front face of detector into some larger parts according to the shower center-of-gravity or the corresponding tracking information. Hence only the global characteristics could be calculated. Consequently, the QED Compton method was presently only suitable for cross-checking the results obtained from other method like kinematical peak or double angle method.

Although the QED Compton method was limited by the smaller amount of data there were some crucial advantages compared to another calibration methods:

- In comparison with the kinematical peak method [62, 63] the QED Compton method is independent of the Monte Carlo simulations, hence it is suitable for the absolute energy calibration.

- Comparing to the double angle method [64, 65] which is successfully used for calibration of the energy spectrum in the kinematical peak region ($E_{cl} > 20$ GeV) it provides the information about the detector in "the middle range" of the energy spectrum of the electron scattered into the backward region ($E_{cl} \simeq 8 - 20$ GeV). To complete these two mentioned above methods in terms of lower cluster energies for SPACAL calorimeter one of the methods based on cosmics [69], halo muons [67], π^0-mesons [65, 68], and scalar vector mesons [66, 68] is to be used in contrary to BEMC calorimeter where only the QED Compton events were employable. That was provided by negligible noise of the SPACAL read-out which was based on photo-multipliers, see Sec. 3.4.2.

- The QED Compton method provided the only possibility to measure the response linearity of the BEMC detector in the H1 environment.

As it was mentioned before due to the limited amount of statistics only global characteristics were possible to be given. Therefore the procedure of calculation and consequently the over-all characteristics (results of the analyses) should not be influenced by the difference of the understanding between the well understood parts of detector and more difficult ones, which were either understood less precise or the corrections have larger errors, e.g. the inner region of the BEMC detector equipped with triangular stacks, see Sec. 3.3.2. In order to get rid of them the fiducial cut was imposed and for different calibration studies only the data samples with "closed triangle" (data samples 1, 2, 3) were only used.

In order to suppress the radiative QED Compton events and to limit the contribution of the inelastic channel of the QED Compton process following additional cuts were imposed:

- To make the kinematic relations "more valid" in the sense of the assumption $Q^2 \to 0$ GeV^2 it was, according to Eq. (2.61), required:

$$\frac{|E_e - E_{cl_1}(1 - \cos\theta_{cl_1}) - E_{cl_2}(1 - \cos\theta_{cl_2})|}{2\,E_e} < 0.1 \qquad (6.1)$$

where E_e is the electron beam energy, E_{cl_1}, E_{cl_2} and θ_{cl_1}, θ_{cl_2} are the cluster energies and the corresponding polar angles of the first two BEMC clusters with the highest energies, respectively.

- To limit the contribution of the inelastic channel of the QED Compton process as it was suggested in [61] additional cut on the transversal momentum of the $(e - \gamma)$ system was imposed and the coplanarity cut was tighten:

$$|\vec{p}_t| < 1.0 \text{ GeV} \quad \text{and} \quad 180° - |\phi_{cl_1} - \phi_{cl_2}| < 7° \qquad (6.2)$$

where $|\vec{p}_t|$ is the transversal momentum of the $(e - \gamma)$ system, and ϕ_{cl_1}, ϕ_{cl_2} are the azimuthal angles of the first two most energetic BEMC cluster, respectively.

6.1.1 BEMC Absolute Energy Scale

In order to study the absolute energy scale of the BEMC detector the relation, Eq. (2.62), was employed in the following way:

$$E'_{cl_1\,(cl_2)}(\theta_{cl_1}, \theta_{cl_2}) = \frac{2E_e \sin\theta_{cl_2\,(cl_1)}}{\sin\theta_{cl_1} + \sin\theta_{cl_2} - \sin(\theta_{cl_1} + \theta_{cl_2})} , \qquad (6.3)$$

where E_{cl_1}, E_{cl_2} and θ_{cl_1}, θ_{cl_2} are the cluster energies and the corresponding polar angles of the first two BEMC clusters with the highest energies, respectively. The calibration factor κ could be introduced as:

$$E_{cl_i} = \kappa\, E_{cl_i}^{H1}, \qquad i = 1, 2 \qquad (6.4)$$

where E_{cl_i}, $E_{cl_i}^{H1}$, $i = 1, 2$, are the calibrated and measured energies of the first and second clusters, respectively. The measured energies $E_{cl_i}^{H1}$, $i = 1, 2$ are the ones after the dead material and crack corrections (i.e. stored in BCFR bank in reconstruction procedure). The value of calibration factor κ is found by minimizing the distribution of χ_i^2, $i = 1, 2$:

1. Each measured cluster energy and its corresponding calculated energy provide the possibility of the calibration of the calorimeter for each cluster separately and thus double the statistics. The minimized χ_1^2-distribution is then defined as:

$$\chi_1^2 = \sum_{j=1}^{N} \sum_{i=1}^{2} \left(\frac{\Delta E_i^j}{\sigma_{cl_i}^j}\right)^2, \qquad (6.5)$$

where N is the number of events, ΔE_i^j is given by

$$\Delta E_i^j = E_{cl_i}^j(\theta_{cl_1}, \theta_{cl_2}) - E_{cl_i}^j, \qquad (6.6)$$

with $E_{cl_i}^j(\theta_{cl_1}, \theta_{cl_2})$, $i = 1, 2$ determined by Eq. (6.3). For the estimation of the dispersion $\sigma_{cl_i}^j$ the two following approaches were used:

(a) According to [34]:

$$\frac{\Delta E_i^j}{\sqrt{E_i^j}} = \frac{\sigma_{cl_i}^j}{\sqrt{E_i^j}} = R_0, \tag{6.7}$$

$$\sigma_{cl_i}^j = R_0 \sqrt{E_i^j}, \tag{6.8}$$

where R_0 is the experimental dispersion of the $\Delta E/\sqrt{E}$ distribution determined by a Gaussian fit, see Fig. 6.1.a.

(b) The energy resolution of the BEMC calorimeter could be described by the resolution function [24], which will be discussed in more details further:

$$\frac{\sigma}{E} = \frac{0.39(2)}{E} \oplus \frac{0.100(3)}{\sqrt{E}} \oplus 0.017(5) \quad (E \text{ in GeV}). \tag{6.9}$$

This can be used for the estimation of the error in the following way:

$$\sigma_{cl_i}^j = 0.39 + 0.10 \sqrt{E_{cl_i}^j} + 0.02 E_{cl_i}^j, \quad i = 1, 2 \quad (E_{cl_i}^j \text{ in GeV}). \tag{6.10}$$

2. Since the value of ΔE, and consequently the calibration procedure, is sensitive to the error of energy and polar angle measurements yet another method could be used. The value of the calibration factor κ is found by minimizing the χ_2^2-distribution:

$$\chi_2^2 = \sum_{j=1}^{N} \left(\frac{\Delta E_1^j + \Delta E_2^j}{\tilde{\sigma}^j} \right)^2, \tag{6.11}$$

where for the dispersion $\tilde{\sigma}^j$ the following estimation can be used:

(a) According to [34]:

$$\tilde{\sigma}^j = R_1 \sqrt{E_{cl_1} + E_{cl_2}}, \tag{6.12}$$

where R_1 is the experimental dispersion of the $\frac{\Delta E_1 + \Delta E_2}{\sqrt{E(\theta)_1 + E(\theta)_2}}$ distribution determined by a Gaussian fit, see Fig. 6.1.b.

(b) or similarly to Eq. (6.10) using the resolution function (the factor $\sqrt{2}$ stands for the incoherence sum of noise of the two clusters):

$$\tilde{\sigma}^j = \sqrt{2}\, 0.39 + 0.10 \sqrt{E_{cl_1}^j + E_{cl_2}^j} + 0.02 \left(E_{cl_1}^j + E_{cl_2}^j\right) \quad (E_{cl_i}^j \text{ in GeV}). \tag{6.13}$$

In this way four different χ^2s were constructed and compared, see Fig. 6.2. All four obtained calibration factors, see Tab. 6.1, showed that the BEMC absolute energy scale was well understood (beyond 0.5%).

Although the errors of the calibration factors are the same comparing the four different χ^2-distributions the difference of their shapes indicated:

1. The χ_2^2-method, Eq. (6.11), of extracting the global calibration factor κ is more precise than χ_1^2-method, Eq. (6.5), because:
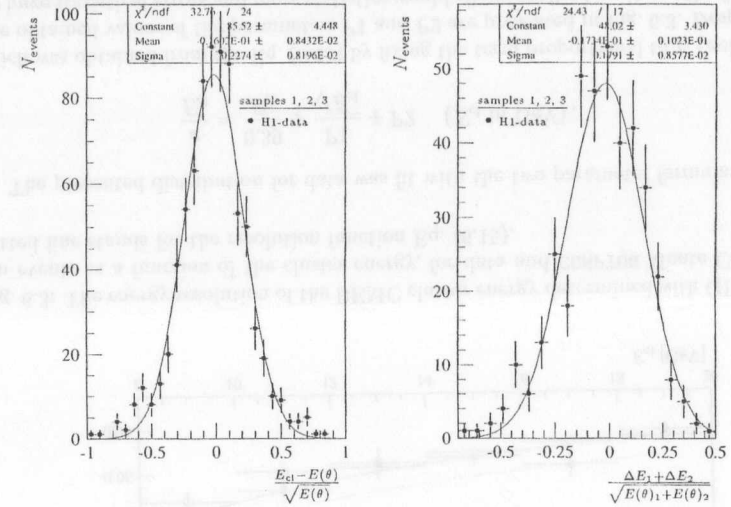
Fig. 6.1: The Gaussian fits for extracting the σ's.

(a) The χ_2^2-method, Eq. (6.11), uses only the half of the statistics of the χ_1^2-method, Eq. (6.5),

(b) the shape of the χ_2^2-distributions, Eq. (6.11), is narrower compared to the χ_1^2-distributions, Eq. (6.5). Notice the difference between the shapes of the curves for the two estimations of the dispersion separately, i.e. compare χ_{2a}^2 to χ_{1a}^2 and χ_{2b}^2 to χ_{1b}^2, as shown in Fig. 6.2.a and in Fig. 6.2.b, respectively.

2. The estimations of the dispersion based on the resolution function, i.e. Eq. (6.10) and Eq. (6.13) are more precise because the minimum values of these χ^2-distributions which use them, i.e. χ_{2a}^2 and χ_{2b}^2, is closer to 1 then those which use the estimations of the dispersion extracted from the Gaussian fit of the experimental distributions. This indicates that the errors of obtained calibration factors are better understood.

χ^2	error estimation	calibration factor
χ_{1a}^2	Eq. (6.8)	$\kappa_{1a}^{min} = 0.997 \pm 0.002$
χ_{1b}^2	Eq. (6.10)	$\kappa_{1b}^{min} = 0.997 \pm 0.002$
χ_{2a}^2	Eq. (6.12)	$\kappa_{2a}^{min} = 1.002 \pm 0.002$
χ_{2b}^2	Eq. (6.13)	$\kappa_{2b}^{min} = 1.002 \pm 0.002$

Tab. 6.1: The obtained calibration factors.
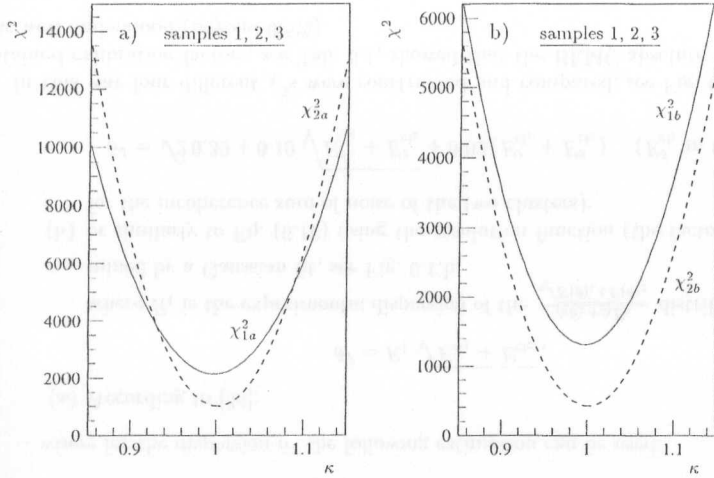
Fig. 6.2: The χ_1^2 and χ_2^2 distributions as functions of the calibration factors for (a) the errors estimated according to Eq. (6.8), Eq.(6.12) and (b) using the Eq. (6.10), Eq. (6.13). The minima are $\kappa_{1a}^{min} = 0.997 \pm 0.002$, $\kappa_{2a}^{min} = 1.002 \pm 0.002$, $\kappa_{1b}^{min} = 0.997 \pm 0.002$ and $\kappa_{2b}^{min} = 1.002 \pm 0.002$ respectively. The full line stands for the χ_1^2, Eq. (6.5) and the dashed line for χ_2^2, Eq. (6.11). Note the difference between the shapes which is narrow and the value of χ^2 in the minimum, which is lower for the χ_2^2-method compared to χ_1^2-method.

6.1.2   BEMC Energy Resolution

The energy resolution of the BEMC was measured using the test beams of different energies (from 5 to 60 GeV) at CERN and DESY (from 1 to 6 GeV) [24]. The resolution function has three following terms: The photo-diode readout and pre-amplifier noise leads to the constant noise term, which was measured to be 93 MeV. Sampling fluctuations are proportional to $\sqrt{E}$. A term proportional to E characterized the contribution of the leakage due to the limited depth of the stacks. These tree terms provided the following resolution function:

$$\frac{\sigma}{E} = \frac{0.097(6)}{E} \oplus \frac{0.100(3)}{\sqrt{E}} \oplus 0.010(3) \quad (E \text{ in GeV}). \tag{6.14}$$

In the H1 environment it is possible to extract the information about the energy resolution indirectly from the high energy side of the kinematical peak, which is dominated by calorimeter resolution. The test beam's resolution function Eq. (6.14) was adopted for the BEMC calorimeter in the H1 environment taking into account the fact that the electron energy is reconstructed from the most energetic stack and its neighbors, so-called leading cluster. Therefore the noise term is increased by factor $\sqrt{9} = 3$ with respect to a single stack. This together with the additional change of the shaping time constant lead

to the below indicated noise contribution. The sampling structure stayed unchanged. Therefore the sampling term was fixed to 100 MeV$^{1/2}$. The stack-to-stack variations although minimized by the individual stack calibration detoriated the resolution together with the inhomogeneities of the energy response especially near the borders of the stacks. These factors increased the constant term. An adjustment based upon the Monte Carlo simulated electron response provided a value of 1.7 %. The BEMC resolution function is then given by:

$$\frac{\sigma}{E} = \frac{0.39(2)}{E} \oplus \frac{0.100(3)}{\sqrt{E}} \oplus 0.017(5) \quad (E \text{ in GeV}). \tag{6.15}$$

By means of the QED Compton event sample an attempt to measure directly the energy resolution of the BEMC detector in the H1 environment was done. A Gaussian fit of the difference between the calculated and measured cluster energies in selected energy bins reveals the mean position and the experimental dispersion σ. The distribution of σ/E_{cl} for selected cluster energy bins was obtained for both the data and Monte Carlo samples, see Fig. 6.3. The vertical error bars indicate the errors of the mean position of these fits whereas horizontal ones are the energy bin widths.
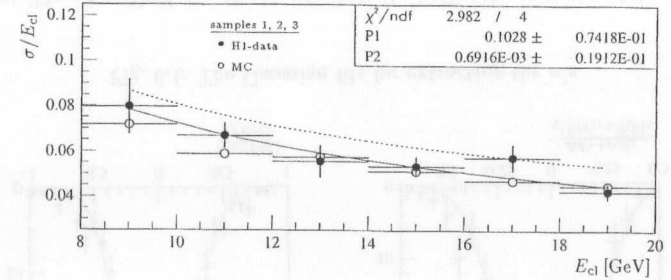
Fig. 6.3: The energy resolution of the BEMC cluster energy determined with QED Compton events as a function of the cluster energy, for data and COMPTON Monte Carlo. The dotted line stands for the resolution function Eq. (6.15).

The presented distribution for data was fit with the two parameter formula:

$$\frac{\sigma}{E_{cl}} = \frac{0.39}{E_{cl}} + \frac{P1}{\sqrt{E_{cl}}} + P2 \quad (E_{cl} \text{ in GeV}), \tag{6.16}$$

which was obtained from the Eq. (6.15) by fixing the term proportional to E (noise term). The obtained values of the parameters P1 and P2 are presented in Fig. 6.3. Despite there are huge statistical errors and more statistics would allow smaller bins it was the first direct measurement of the energy resolution in situ detector. It provided a comparable result although only a small part of the energy interval compared to the test beam measurement was used. To complete it a possible solution would be to use other calibration methods e.g. double angle method, π^0-method.

6.1.3 Response Linearity of BEMC Detector

The QED Compton events were used to verify the response linearity of the BEMC in the H1 detector. On the basis of the cluster position the expected energies can be calculated using the relation Eq. (6.3). A Gaussian fit of the difference between calculated and measured cluster energies in six selected energy bins reveals the mean position shown in Fig. 6.4. The vertical error bars indicate the errors of the mean position fits whereas horizontal ones are the energy bin widths. This data confirmed the linearity of the BEMC electromagnetic scale to within 1% in the range from approximately 5 to 22 GeV (restricted by energy requirements applied to a non-leading cluster).
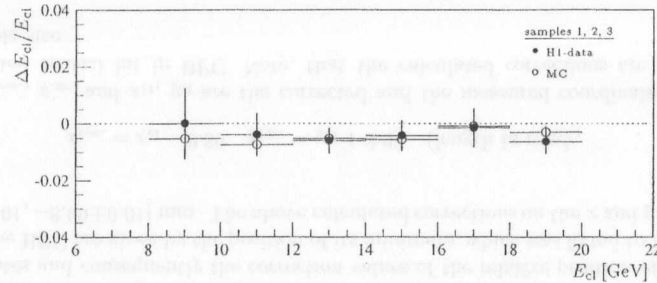
Fig. 6.4: The linearity of the BEMC determined with QED Compton events as a function of the cluster energy, for data and COMPTON Monte Carlo.

6.1.4 Relative Position of BEMC versus Beam

From the point of view of the measurement of the polar angle θ, calculated from the coordinates of the shower center-of-gravity and the coordinates of the interaction vertex it was of great importance to control the relative position of of the BEMC detector to the beam. The absolute x and y coordinates of the electromagnetic clusters (given by the shower center-of-gravity) measured in the H1 coordinate system by means of the BEMC could be spoilt by:

1. The misplacement of the BEMC during the setting up the whole H1 detector,

2. different x and y position of the beam during the different running periods or luminosity fills.

In the here performed determination of the relative position of the BEMC versus the beam the following assumptions were made:

1. For events without the reconstructed z-vertex position the position $[0, 0, 0]$ cm was assumed,

2. no beam tilt correction was applied,

3. only the misplacement of the BEMC versus the beam in xy-plane was considered (i.e. no rotations were taken into account).

Substituting the measured values of the polar angles of the two clusters in Eq. (6.3) with the following calculated values:

$$\theta_{cl_i} = \arctan\left(\sqrt{\frac{(x_{cl_i} - x_0)^2 + (y_{cl_i} - y_0)^2}{(z_{cl_i} - z_{vtx})^2}}\right), \qquad (6.17)$$

where $x_{cl_i}, y_{cl_i}, z_{cl_i}$ are the coordinates of the shower center of gravity of the i-th BEMC cluster and z_{vtx} is the z coordinate of the vertex, the cluster energies could be calculated and the following two-dimensional χ_4^2-distribution could be constructed:

$$\chi_4^2 = \sum_{j=1}^{N} \sum_{i=1}^{2} \left(\frac{\Delta E_i^j}{\sigma_{cl_i}^j}\right). \qquad (6.18)$$

N is the number of events. For $\sigma_{cl_i}^j$, $i = 1, 2$ the resolution function Eq. (6.10) was used, and ΔE_i^j was defined:

$$\Delta E_i^j = E_{cl_i}^j(\theta_{cl_1}, \theta_{cl_2}) - E_{cl_i}^j. \qquad (6.19)$$

In the case of well placed xy-plane of the BEMC detector the minimum of the χ_4^2 is to be $[x_0, y_0] = [0, 0]$ cm. The distribution of the χ_4^2 is shown in Fig. 6.5. The coordinates and consequently the correction values of the relative position of the BEMC with respect to the beam are given by the minimum, which is $[x_0, y_0] = [-5.64 \pm 0.01, 1.66 \pm 0.01]$ mm. The above calculated corrections on the x and y coordinates are:

$$x_{beam.cor.} = x_{cl} + 5.64, \quad y_{beam.cor.} = y_{cl} - 1.66 \quad \text{(length in mm)}, \qquad (6.20)$$

where $x_{beam.cor.}$, $y_{beam.cor.}$ and x_{cl}, y_{cl} are the corrected and the measured coordinates of the shower center-of-gravity of the BEMC cluster. Note, that the calculated corrections are of the very reasonable size.

6.1.5 Relative Position of BEMC versus BPC

In analogy with the previous Section the relative position of the BEMC with respect to BPC was studied. It might have been changed during the setting up the whole H1 detector, although the BPC chamber was fixed to the surface of the BEMC.

In order to evaluate the relative shift of the two detectors in the xy-plane of the following χ_5^2-distribution was constructed:

$$\chi_5^2 = \sum_{i=1}^{N_{cl_{BPC}}} \left[(x_{cl} - x_0 - x_{BPC})^2 + (y_{cl} - y_0 - y_{BPC})^2\right]_i, \qquad (6.21)$$
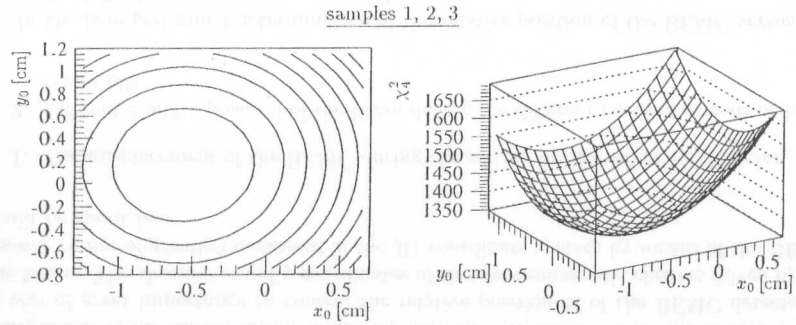
Fig. 6.5: The χ_4^2 distributions as a function of the $[x_0, y_0]$ for determination of the relative position of the BEMC versus the beam.

where $N_{cl_{BPC}}$ is number of clusters which have the associated reconstructed BPC hit, x_{BPC} and y_{BPC} are the x and y coordinates of the reconstructed BPC hit closest to the shower center-of-gravity of the corresponding BEMC cluster.

The χ_5^2-distribution for the QED Compton event sample is shown in Fig. 6.6. The coordinates and consequently the correction values of the relative position of the BEMC versus the BPC are given by the position of its minimum, which was found to be $[x_0, y_0] = [0.86\pm0.01, -8.09\pm0.01]$ mm. The above calculated corrections on the x and y coordinates are:

$$x_{cor.} = x_{cl} - 0.86 \quad y_{cor.} = y_{cl} + 8.09 \quad \text{(length in mm)}, \tag{6.22}$$

where $x_{cor.}$, $y_{cor.}$ and x_{cl}, y_{cl} are the corrected and the measured coordinates of the reconstructed spatial hit in BPC. Note, that the calculated corrections are of the very reasonable size.

6.1.6 BPC Efficiency Measurement, Evaluation of Probability of γ-Conversion and Estimation of Dead Material in front of BPC-BEMC System

The BEMC QED Compton event sample as a sample of events which final state consists only of two particles, i.e. one charged (electron) and one neutral (photon), were used for the BPC efficiency measurement, evaluation of the probability of γ-conversion and consequently the estimation of the amount of the dead material in front of the BPC-BEMC system. The all three methods were based on the assumptions that electron as charged particle should be always detected as an electromagnetic cluster with corresponding reconstructed track information, in contrary to the photon which was expected as an electromagnetic cluster without any tracking information.

The inefficiency of the BPC could cause that there were QED Compton events without any BPC information and on the other hand the γ-conversion in the dead material in
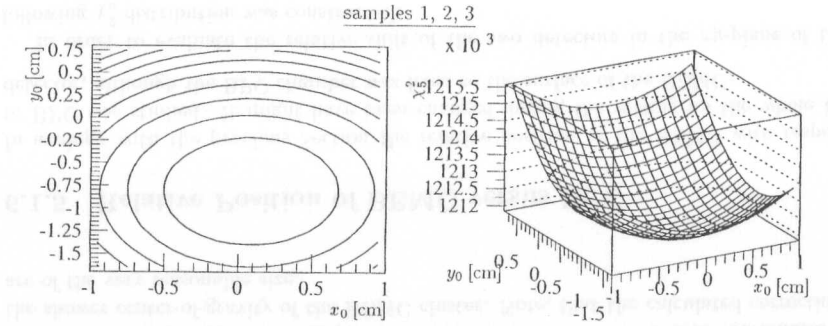
Fig. 6.6: The χ_5^2 distributions as a function of the $[x_0, y_0]$ for determination of the relative position of the BEMC versus the BPC.

front of BPC-BEMC system could result in a detected QED Compton event with two corresponding BPC points.

According to [34] calculating N_0, the number of events without any reconstructed spatial BPC point associated with the corresponding BEMC cluster; N_1 ,the number of events with only one reconstructed spatial BPC point associated with corresponding BEMC cluster and N_2, the number of events in which both BEMC clusters had corresponding reconstructed spatial BPC hit the total number of events N was divided into the three groups, while:

$$N = N_0 + N_1 + N_2. \tag{6.23}$$

If ϵ_{BPC} is the efficiency of the BPC, and α_c is the probability that the γ-conversion is detected, then:

$$N_0 = [(1 - \epsilon_{BPC})(1 - \alpha_c)]N, \tag{6.24}$$
$$N_1 = [(1 - \epsilon_{BPC})\alpha_c + (1 - \alpha_c)\epsilon_{BPC}]N, \tag{6.25}$$
$$N_2 = \epsilon_{BPC}\alpha_c N. \tag{6.26}$$

And using last three relations together with Eq. (6.23) the BPC efficiency, ϵ_{BPC}, and the probability that the γ-conversion is detected, α_c, is then given by:

$$\epsilon_{BPC} = \frac{N_1 + 2N_2 + \sqrt{N_1^2 - 4N_0N_2}}{2N}, \tag{6.27}$$

$$\alpha_c = \frac{N_1 + 2N_2 - \sqrt{N_1^2 - 4N_0N_2}}{2N}. \tag{6.28}$$

Since α_c represents the probability that at least electron or positron (one of these two particles) from the γ-conversion is detected, we can write:

$$\alpha_c = \tau_c \epsilon_{BPC}^2 + 2\tau_c \epsilon_{BPC}(1 - \epsilon_{BPC}) = \epsilon_{BPC}(2 - \epsilon_{BPC})\tau_c, \tag{6.29}$$

where τ_c is the probability of the γ-conversion in front of BPC-BEMC system and is given by:

$$\tau_c = \frac{\alpha_c}{\epsilon_{BPC}\left(2 - \epsilon_{BPC}\right)} . \tag{6.30}$$

The statistical errors of the measurement of the BPC efficiency, ϵ_{BPC}, and the probability of the γ-conversion, τ_c, are

$$\Delta\epsilon_{BPC} = \sqrt{\frac{\epsilon_{BPC}\left(1 - \epsilon_{BPC}\right)}{N}} , \tag{6.31}$$

$$\Delta\tau_c = \sqrt{\frac{\tau_c\left(1 - \tau_c\right)}{N}} . \tag{6.32}$$

Using the described above method the global BPC efficiency for the each given run period was calculated, and the probability of γ-conversion in front of BPC-BEMC system was evaluated. In the further step using the obtained values of τ_c the dead material in front of the BPC-BEMC was estimated applying the relation between the number of photons which convert into e^+e^--pair $N_{e^+e^-}$ and the number of the photons N_γ penetrating through the material of the thickness x, which is according to [71]:

$$N_{e^+e^-} = N_\gamma \left[1 - \exp\left(-\frac{7}{9}\frac{x}{X_0}\right)\right] , \tag{6.33}$$

where from the thickness of the dead material x:

$$x = -\frac{9}{7} X_0 \ln(1 - \tau_c) . \tag{6.34}$$

The BPC efficiency measurement, the probability of γ-conversion and the estimation of the amount of the dead material in front of the BPC-BEMC system as a function of the run number is presented in Fig. 6.7, 6.8 and 6.9, respectively.
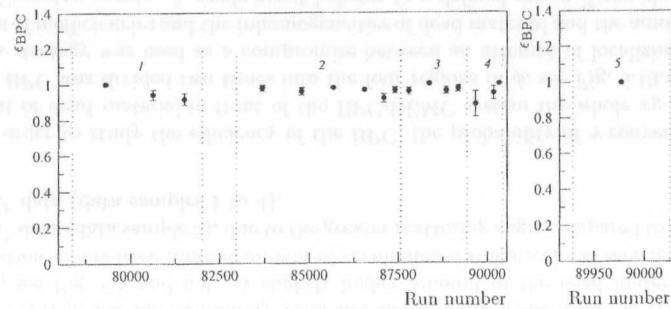
Fig. 6.7: The BPC efficiency as a function of run number during the 1994 data taking. The different run periods are indicated with the dotted lines.

As it is shown in Fig. 6.7 the BPC was stable during the whole 1994 data taking, and its efficiency was very high, i.e. $> 96\%$ and even in some periods reaching the full 100%
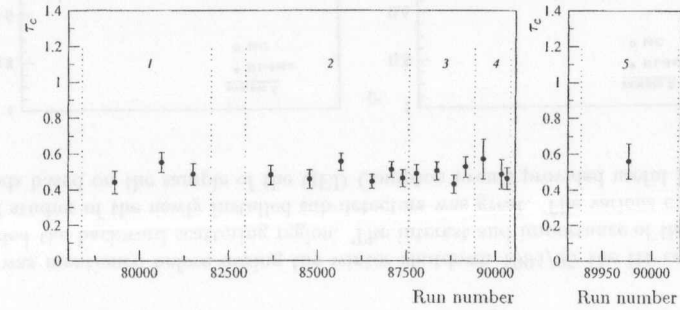
Fig. 6.8: The probability of the γ-conversion in front of the BPC-BEMC system as a function of run number during the 1994 data taking. The different run periods are indicated with the dotted lines.
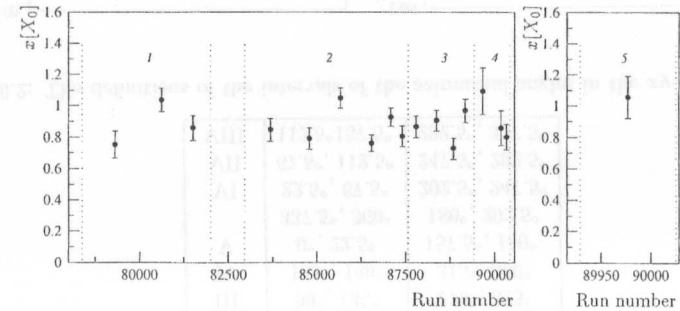
Fig. 6.9: The estimation of the amount of the dead material in front of the BPC-BEMC system as a function of run number during the 1994 data taking. The different run periods are indicated with the dotted lines.

efficiency. The probability of the γ-conversion in the dead material in front of the BPC-BEMC system was approximately 45%, and the amount of the dead material was about $0.9X_0$, see Fig. 6.8 and 6.9. A slightly higher amount of the dead material (even the estimation suffers from limited amount of accumulated statistics) was seen for the "shifted vertex" data (data sample 5), due to the greater scattering angle compared to the "nominal vertex" data (data samples 1 to 4).

In order to study the efficiency of the BPC, the probability of γ-conversion and the amount of dead material in front of the BPC-BEMC system the whole xy-cross section of the BPC was divided two times into the four regions in ϕ, see Fig. 6.10.a and 6.10.b. Such a strategy was used as a compromise between an attempt of localizing of possible regions of inefficiencies and the inhomogeneities of dead material and the amount of stored QED Compton events. A single event belongs to a defined region if one cluster has corresponding azimuthal angle in the first interval and the second cluster has corresponding azimuthal angle in the second interval in ϕ (marked with the same number) in order to follow the coplanar shape of the events. The definitions of the intervals are summarized in Tab. 6.2.
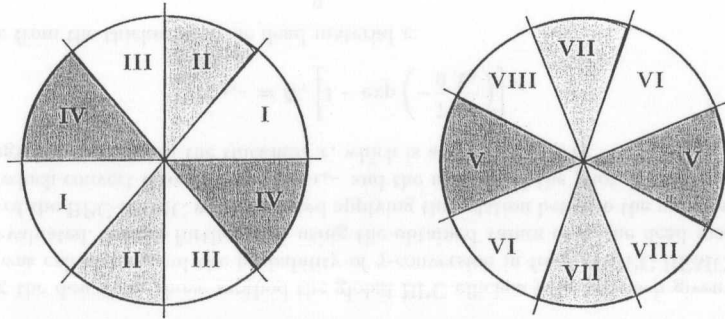
Fig. 6.10: Schematic view of the devision in xy-plane.

Using the described above method the efficiency of the BPC, the probability of γ-conversion and the amount of dead material in front of the BPC-BEMC system was calculated separately for each BPC region for both data and Monte Carlo data samples, see Fig. 6.11, 6.12 and 6.13.

The BPC efficiency, shown in Fig. 6.11, is underestimated but homogeneous in ϕ in Monte Carlo, in contrary to data, where there is an indication for a regions with lower and full BPC efficiencies. The probability of the γ-conversion and consequently the estimation of the amount of the dead material in front of the BPC-BEMC system is significantly underestimated in Monte Carlo compared to data, see Fig. 6.12, 6.13. For both the data and Monte Carlo the distributions are rather homogeneous in ϕ.

region	intervals of azimuthal angles	
	ϕ_i	ϕ_j
I	$0°$, $45°$	$180°$, $225°$
II	$45°$, $90°$	$225°$, $270°$
III	$90°$, $135°$	$270°$, $315°$
IV	$135°$, $180°$	$315°$, $360°$
V	$0°$, $22.5°$	$157.5°$, $180°$,
	$337.5°$, $360°$	$180°$, $202.5°$
VI	$22.5°$, $67.5°$	$202.5°$, $247.5°$
VII	$67.5°$, $112.5°$	$247.5°$, $292.5°$
VIII	$112.5°157.5°$	$292.5°$, $337.5°$

Tab. 6.2: The definitions of the intervals of the azimuthal angles in the xy-plane of the BPC.
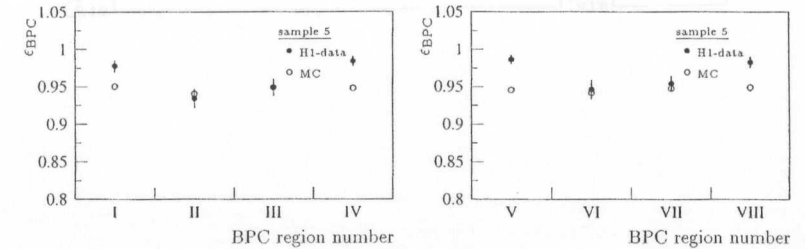
Fig. 6.11: The BPC efficiency in different ϕ regions.

6.2 Study of SPACAL QED Compton Event Sample

As it was mentioned before during the winter shutdown 1994/95 the H1 collaboration upgraded the backward scattering region. The interest and importance of the methodological studies of the newly installed sub-detectors was great. The various experimental methods based on the sample of the QED Compton events provided useful information
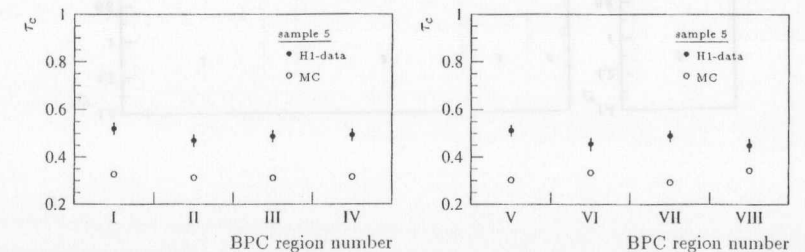
Fig. 6.12: The probability of the γ-conversion in the dead material in front of the different BPC ϕ regions.
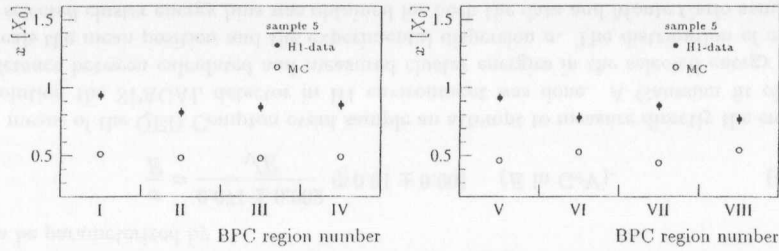
Fig. 6.13: The estimate of the dead material in front of the different ϕ regions of the BPC.

and thus helped first experiencing the new apparatus. These studies are the subject of this section. Since the methods used are in principle the same as used for BEMC only differences are discussed and presented.

Here it should be stressed that the here presented analysis were limited by the amount of accumulated QED Compton events due to the reasons discussed in Sec. 5.3.

In order to suppress the radiative QED Compton events and to limit the contribution of the inelastic channel of the QED Compton events additional cuts as in the BEMC analysis were imposed, Eq. (6.1) and (6.2).

6.2.1 SPACAL Absolute Energy Scale

In analogy to the BEMC QED Compton event analysis, the study of the absolute energy scale of the SPACAL detector, was based on the relation Eq. (6.3). The calibration factor κ was introduced as:

$$E_{cl_i} = \kappa E_{cl_i}^{H1}, \qquad i = 1, 2 \tag{6.35}$$

where E_{cl_i}, $E_{cl_i}^{H1}$, $i = 1, 2$, are the calibrated and measured energies of the first and second clusters, respectively. Since there were not any overall dead material corrections available in the reconstructure procedure the measured energies, $E_{cl_i}^{H1}$, $i = 1, 2$, are the ones without the dead material corrections (i.e. SCLR bank in reconstruction procedure), but corrected using the dead material correction for the inner part of the detector [63, 70] on the analysis level. The value of calibration factor κ is found by minimizing the distribution of χ_i^2, $i = 1, 2$, Eq. (6.5) and (6.11), while:

- The experimental dispersions R_0, R_1 of the $\Delta E/\sqrt{E}$ and $\frac{\Delta E_1 + \Delta E_2}{\sqrt{E(\theta)_1 + E(\theta)_2}}$ distribution were determined by a Gaussian fit, see Fig. 6.14.a and 6.14.b, respectively.

- Instead of Eq. (6.10) and (6.13) the modified estimations of the dispersion σ using the SPACAL resolution function [39]:

$$\frac{\sigma}{E} = \frac{0.071 \pm 0.002}{\sqrt{E}} \oplus 0.01 \pm 0.001 \quad (E \text{ in GeV}), \tag{6.36}$$

were introduced in the following way:

$$\sigma_{cl_i}^j = 0.07 \sqrt{E_{cl_i}^j} + 0.01 E_{cl_i}^j, \quad i = 1, 2, \quad (E_{cl_i}^j \text{ in GeV}) \tag{6.37}$$

and

$$\tilde{\sigma}^j = \sqrt{2}\, 0.07 \sqrt{E_{cl_1}^j + E_{cl_2}^j} + 0.01 \left(E_{cl_1}^j + E_{cl_2}^j \right) \quad (E_{cl_i}^j \text{ in GeV}). \tag{6.38}$$
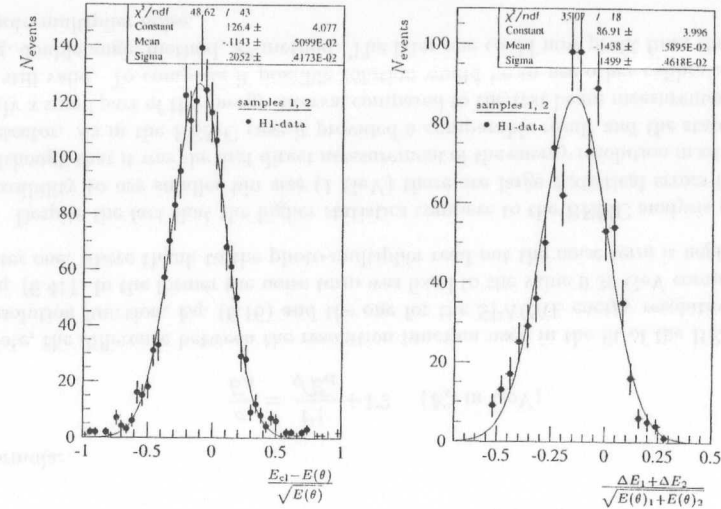
Fig. 6.14: The Gaussian fits for extracting the σ's.

In this way four different χ^2s were constructed and compared, see Fig. 6.2. All four obtained calibration factors, see Tab. 6.1, showed that the SPACAL absolute energy scale was undercalibrated by 2-3%.

χ^2	error estimation	calibration factor
χ_{1a}^2	Eq. (6.8)	$\kappa_{1a}^{min} = 1.021 \pm 0.001$
χ_{1b}^2	Eq. (6.37)	$\kappa_{1b}^{min} = 1.024 \pm 0.001$
χ_{2a}^2	Eq. (6.12)	$\kappa_{2a}^{min} = 1.027 \pm 0.001$
χ_{2b}^2	Eq. (6.38)	$\kappa_{2b}^{min} = 1.027 \pm 0.001$

Tab. 6.3: The obtained calibration factors.

6.2.2 SPACAL Energy Resolution

The energy resolution of the SPACAL was measured using the test beams of different energies (from 5 to 60 GeV) at CERN and DESY (from 2 to 6 GeV) [39]. Both the
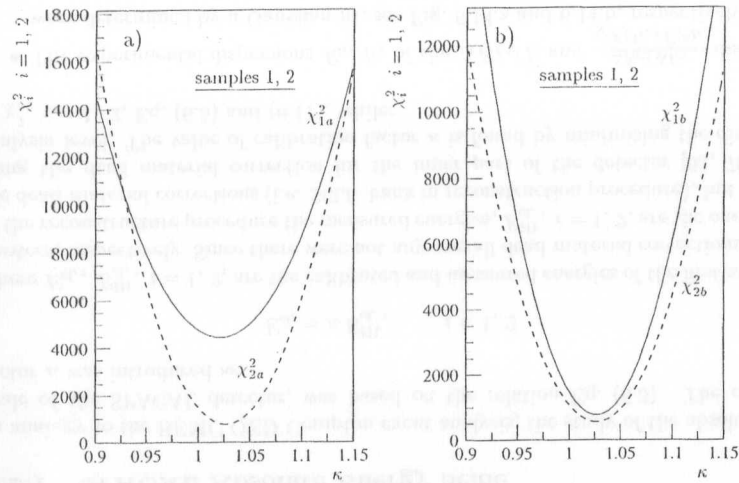
Fig. 6.15: The χ_1^2 and χ_2^2 distributions as functions of the calibration factors for (a) the errors estimated according to Eq. (6.8), Eq.(6.12) and (b) using the Eq. (6.37), Eq. (6.38). The minima are $\kappa_{1a}^{min} = 1.021 \pm 0.001$, $\kappa_{2a}^{min} = 1.027 \pm 0.001$, $\kappa_{1b}^{min} = 1.024 \pm 0.001$ and $\kappa_{2b}^{min} = 1.027 \pm 0.001$ respectively. The full line stands for the χ_1^2, Eq. (6.5) and the dashed line for χ_2^2, Eq. (6.11). Note the difference between the shapes which is narrow and the value of χ^2 in the minimum, which is lower for the χ_2^2-method compared to χ_1^2-method.

CERN and DESY measurements were combined and the normalized resolution σ/E was plotted versus $1/\sqrt{E}$ and analyzed using the resolution function:

$$\frac{\sigma}{E} = \frac{a}{\sqrt{E}} \oplus \frac{b}{E} \oplus c \quad (E \text{ in GeV}). \tag{6.39}$$

The result of the fit showed that the noise term is negligible and that the final resolution can be parameterized by

$$\frac{\sigma}{E} = \frac{0.071 \pm 0.002}{\sqrt{E}} \oplus 0.01 \pm 0.001 \quad (E \text{ in GeV}). \tag{6.40}$$

By means of the QED Compton event sample an attempt to measure directly the energy resolution the SPACAL detector in H1 environment was done. A Gaussian fit of the difference between calculated and measured cluster energies in the selected energy bins reveals the mean position and the experimental dispersion σ. The distribution of σ/E_{cl} for selected cluster energy bins was obtained for both the data and Monte Carlo samples, see Fig. 6.3. The vertical error bars indicate the errors of the mean position of these fits whereas horizontal ones are the energy bin widths.

In analogy with the test beam analysis which used the resolution function, Eq. (6.39), the presented distribution for data was fit, see Fig. 6.16, with the following two parameter
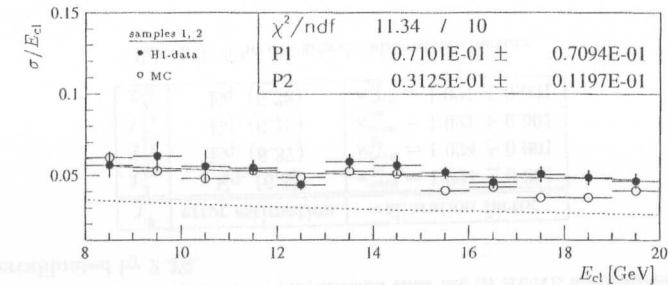
Fig. 6.16: The energy resolution of the SPACAL cluster energy determined with QED Compton events as a function of the cluster energy, for data and COMPTON Monte Carlo. The dotted line stands for the resolution function, Eq. (6.40).

formula:

$$\frac{\sigma}{E_{cl}} = \frac{P1}{\sqrt{E_{cl}}} + P2 \quad (E_{cl} \text{ in GeV}). \tag{6.41}$$

Note, the difference between the resolution function used in the fit of the BEMC energy resolution function, Eq. (6.16) and the one for the SPACAL energy resolution function, Eq. (6.41). In the former the noise term was fixed to the value 0.39 GeV compared to the later one, where thank to the photo-multiplier read-out the noise term is negligible.

Despite the fact that the higher statistics compare to the BEMC analysis provide the possibility to use smaller bin size (1 GeV) there are large statistical errors fluctuation. Although that it was the first direct measurement of the energy resolution in situ SPACAL detector. As in the BEMC case it provided a comparable result and the statement that only a small part of the energy interval compared to the test beam measurement was used is still valid. To complete it possible solution would be to use other calibration method e.g. double angle method, π^0-method. The later one could now profit from the negligible photo-multiplier noise.

6.2.3 Response Linearity of SPACAL Detector

The QED Compton events were used to verify the response linearity of the SPACAL in the H1 detector. A Gaussian fit of the difference between calculated and measured cluster energies in twelve selected energy bins reveals the mean position shown in Fig. 6.17. The vertical error bars indicate the errors of the mean position fits and the systematic error of the polar angle reconstruction whereas horizontal ones are the energy bin widths. This data confirms:

1. For both data and Monte Carlo there was the shift of the absolute energy scale by approximately 2% to the lower values of the cluster energies,

2. the response linearity of the SPACAL electromagnetic scale to within 1% in the range from approximately 10 to 20 GeV (restricted by energy requirements applied to a non-leading cluster),

3. and shows the non-linearity on the level of 3% of the SPACAL detector in the range of lower cluster energies (< 10 GeV).
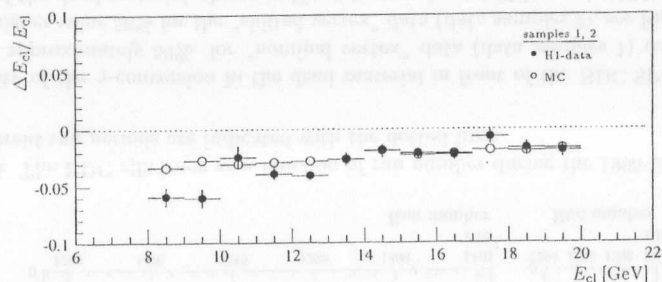
Fig. 6.17: The linearity of the SPACAL determined with QED Compton events as a function of the cluster energy, for data and COMPTON Monte Carlo.

6.2.4 Relative Position of SPACAL versus Beam

Using the same method as in the BEMC analysis, see Sec. 6.1.4, with only a small modification (i.e. the expression for $\sigma_{cl_i}^j$, Eq. (6.10) in the χ_4^2-distribution, Eq. (6.18), was substituted with the relevant one for SPACAL, Eq. (6.37)) the relative position of the SPACAL to the beam was determined.

The distribution of the χ_4^2 is shown in Fig. 6.18. The coordinates and consequently the correction values of the relative position of the SPACAL with respect to the beam are given by the minimum, which is $[x_0, y_0] = [0.87 \pm 0.01, 3.20 \pm 0.01]$ mm. Thus, corrections on the x and y coordinates are:

$$x_{\text{beam.cor.}} = x_{cl} - 0.87, \quad y_{\text{beam.cor.}} = y_{cl} - 3.20 \quad \text{(length in mm)}, \quad (6.42)$$

where $x_{\text{beam.cor.}}$, $y_{\text{beam.cor.}}$ and x_{cl}, y_{cl} are the corrected and the measured coordinates of the shower center-of-gravity of the SPACAL cluster. Note, that the calculated corrections are of the very reasonable size.

6.2.5 Relative Position of SPACAL versus BDC

In analogy with the determination of the the relative position of the BEMC with respect to BPC, see Sec. 6.1.5, the relative position of the SPACAL versus BDC was studied. It might have been changed during the setting up the whole H1 detector. In order to evaluate
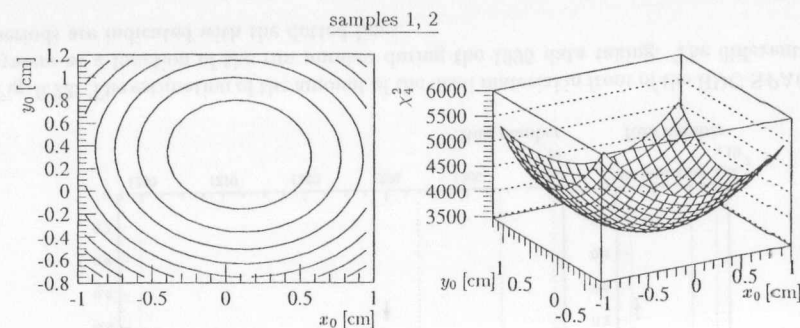
Fig. 6.18: The χ^2 distributions as a function of the x_0, y_0 for determination of the relative position of the SPACAL versus the beam.

the relative shift of the two detectors in the xy-plane the χ_5^2-distribution, Eq. (6.21), was used where $N_{cl_{BPC}}$ was substituted with $N_{cl_{BDC}}$ which is the number of clusters which have the associated reconstructed BDC track. Similarly, the x and y coordinates of the reconstructed BPC point closest to the shower center-of-gravity of the corresponding BEMC cluster x_{BPC} and y_{BPC} were exchanged by the x and y coordinates of the reconstructed BDC track closest to the shower center-of-gravity of the corresponding SPACAL cluster.

In this way modified χ_5^2-distribution for the 1995 QED Compton event sample is shown in Fig. 6.19. The coordinates and consequently the correction values of the relative position of the SPACAL versus the BDC are given by the position of its minimum, which was found to be $[x_0, y_0] = [6.78 \pm 0.01, 5.22 \pm 0.01]$ mm. Thus, the corrections on the x and y coordinates are:

$$x_{\text{cor.}} = x_{cl} - 6.78, \quad y_{\text{cor.}} = y_{cl} - 5.22, \quad \text{(length in mm)}, \quad (6.43)$$

where $x_{\text{cor.}}$, $y_{\text{cor.}}$ and x_{cl}, y_{cl} are the corrected and the measured coordinates of the shower center-of-gravity of the SPACAL cluster. Note, that the calculated corrections are of the very reasonable size.

6.2.6 BDC Efficiency Measurement, Evaluation of Probability of γ-Conversion and Estimation of Dead Material in front of BDC-SPACAL System

In this section using the methods described in Sec. 6.1.6 the global BDC efficiency was calculated, the probability of γ-conversion and the amount of the dead material in front of the BDC-SPACAL system was estimated. The results are shown in Fig. 6.20, 6.21 and 6.22 as a functions of the run number.

As it is shown in Fig. 6.20 the BDC was stable during the whole 1995 data taking, and its efficiency was very high, i.e. > 97% (in some periods reaching the 100%). The
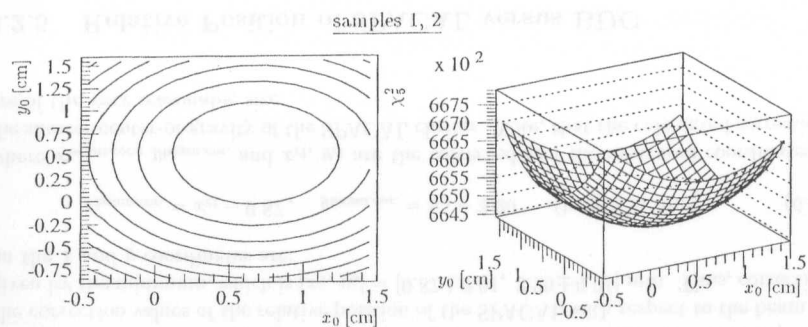
samples 1, 2

Fig. 6.19: The χ_5^2 distributions as a function of the x_0, y_0 for determination of the relative position of the SPACAL versus the BDC.
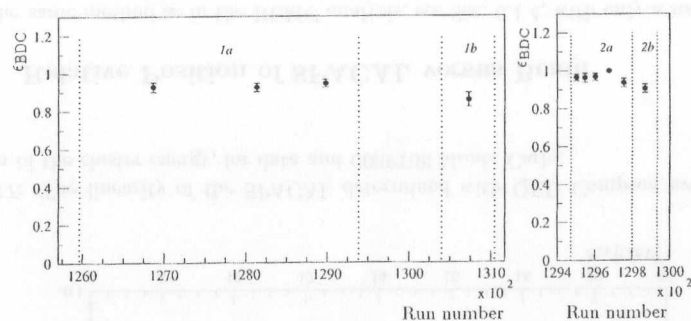
Fig. 6.20: The BDC efficiency as a function of run number during the 1995 data taking. The different run periods are indicated with the dotted lines.

probability of the γ-conversion in the dead material in front of the BDC-SPACAL system was approximately 50%, for "nominal vertex" data (data samples 1) compared to slightly higher value 58% for the "shifted vertex" data (data samples 2), see Fig. 6.8. The amount of the dead material, shown in Fig. 6.9, was about $0.95X_0$, and $1.10X_0$ for "nominal vertex" data (data samples 1) and "shifted vertex" data samples (data samples 2), respectively. These increases could be explained by a slightly higher amount of the dead material (even the estimation suffers from limited amount of accumulated statistics) which was observed for the "shifted vertex" data (data samples 2), due to the greater scattering angle compared to the "nominal vertex" data (data samples 1).

Since the amount of stored selected data sample was not larger enough compared to the ones used in BPC-BEMC analysis the same strategy of localizing the possible regions of inefficiencies and the inhomogeneities of dead material in front of the BDC-SPACAL system was used. The efficiency of the BDC, the probability of γ-conversion and the amount of dead material in front of the BDC-SPACAL system was calculated separately for each BDC region, defined in Tab. 6.2 and Fig. 6.10, for both data and Monte Carlo
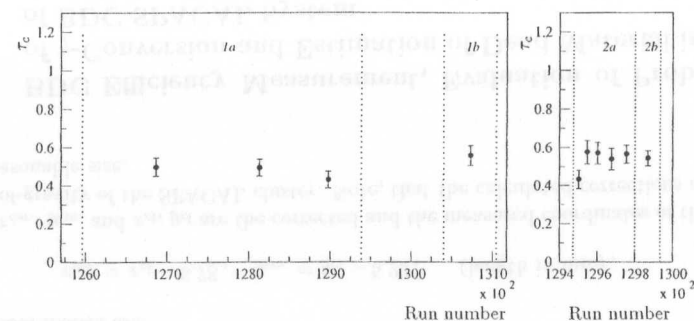
Fig. 6.21: The probability of the γ-conversion in front of the BDC-SPACAL system as a function of run number during the 1995 data taking. The different run periods are indicated with the dotted lines.
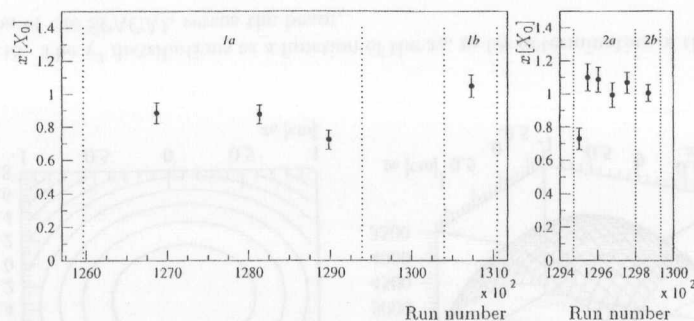
Fig. 6.22: The estimation of the amount of the dead material in front of the BDC-SPACAL system as a function of the run number during the 1995 data taking. The different run periods are indicated with the dotted lines.

data samples, see Fig. 6.23, 6.24 and 6.25, respectively.
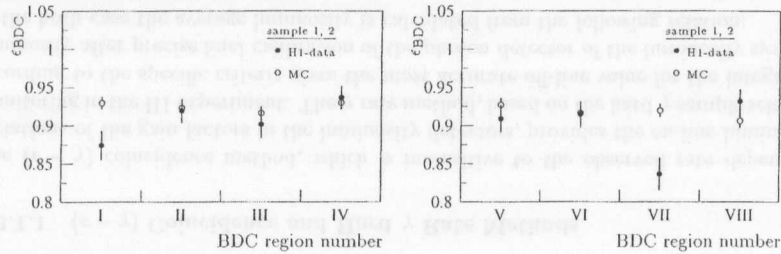
Fig. 6.23: The BDC efficiency in different ϕ regions.
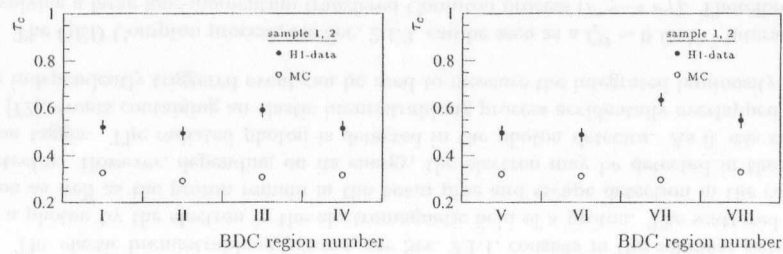
Fig. 6.24: The probability of the γ-conversion in the dead material in front of the different BDC ϕ regions.
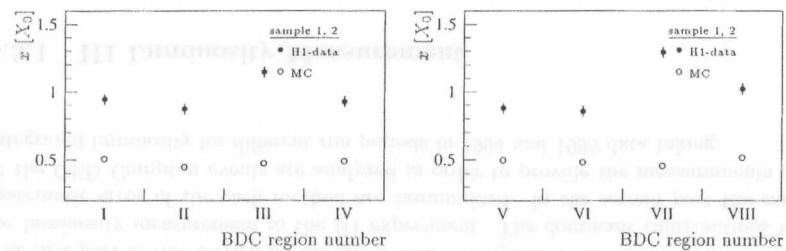
Fig. 6.25: The estimate of the dead material in front of the different ϕ regions of the BDC.

The BDC efficiency, shown in Fig. 6.23, is rather well described by Monte Carlo in all regions except regions I and VII. The BDC efficiency is homogeneous in ϕ in Monte Carlo, in contrary to data, where there is an indication for a regions with lower (in the problematic regions I and VII) and higher BDC efficiencies. The probability of the γ-conversion and consequently the estimation of the amount of the dead material in front

of the BDC-SPACAL system is significantly underestimated in Monte Carlo compared to data, see Fig. 6.24 and 6.25. For Monte Carlo the distributions are rather homogeneous in ϕ, which is in strong contradiction with distribution for data where there is a significantly higher probability of the γ-conversion and consequentially higher amount of dead material in front of the BDC-SPACAL system in the regions III and VIII. The later result agrees with the result of the analysis of the xy-distribution of collected charge by BDC [37]. It shows the higher amount of the dead material in front of the BDC in the ϕ-region III and VIII.

6.3   Luminosity Measurement Using QED Compton Method

The first part of this section is concerned with description of the different methods used for luminosity measurement in the H1 experiment. The dominant contributions to the systematic error of the each method are summarized. In the second part the samples of the QED Compton events are analyzed in order to provide the measurements of the integrated luminosity for different run periods in 1994 and 1995 data taking.

6.3.1   H1 Luminosity Measurement

In order to perform both the direct on-line luminosity monitoring and the off-line luminosity measurement a process with a well calculable cross section and the clear experimental signature has to be chosen. Suitable processes at HERA experiments are elastic bremsstrahlung process and QED Compton process.

The elastic bremsstrahlung process, see Sec. 2.1.1, consists in the collinear radiation of a photon by the electron in the electromagnetic field of a proton. The scattered electron as well as the proton remain in the beam pipe and escape detection in the central detector. However, depending on its energy, the electron may be detected in the electron tagger. The radiated photon is detected in the photon detector. As it was shown in [72], events containing an elastic bremsstrahlung process accidentally overlapped with an independently triggered event can be used to measure the integrated luminosity.

The QED Compton process, see Sec. 2.1.3, can be seen as a $Q^2 \sim 0$ GeV^2 interaction involving a large four-momentum transfered Compton process ($e^*\gamma \to e\gamma$). Therefore the final state only consists of a coplanar ($e - \gamma$) system, both observable in the central H1 detector.

6.3.1.1   ($e - \gamma$) Coincidence and Hard γ Rate Methods

The ($e - \gamma$) coincidence method, which is insensitive to the observed rate dependent variations of the gain factors in the luminosity detectors, provides the on-line luminosity monitoring in the H1 experiment. The γ rate method, based on the hard γ sample selected according to the specific criteria gives the most accurate off-line value for the integrated luminosity after precise final calibration of the photon detector of the luminosity system. In the both case the average luminosity is calculated from the following relation:

$$L = \frac{N_{data}(\Delta t) - N_{bgr}(\Delta t)}{\sigma_{BH}^{acc}\Delta t} , \qquad (6.44)$$

where $N_{data}(\Delta t)$ is the number of events satisfying the selection criteria for the given method collected in the time interval Δt and the $N_{bgr}(\Delta t)$ is the number of background events originating from the interactions of electrons with the residual gas in the beam

pipe. This number is measured using the non-colliding pilot bunches according to the following formula:

$$N_{bgr}(\Delta t) = \frac{I_{all}}{I_{pilot}}N_{pilot}(\Delta t) , \qquad (6.45)$$

where N_{pilot} is the number of accepted bremsstrahlung events originating from the pilot bunches, I_{pilot} is the current of these bunches and I_{all} is the total electron current. The acceptance corrected value of the cross section for bremsstrahlung events σ_{BH}^{acc} is calculated using the Bethe-Heitler formula [15]. The Eq. (6.45) is based on the assumption that the pilot and colliding electron bunches are equivalent in terms of the background rate per unit of current. This assumption was checked and verified with an accuracy of better than 1% [35].

The major contributions to the systematic error of the absolute luminosity measurement in the ($e - \gamma$) coincidence method are: (i) acceptance determination which mainly affects the on-line monitoring where only the electron beam tilt is measured, in contrary to the off-line measurement when the actual acceptance of the electron tagger is determined from the data; (ii) background subtraction; (iii) trigger efficiency and purity, which could be minimized for both the on-line and off-line errors by requiring that the minimal energies are well above the thresholds for both the electron tagger and the photon detector.

The value of the systematic error of the luminosity measurement using the hard γ rate depends on: (i) the absolute energy calibration and resolution of the photon detector; (ii) its trigger efficiency; (iii) background subtraction and effect of multiple photons. The latest effect is taken into account although the probability of having more than one photon ($E'_\gamma > 0.3$ GeV) in the same bunch crossing, which can influence the shape of the reconstructed photon energy spectrum is small.

6.3.1.2   Random Coincidence Method

In order to measure the integrated luminosity using events containing an elastic bremsstrahlung process accidentally overlapped with an independently triggered event the sample of the random events is to be selected according the following criteria [72]:

1. Photon energy $E'_\gamma \geq 5$ GeV ,

2. an reconstructed electromagnetic cluster in the backward electromagnetic calorimeter with $E'_e \geq 25$ GeV.

Such energy requirements reject all radiative DIS events with a photon emitted in the acceptance region of the photon detector. We determine first the average conditional probability P_{DIS-B} that a bremsstrahlung event satisfying requirement 1 happen to occur in the same bunch crossing as a DIS event satisfying requirement 2. This probability is given by $P_{DIS-B} = N_{1,2}/N_2$, where $N_{1,2}$ is the number of random coincidences satisfying both criteria 1 and 2, and N_2 is the number of events fulfilling the condition 2. If the luminosity were constant over a given running period then P_{DIS-B} would be equal to the probability P_{BC-B}, of registering a bremsstrahlung event in any randomly chosen bunch

crossing. In reality the instantaneous luminosity varies with each electron and proton fill of the HERA storage rings and is unevenly distributed over the colliding bunches. Therefore, $P_{BC-B} = (1-\kappa)P_{DIS-B}$, where κ is an average correction for the time variation of the instantaneous luminosity. This correction was determined using the time variation of the $(e - \gamma)$ coincidence rate and was found to be $(5 \pm 1)\%$ [82]. This correction is insensitive to both the absolute calibration of the luminosity system and the selection criteria for bremsstrahlung events.

Having determined P_{BC-B} we calculate the total number of bremsstrahlung events fulfilling requirement 1 as: $N_{BC-B}(\Delta t) = P_{BC-B} \times N_{\text{bunch}}(\Delta t)$, where $N_{\text{bunch}}(\Delta t)$ is the integrated number of bunch crossings over the time interval Δt. The corresponding luminosity is then calculated using the formula:

$$L = \frac{N_{BC-B}(\Delta t) - N_{bgr}(\Delta t)}{\sigma_{BH}^{acc}\Delta t} , \qquad (6.46)$$

The resulting integrated luminosity is independent of the efficiency of the photon detector trigger. Thus, the systematic errors for this method come from the same sources as for the hard γ method except that there is no error due to uncertainties in the trigger efficiency but an additional 1% error due to κ. This results in the total systematic error of 2.8% and the measurement error that is dominated by the statistical precision.

6.3.1.3   QED Compton Method

In order to determine the integrated luminosity $\mathcal{L}_{\text{QEDC}}$ from the measured sample of the QED Compton events we used the following formula:

$$\mathcal{L}_{\text{QEDC}} = \frac{N_{\text{QEDC}} - N_{bg}}{N_{\text{MC}}} \frac{1}{\epsilon_{sel}} \mathcal{L}_{\text{MC}} , \qquad (6.47)$$

where N_{QEDC} is the number of selected QED Compton events, N_{bg} is the number of background events remaining in the selected sample (see below), N_{MC} is the number of Monte Carlo simulated QED Compton events which were subjected to the same reconstruction and analysis chain as the real data, ϵ_{sel} is the efficiency of the QED Compton event selection and $\mathcal{L}_{\text{MC}}$ is the integrated luminosity corresponding to the generated Monte Carlo QED Compton event sample.

6.3.2   Determination of 1994 Total Integrated Luminosity

In the following the total integrated luminosity using the sample of the QED Compton events recorded during 1994 data taking is measured. The stability of the QED Compton method during the whole data taking is checked. To determine the amount of the background events which remain in the selected samples a Monte Carlo study was performed. The different sources of uncertainties of here presented measurement has been studied in order to estimate the total systematic error. Finally, the results are presented and their comparison with the both H1 luminosity system measurement and random coincidence method is shown.

6.3.2.1   Stability of QED Compton Method

In order to study the stability of the luminosity measurement using the sample of QED Compton events each run period was divided into intervals with comparable values of integrated luminosity, $\mathcal{L}_{\text{H1-LS}}$, determined by luminosity system. The distribution of the ratio of number of QED Compton events, N_{QEDC}, to $\mathcal{L}_{\text{H1-LS}}$ calculated for each subinterval as a function of run numbers is depicted in Fig. 6.26.
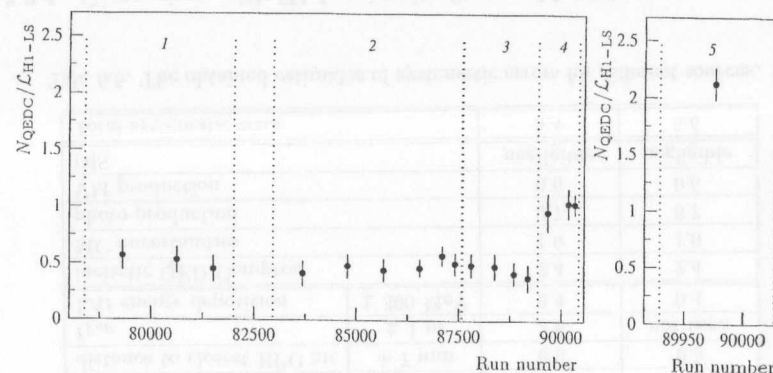
Fig. 6.26: The stability of the ratio of number of QED Compton events, N_{QEDC}, to integrated luminosity determined by the luminosity system of H1 detector, $\mathcal{L}_{\text{H1-LS}}$, for different run period. The error bars stand only for statistical errors. The dotted lines define the intervals of run periods. The ratio $N_{\text{QEDC}}/\mathcal{L}_{\text{H1-LS}}$ is higher in run periods with "open" BEMC triangular stacks (period 4) due to enlarging the BEMC geometrical acceptance closer to the beam pipe and hence to the higher value of polar angles of scattered particles. Similarly, running with open BEMC triangular stacks and with shifted z-position of the nominal vertex to the forward direction (period 5) increases the ratio $N_{\text{QEDC}}/\mathcal{L}_{\text{H1-LS}}$ even more.

It shows that the presented method is stable within the interval of statistical errors for periods with closed (periods 1, 2, 3) and opened BEMC triangles (period 4). Including the four innermost triangular stacks into the trigger increases acceptance of the BEMC closer to the beam pipe and thus to the higher values of the polar angle of the scattered particles $\theta_{e(\gamma)}$. As it was shown in Chapter 2, the cross section of quasi-real QED Compton process strongly increases with the $\theta_{e(\gamma)}$. Therefore the value of the ratio $N_{\text{QEDC}}/\mathcal{L}_{\text{H1-LS}}$ is higher in run periods with open BEMC triangular stacks (period 4) and with shifted z-position of the nominal vertex (period 5).

6.3.2.2   Remaining Background Contribution

In this section the possible background processes to the QED Compton event samples from the ep interactions were studied. The following three processes with the given below event topology were considered:

- photo-production events in which energy clusters from the hadronic final state mimic the topology of a QED Compton event;

- diffractive production of vector mesons (VM) processes (mostly dominated by the elastic ρ^0 production at low-Q^2 and high-W_h) where the scattered electron is detected in the BEMC, and one of the produced pions escapes the central detector along the beam pipe, but in which the second pion fakes a scattered photon. Although this configuration should result in the experimental signal composed of two clusters and two corresponding tracks, i.e. one additional track to the experimental signature of the QED Compton event, the clean identification is not unambiguous due to both the limited geometrical acceptance of the tracking detectors and the rather large probability of the γ-conversion in the dead material in the backward scattering region, see Sec. 6.1.6;

- deep inelastic scattering (DIS) characterized by very low-x and low-Q^2, where the scattered electron is correctly identified as an energy cluster in BEMC, but in which an energy from the *hadronic* final state fakes a scattered photon.

In order to evaluate the possible contributions of listed above background processes to the selected samples of QED Compton events the Monte Carlo samples generated by PHOJET [109], RAYVDM [81] and DJANGO [95], respectively, were used. For the events generated with the appropriate models the detector response was simulated in detail [12] using a program based on GEANT [110]. Consequently, the simulated Monte Carlo events were subjected to the same reconstruction and analysis chain as the real data and tested whether they satisfy all selection criteria. All these fake events which survived all steps of just described procedure were considered as remaining contribution of given background processes. According to the corresponding values of integrated luminosity the fractions of such events, in the selected sample of the QED Compton events were evaluated, see Tab. 6.4.

Process	Background contribution
photo-production	2.6 ± 0.6 %
VM production	1.6 ± 0.5 %
DIS[1]	negligible

Tab. 6.4: The obtained Monte Carlo estimates of background processes to the QED Compton event sample from the ep interactions.

6.3.2.3   Estimation of Systematic Errors

For the luminosity determination via the QED Compton method there are four main groups of the sources of the systematic errors:

- Systematic effects of the apparatus, mainly the backward electromagnetic calorimeter. Its energy and space resolution, the cluster radius determination, and its electronic noise are the crucial issues in minimizing the systematics.

---
[1]Note, that only DIS events with in the text specified event topology were considered.

- The uncertainty of the control on the inelastic QED Compton contribution, which was estimated from the observed tail of the acoplanarity distribution to be of 2.4%.

- According to [35] the theoretical uncertainties in the Monte Carlo, related to the uncertainty in the elastic proton form factor.

- The uncertainty of the estimation of different background processes contribution.

The obtained estimates of different sources of systematic errors together with the total value of systematic error of the QED Compton method are presented in the Tab. 6.5 for both the "open" and "closed triangle" data samples. Comparing the "closed triangle" and "open triangle" data samples one can see that the total systematic error for open triangular data is a little bit higher mainly because of the worse cluster radius determination in the inner triangular stacks. The smaller contribution of the BPC hit position cut to the total systematic error is due to the reduced geometrical acceptance in the beam pipe region, i.e. that it does not cover all the active surface of the BEMC.

Source	Variation	syst. error closed tr.[%]	syst. error open tr. [%]
BEMC energy scale	$\pm 1\%$	0.8	1.0
BEMC cluster radius	± 5 mm	2.0	3.6
BEMC noise cut	± 350 MeV	2.3	2.3
acoplanarity restriction	$\pm 2.5°$	2.0	2.0
distance to closest BPC hit	± 7 mm	0.9	0.5
t_{ToF}	± 1 ns	2.6	not used
LAr energy deposition	± 300 MeV	0.4	0.4
inelastic QED Compton		2.4	2.4
MC uncertainties		1.0	1.0
photo-production		0.7	0.7
VM production		0.6	0.6
DIS		negligible	negligible
Total systematic error		5.4	5.6

Tab. 6.5: The obtained estimates of systematic errors for different sources.

6.3.2.4   Comparison with H1 Luminosity System Measurement

In this section the results of the integrated luminosity measurement using the QED Compton method are presented and compared with results obtained by both the H1 luminosity system (H1-LS) measurement, which refers to the hard γ rate method, and random coincidence method.

The final results of here presented analysis of integrated luminosity measurement using the QED Compton samples in 1994 are shown in Fig. 6.27.a and 6.27.b for the "closed triangle" and "open triangle" data samples, respectively.

In addition, the results of the H1-LS method and the random coincidence method are presented. Since the H1-LS method provides values with the smallest errors compared to

the two other methods, the ratios of results of those two to the ones determined by H1-LS were calculated, see Fig. 6.27.c and 6.27.d. Before comparing the obtained results, note the two following remarks:
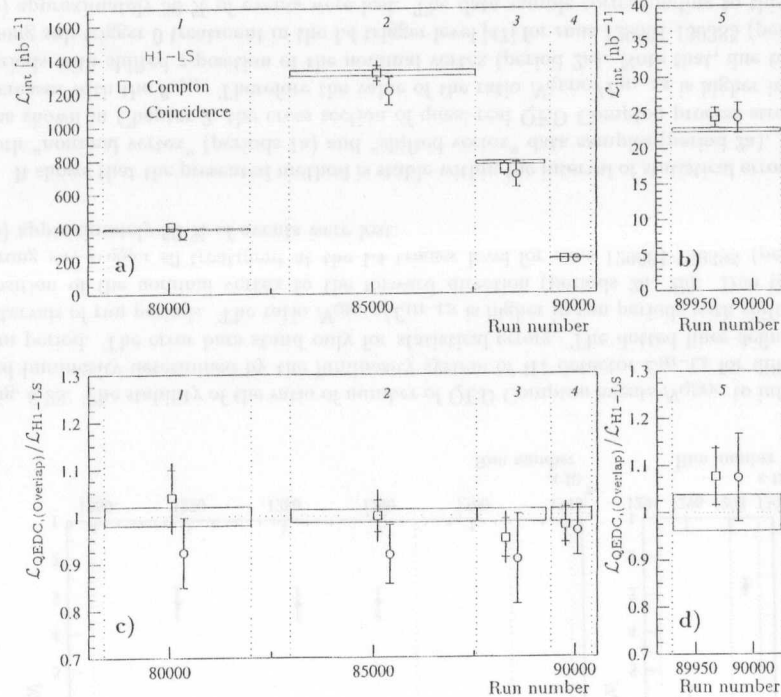
Fig. 6.27: The comparison of obtained results of integrated luminosities using different methods for a given run periods during the 1994 data taking. Whilst the dotted lines define the intervals of run periods, the integer numbers indicate the different data samples, see Tab. 5.1 in Chapter 5.

1. Both the random coincidence and the H1-LS methods do not include the data acquisition dead time compared to the QED Compton method. In order to compare the values of integrated luminosities delivered in the interaction region of the central detector of the H1 experiment the dead time value has been introduced, for each run, in the two dead time independent methods.

2. All here presented methods of luminosity measurement include the contribution of satellite bunches.[2] No such corrections have been introduced neither on the analyzed samples of QED Compton events, nor on values determined using the random coincidence and the H1-LS method used for comparison.

Comparing the results obtained using the QED Compton method we can conclude, that:

1. the values of integrated luminosity measured by the QED Compton method are in agreement within one sigma statistical error with other values measured by means of the other two methods, and thus confirm the H1 luminosity measurement;

2. the total error of the values of integrated luminosity determined by the QED Compton method are larger compared to the for H1 LS measurement, but comparable (even slightly smaller) with the ones obtained by the random coincidence method;

3. in order to lower both the statistical and the systematic error of the integrated luminosity measurement using the QED Compton method:

   • the amount of accumulated QED Compton events has to be enlarged, which could be achieved by increasing the total amount of delivered luminosity by HERA machine in the H1 scattering region and/or by increasing the geometrical acceptance of the electromagnetic calorimeter covering the backward scattering region,

   • the improvement of the measurement of the scattered electron and photon in the H1 backward scattering region in terms of improved measurement of the cluster parameters and the more precise determination of the azimuthal angles of the scattered electron and photon for coplanarity determination will be required.

The latest was planned and achieved during the 1994/95 winter shutdown when the H1 collaboration has upgraded the backward scattering region of the H1 experiment. The integrated luminosity measurement using QED Compton events detected by means of the newly installed detectors in the 1995 data taking is the subject of the next section.

6.3.3 Determination of 1995 Total Integrated Luminosity

As it was mentioned before during the 1994/95 winter shutdown the H1 collaboration has upgraded the H1 detector with a new backward calorimeter of the spaghetti (SPACAL) lead-fiber design and the new backward tracking detector (BDC), see Sec. 3.4. The increased geometrical acceptance of the BDC-SPACAL system in the upgraded H1 detector provides the possibility to to detect scattered electrons and photons at large values of the polar angles ($\theta_{e(\gamma)} \lesssim 178°$ in the 1995 "shifted vertex" data samples).

The total integrated luminosity using the samples of the QED Compton events recorded during the last few weeks of the 1995 data taking is measured. Similarly to the 1994 analysis first the stability of the QED Compton method is shown, then the background processes to the QED Compton process from the ep interaction are studied and the systematic errors are estimated. Finally, the results are presented and their comparison with the H1 luminosity system measurement is shown.

---

[2]The parasitic satellite bunches are formed during the bunch length compression when a small fraction of proton current escapes from main bunches [18].

6.3.3.1   Stability of QED Compton Method

In order to study the stability of the luminosity measurement using the sample of QED Compton events each run period was divided into intervals with comparable values of integrated luminosity, $\mathcal{L}_{H1-LS}$, determined by luminosity system. The distribution of the ratio of number of QED Compton events, N_{QEDC}, to $\mathcal{L}_{H1-LS}$ calculated for each subinterval as a function of run numbers is depicted in Fig. 6.28.
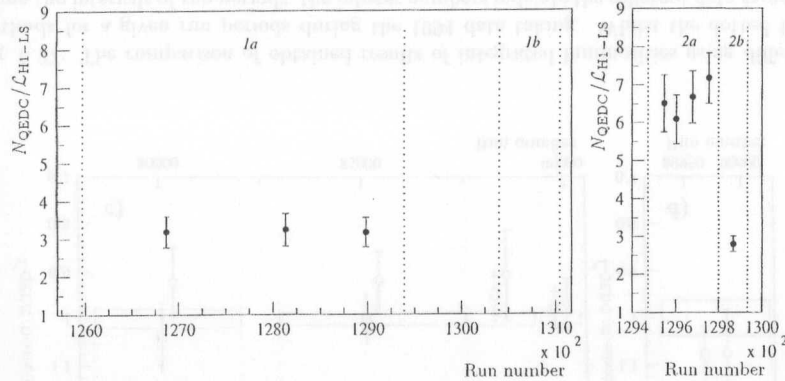
Fig. 6.28: The stability of the ratio of number of QED Compton events N_{QEDC} to integrated luminosity determined by the luminosity system of H1 detector $\mathcal{L}_{H1-LS}$ for different run period. The error bars stand only for statistical errors. The dotted lines define the intervals of run periods. The ratio $N_{QEDC}/\mathcal{L}_{H1-LS}$ is higher in run periods with shifted z-position of the nominal vertex to the forward direction (periods 2a, 2b). Due to the wrong sub-trigger s0 treatment at the L4 trigger level for runs 129801-130385 (periods 2b) approximately 50 % of events were lost.

It shows that the presented method is stable within the interval of statistical errors for both "nominal vertex" (periods 1a) and "shifted vertex" data samples (period 2a). As it was shown in Chapter 2, the cross section of quasi-real QED Compton process strongly increases with the $\theta_{e(\gamma)}$. Therefore the value of the ratio N_{QEDC}/L_{H1-LS} is higher in run periods with shifted z-position of the nominal vertex (period 2a). Note that, due to the wrong sub-trigger 0 treatment in the L4 trigger level [47] for runs 129801-130385 (periods 2b) approximately 50 % of events were lost. The data sample corresponding to this run range were thus excluded from the further analysis.

6.3.3.2   Remaining Background Contribution

In the 1995 data analysis the possible background processes to the QED Compton event samples from the ep interactions were studied. The following three processes with the given below event topology were considered:

- photo-production events in which energy clusters from the hadronic final state mimic the topology of a QED Compton event;

- diffractive production of vector mesons (VM) processes (mostly dominated by the elastic ρ^0 production at low-Q^2 and high-W_h) where the scattered electron is detected in the SPACAL, and one of the produced pions escapes the central detector along the beam pipe, but in which the second pion fakes a scattered photon. Although this configuration should result in the experimental signal composed of two clusters and two corresponding tracks, i.e. one additional track to the experimental signature of the QED Compton event, the clean identification is not unambiguous due to both the limited geometrical acceptance of the tracking detectors and the rather large probability of the γ-conversion in the dead material in the backward scattering region, see Sec. 6.1.6;

- deep inelastic scattering (DIS) characterized by very low-x and low-Q^2, where the scattered electron is correctly identified as an energy cluster in BEMC, but in which an energy from the *hadronic* final state fakes a scattered photon.

In order to evaluate the possible contributions of listed above background processes to the selected samples of QED Compton events the Monte Carlo samples generated by PHOJET [109], RAYVDM [81] and DJANGO [95], respectively, were used. Compared to the 1994 analysis here the contribution of elastic dissociative ρ^0 and ϕ production was investigated separately. For the events generated with the appropriate models the same algorithm as in 1994 analysis, see Sec. 6.3.2.2, was employed. The determined fractions of background events are presented in Tab. 6.6.

Process		Background contribution
photo-production		1.1 ± 0.5 %
VM production	elastic ρ	0.3 ± 0.3 %
	dissociative ρ	0.2 ± 0.2 %
	ϕ el., disoc.	negligible
DIS[3]		negligible

Tab. 6.6: The obtained Monte Carlo estimates of background processes to the QED Compton event sample from the ep interactions.

Comparing the obtained estimates for the 1994 and 1995 data analysis one can conclude that, the background contribution is significantly smaller in 1995. This was achieved mainly by means of higher value of the lower limit imposed on the visible energy and a tighten acoplanarity restriction, which was provided by the improved measurements of the cluster parameters of newly installed detectors in the H1 backward scattering region.

6.3.3.3   Estimation of Systematic Errors

For the luminosity determination via the QED Compton method there are four main groups of the sources of the systematic errors:

---

[3]Note, that only DIS events with in the text specified event topology were considered.

- Systematic effects of the apparatus, mainly the backward electromagnetic calorimeter. Its energy and space resolution, the cluster radius determination, and its electronic noise are the crucial issues in minimizing the systematics.

- The uncertainty of the control on the inelastic QED Compton contribution, which was estimated from the observed tail of the acoplanarity distribution to be of 2.0%.

- According to [35] the theoretical uncertainties in the Monte Carlo, related to the uncertainty in the elastic proton form factor.

- The uncertainty of the estimation of different background processes contribution.

The obtained estimates of different sources of systematic errors together with the total value of systematic error of the QED Compton method are presented in the Tab. 6.7 for both the "nominal vertex" and "shifted vertex" data samples.

Source	Variation	systematic error	
		"nominal vertex"	"shifted vertex"
SPACAL energy scale	$\pm 2.5\%$	1.3	0.5
SPACAL cluster radius	± 2 mm	0.9	3.4
SPACAL veto/noise cut	± 50 MeV	3.2	0.5
acoplanarity restriction	$\pm 3°$	1.1	0.5
inelastic QED Compton		2.0	2.0
MC uncertainties		1.0	1.0
photo-production		0.5	0.5
VM production		0.4	0.4
DIS		negligible	negligible
Total systematic error		4.4	4.2

Tab. 6.7: The obtained estimates of systematic errors for different sources.

6.3.3.4   Comparison with H1 Luminosity System Measurement

In this section the results of the integrated luminosity measurement using the QED Compton method are presented and compared with results obtained by the H1 luminosity system (H1-LS) measurement, which refers to the hard γ rate method.

The final results of here presented analysis of integrated luminosity measurement using the QED Compton samples in 1995 are shown in Fig. 6.29.a and 6.29.b for "nominal vertex" and "shifted vertex" data samples, respectively. In addition, the results of the H1-LS method are presented. The ratio of results obtained using the QED Compton method to the ones determined by H1-LS were calculated, see Fig. 6.29.c and 6.29.d. Before comparing the obtained results we repeat the analogical two remarks concerning the introduction of the dead time value in the H1-LS method and the absence of the satellite bunches correction in both here discussed method of luminosity measurement.

Comparing the results obtained using the QED Compton method we can conclude, that:
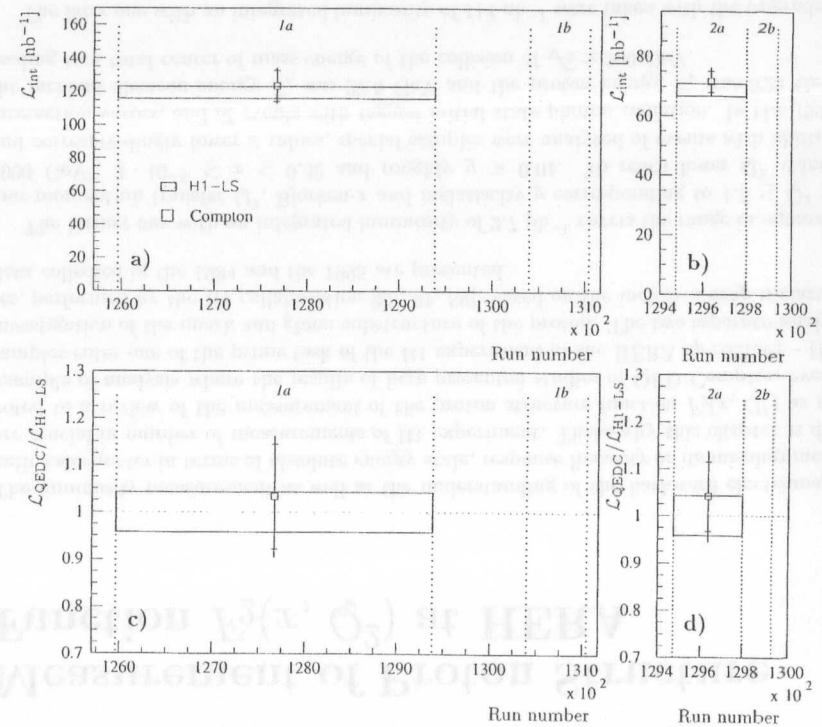
Fig. 6.29: The comparison of obtained results of integrated luminosities using different methods for a given run periods during the 1995 data taking. Whilst the dotted lines define the intervals of run periods, the integer numbers indicate the different data samples, see Tab. 5.2 in Chapter 5.

1. the values of integrated luminosity measured using the QED Compton method are in agreement within one sigma statistical error with values measured by means of H1-LS method, and thus confirm the H1 luminosity measurement;

2. the total error of the values of integrated luminosity determined by the QED Compton method are larger compared to that of the H1-LS measurement;

3. in order to lower both the statistical and the systematic error of the integrated luminosity measurement using the QED Compton method:

   - the amount of accumulated QED Compton events has to be enlarged, which could be achieved by increasing the total amount of delivered luminosity by HERA machine in the H1 scattering region and/or by improved triggering e.g. such as using the higher level of H1 trigger system. A solution of special dedicated trigger based on topological requirements of the SPACAL trigger element was tested at the end of 1995 data taking and result in the running a so-called QED Compton L2 topological trigger machine [73, 74]. In order to further increase the efficiency of the whole QED Compton event trigger chain and additionally to decrease the amount of recorded background events a special level L4 trigger QED Compton finder was installed [75].

   - the further improvement of the measurement of the scattered electron and photon in the H1 backward scattering region in terms of improved measurement of the cluster parameters and the precise determination of the azimuthal angles of the scattered electron and photon for coplanarity determination is required. This could be achieved by using the newly installed backward silicon tracker [76].

Chapter 7

Measurement of Proton Structure Function $F_2(x, Q^2)$ at HERA

The luminosity measurement as well as the understanding of the backward electromagnetic calorimeter in terms of absolute energy scale, response linearity or its misalignment are crucial in number of measurements of H1 experiment. Thats-why this chapter is devoted to a review of the measurement of the proton structure function $F_2(x, Q^2)$ as an example of analysis where the results of here presented studies of QED Compton event samples enter one of the prime task of the H1 experiment at the HERA ep-collider – the investigation of the quark and gluon substructure of the proton. The two separate analyses, performed by the H1 collaboration [88, 91, 89], based on the inclusive deep-inelastic data collected in the 1994 and the 1995 are presented.

The former one with an integrated luminosity of 2.7 pb^{-1} covers the range in squared four-momentum transfer Q^2, Bjorken-x and inelasticity y corresponding to $1.5 \leq Q^2 \leq 5000$ GeV^2, $3 \cdot 10^{-5} \leq x \leq 0.32$ and roughly $y > 0.01$. To reach lower Q^2 values and correspondingly lower x values, special samples were analyzed of events with shifted interaction vertex, and of events with tagged initial state photon radiation. In the 1994 the incident electron energy E_e was 27.5 GeV and the proton energy E_p was 820 GeV leading to a total center of mass energy of the collision of $\sqrt{s} \simeq 300$ GeV.

The later one with an integrated luminosity of 114 nb^{-1} were taken with the upgraded detector components, described in Sec. 3.2, which compared with the detector used up to the end of 1994, has resulted in an increased acceptance of electrons scattered through small angles (large θ_e), in improved granularity and in improved resolution. When taken together with the hadronic energy measurement these features have greatly facilitated the recognition and removal of background when selecting DIS events, and have extended the available kinematic range of the measurement. The data used for this analysis result from a short data taking period where the ep collision vertex was shifted by 70 cm in the proton-beam direction with respect to the nominal vertex position to increase the acceptance for the electrons scattered through small angles. As a result the data have an acceptance in Q^2 down to $Q^2 \sim 0.3$ GeV^2. The 1995 data taken with the same incident electron and proton energy as used in 1994 date taking covers the the kinematic range corresponding to $0.35 \leq Q^2 \leq 3.5$ GeV^2, $x \geq 6 \cdot 10^{-6}$ and $0.03 \leq y \leq 0.75$.

This chapter is organized as follows. After a short introduction to the kinematics of inclusive ep scattering in Sec. 7.1, the Monte Carlo simulation are described in Sec. 7.2. Next the different 1994 and 1995 data samples and the event selection including the background rejection are discussed in Sec. 7.3 for the different data samples used. Sec. 7.4 describes the F_2 analyses and the results are discussed with the respect to the results obtained in the here presented analyses of the QED Compton events in Sec. 7.5.

7.1   Kinematics

The structure function $F_2(x, Q^2)$ is derived from the inclusive electron-proton scattering cross section. It depends on the squared four-momentum transfer Q^2 and the scaling variable x. These variables are related to the inelasticity parameter y and to the total squared center of mass energy of the collision s since $Q^2 = xys$ with $s = 4E_eE_p$, where E_e and E_p are the energy of incoming electron and proton, respectively. A salient feature of the HERA collider experiments is the possibility of measuring not only the scattered electron but also the complete hadronic final state, apart from losses near the beam pipe. This means that the kinematic variables x, y and Q^2 can be determined with complementary methods which are sensitive to different systematic effects. These methods were exploited and detailed already in [77] which describes the analysis of the 1993 data. An appropriate combination of the results ensures maximum coverage of the available kinematic range with reasonable systematic errors. In addition the application of different methods is an important cross check of the results.

The methods used in the analysis of the 1994 data are the so-called "E" (electron) method using only the information of the scattered electron and the so-called "Σ" method (Σ) calculating the kinematics based on both the scattered electron and the hadronic final state measurements [78]. The E method, which is independent of the hadronic final state, apart from the requirement that the interaction vertex is reconstructed using the final state hadrons, has at large y the best resolution in x and Q^2 but needs sizeable radiative corrections. At low y the E method is not applied due to the degradation of the y_e (index e y_e indicates that the inelasticity parameter y was calculated using the E method) resolution as $1/y$. The Σ method, which has small radiative corrections, relies mostly on the hadronic measurement which has still an acceptable resolution at low y values and can be used from very low to large y values. The E and Σ results were compared in order to control the calculation of the systematic errors. The basic formulae for Q^2 and y for the E method are:

$$y_e = 1 - \frac{E_e'}{E_e}\sin^2\frac{\theta_e}{2}, \qquad Q_e^2 = 4E_e'E_e\cos^2\frac{\theta_e}{2}, = \frac{E_e'^2\sin^2\theta_e}{1 - y_e} \qquad (7.1)$$

where E_e' and θ_e are the energy and polar angle of the scattered electron. The polar angle θ_e is defined with respect to the proton beam or z direction, termed "forward" region. The formulae for the Σ method are

$$y_\Sigma = \frac{\Sigma}{\Sigma + E_e'(1 - \cos\theta_e)}, \qquad Q_\Sigma^2 = \frac{E_e'^2\sin^2\theta_e}{1 - y_\Sigma} \qquad (7.2)$$

with

$$\Sigma = \sum_h (E_h - p_{z,h}). \qquad (7.3)$$

Here E_h and $p_{z,h}$ are the energy and longitudinal momentum component of a particle h, the summation is over all hadronic final state particles and the masses are neglected. The denominator of y_Σ is equal to $2E_e$ but measured with all secondary particles. Thus

$$y_\Sigma = \frac{y_h}{1 + y_h - y_e} \qquad (7.4)$$

with the standard definition

$$y_h = \frac{\Sigma}{2E_e}. \qquad (7.5)$$

The variable x is calculated as $x = Q^2/ys$.

7.2   Monte Carlo Simulation

In the 1994 data analysis more than one million Monte Carlo DIS events were generated using the DJANGO [94] program. Whilst the 1994 Monte Carlo event statistics correspond to an integrated luminosity of approximately 18 pb^{-1}, the 1995 Monte Carlo DIS events corresponding to twice the luminosity of the data.

The DJANGO program is based on HERACLES [95] for the electroweak interaction and on the LEPTO program [96] to simulate the hadronic final state. HERACLES includes first order radiative corrections, the simulation of real bremsstrahlung photons and the longitudinal structure function. The acceptance corrections were performed using the GRV parametrization [106] which describes rather well the HERA F_2 results based on the 1993 data. LEPTO uses the colour dipole model (CDM) as implemented in ARIADNE [97] which is in good agreement with data on the energy flow and other characteristics of the final state as measured by H1 [98] and ZEUS [99]. Alternatively, first order QCD matrix elements with additional parton showers can be used for the final state QCD radiation. Hadronization is performed using string fragmentation [100]. This model does not contain events with large rapidity gaps [101], interpreted as diffractive events. Such events can be generated with the Monte Carlo programs RAPGAP [102] and DIFFVM [103]. The latter generates the diffractive exclusive channels $ep \rightarrow ep\rho^0$ and $ep \rightarrow ep\phi$. In the present analysis these channels to a large extent escape selection. Dedicated measurements of vector meson production cross sections have been made at HERA [104, 105], and are used to normalize the Monte Carlo prediction. The program RAPGAP generates events with a continuous mass spectrum of diffractive final states and the yield has been normalized to the rate of events with a large rapidity gap observed in the data. For the determination of systematic errors connected with the topology of the hadronic final state, the HERWIG model [79] was used. In the 1995 the acceptance corrections were performed using in turn the GRV [106] and MRSD0' [108] parton distributions for the initial structure functions in the Monte Carlo calculations. An iterative procedure was used to re-weight the input

structure functions of the Monte Carlo programs with the measured F_2 values in this analysis, as described in Sec. 7.4

Photo-production background was simulated using the PHOJET [109], PYTHIA [80] and RAYVDM [81] generators for γp interactions. With these models large samples of photo-production events were generated which contained all classes of events (elastic, soft hadronic collisions, hard scattering processes and heavy flavor production).

For the events generated with the models described above the detector response was simulated in detail [12] using a program based on GEANT [110]. The simulated Monte Carlo events were subjected to the same reconstruction and analysis chain as the real data.

7.3   Data Samples and Event Selection

7.3.1   Selection of Deep-Inelastic Scattering Events in 1994

Several data samples have been analyzed in order to cover maximally the kinematic plane. The distribution of the events is shown in Fig. 7.1.

The majority of the events are produced with the interaction vertex centered around zero in z, called the "nominal vertex" sample (shown as regions C and D in Fig. 7.1). Throughout this paper, the low (high) Q^2 sample refers to events in which the scattered electron has been detected in the BEMC (LAr calorimeter). To reduce the systematic errors of the F_2 measurement, a strict data selection was performed based on the behavior of the main detector components. This behavior was required to be optimal for the low Q^2 analysis of the nominal vertex sample which allows the highest precision to be reached. The remaining integrated luminosity for the low Q^2 sample is 2.2 pb^{-1}, the one for the high Q^2 sample is 2.7 pb^{-1}. The number of accepted events per unit luminosity was checked to be constant within statistical errors during the data taking period.

In order to study the behavior of F_2 at small Q^2 several means were used to extend the acceptance to this kinematic region using special event samples. For DIS events at very low Q^2 the electron is scattered through a large angle θ_e. For θ_e values greater than 173° and the interaction vertex at its nominal position at $z = +3$ cm the electron hits the inner edge of the BEMC calorimeter or remains undetected near the beam pipe. The acceptance extension in the backward region was realized as follows:

- During good accelerator background conditions, the innermost parts of the backward electromagnetic calorimeter (BEMC) around the beam pipe were included in the trigger for part of the time. Since these detector elements are of triangular shape, these data will be referred to as the "open triangle" data sample. An integrated luminosity of 0.27 pb^{-1} was accumulated. The kinematic region covered by this sample is shown as region (B) in Fig. 7.1.

- As in 1993 [77], the interaction point was shifted in the forward direction to an average position of $z = +67$ cm which permits measurements up to $\theta_e \simeq 176.5°$. This sample of 58 nb^{-1} of data is referred to as the "shifted vertex" data sample to distinguish it from the data with a nominal event vertex. It covers region (A) in Fig. 7.1.
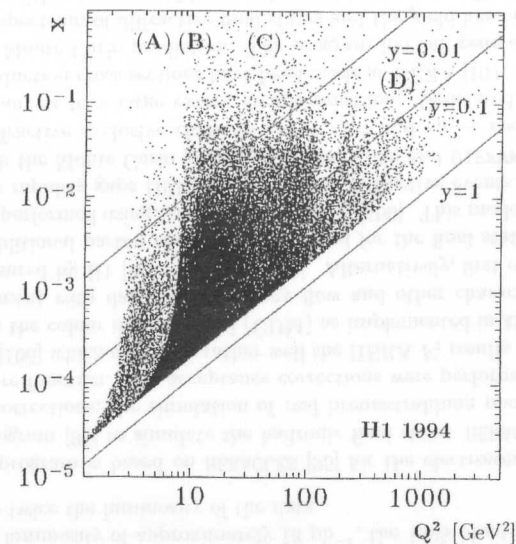
Fig. 7.1: Distribution of the event sample in the (x, Q^2) plane. The 4 visible regions (A, B, C, D) correspond to A) events recorded during a period in which the interaction region was shifted with respect to the nominal position allowing access to larger θ_e; B) events from the nominal vertex position taken in a period in which the innermost BEMC stacks of triangular shape were included in the trigger ("opened triangles", see text) or C) not included; D) high Q^2 events with the scattered electron detected in the LAr calorimeter.

- The low Q^2 region was also accessed by analyzing events from the so-called early proton satellite bunch colliding with an electron bunch at $z \simeq +68$ cm. The kinematic region covered by this sample is similar to that of the shifted vertex data sample. The "satellite" data sample amounts to $\simeq 3\%$ of the total data corresponding to a total "luminosity" of 68 nb^{-1} selected over the whole run period.

- Finally, a sample of deep-inelastic radiative events was extracted with a hard photon emitted collinear with the incident electron. These events have a reduced incident electron beam energy which allows access to very low Q^2 values with the present detector set-up. Since only about 2% of the DIS events are tagged as radiative events, the nominal vertex sample had to be used for this study. Subsequently the tagged radiative events are referred to as "the radiative event sample" and the bulk of the data are sometimes called "non-radiative" in contrast.

The low Q^2 DIS events in the backward region were triggered by an energy cluster in the BEMC ($E'_e > 4$ GeV) which was not vetoed by the ToF. The high Q^2 events were triggered by requiring an electromagnetic energy cluster in the LAr calorimeter ($E'_e > 8$ GeV). A trigger of lower energy threshold ($E'_e > 6$ GeV) also accepted the event if there was simultaneously a tracking trigger. In the region of the final F_2 data presented below

the trigger efficiency, which has been determined from the data, is about 80% for $E'_e \sim 8$ GeV, and becomes larger than 99% for $E'_e > 10$ GeV.

Deep-inelastic scattering events in H1 are identified by the detection of the scattered electron in the BEMC or LAr calorimeter and the presence of a reconstructed interaction vertex. The electron identification cuts, fiducial volume and vertex requirement are detailed in Tab. 7.1.

These selection criteria follow closely those of the 1993 data analysis [77]. For the low Q^2 nominal vertex sample ($Q^2 \leq 120$ GeV^2) an additional cut $r_{BPC} < 64$ cm is applied, where r_{BPC} is the radial distance of the electron hit in the BPC to the beam axis. This cut prevents the electron from entering the transition region between the BEMC and the LAr calorimeter where the energy corrections are large and depend strongly on the impact point. For the same reason, the high Q^2 events ($Q^2 > 120$ GeV^2) are accepted only if the electron cluster is fully contained in the LAr calorimeter. Despite these conditions, the measurement could also be performed for intermediate Q^2 ($Q^2 \sim 120$ GeV^2) due to the ± 30 cm spread of the event vertex position around its nominal position.

The scattered electron is identified with the electromagnetic cluster of maximum energy which satisfies the estimator cuts of Tab 7.1. The electron identification efficiency, determined from Monte Carlo simulation studies, is better than 97% except at $Q^2 \leq 6.5$ GeV^2 where it falls to 94% at the lowest x values.

	low Q^2 (shifted vtx)	low Q^2 (nominal vtx)	high Q^2	
	E, Σ method	E, Σ method	E method	Σ method
$\theta_e/°$	≤ 176	< 173	< 150	≤ 153
E'_e/GeV	> 11	> 11	> 11	> 11
z_{vertex}/cm	67 ± 30	5 ± 30	5 ± 30	5 ± 30
electron iden.	$\epsilon_1 < 5$ cm	$\epsilon_1 < 5$ cm	$\epsilon_3 > 50\%$	$\epsilon_3 > 65\%$
electron iden.	$\epsilon_2 < 5$ cm	$\epsilon_2 < 5$ cm	$\epsilon_4 > 3\%$	$\epsilon_5 < 30$ mrad

Tab. 7.1: Summary of event selection criteria for the shifted and the nominal vertex (vtx) data at low and high Q^2. The approximate event numbers are 10000, 220000 and 9000 events respectively. For the open triangle data sample the θ_e cut is 174°. For the electron identification several estimators were used: ϵ_1: electron cluster radius; ϵ_2: smallest distance from the closest hit in the BPC to the centroid of the electron cluster; ϵ_3: fraction of the electron energy deposited in the 4 most energetic cells of the cluster; ϵ_4: fraction of the electron energy deposited in the first 3 radiation lengths of the calorimeter; ϵ_5: angle between the line connecting the vertex to the centroid of the electron cluster and the associated track.

At low Q^2 the main sources of non-ep background are due to proton beam interactions with residual gas and beam line elements upstream of the H1 detector. At high Q^2 the main background is due to cosmic ray events and muons traveling off axis parallel to the proton beam. An efficient reduction of these background contributions is provided by the minimum energy and the vertex requirements discussed above. The number of residual beam-induced background events was estimated from non-colliding bunch studies, and the number of cosmic events from scanning. Both together represent less than 1% of the number of selected events in any (x, Q^2) bin.

The only significant background to DIS from ep interactions is due to photo-production events where the scattered electron escapes the detector along the beam pipe but in which an energy cluster from the hadronic final state fakes a scattered electron. About 10% of these events are identified as photo-production background if the scattered electron is found in the electron tagger. Photo-production events were simulated to estimate this background. The photo-production background was subtracted statistically bin by bin. Only 12 bins, out of a total of 193 (x, Q^2) bins, have a contamination larger than 3%. This contamination never exceeds 15% in any bin.

7.3.2   Selection of Deep-Inelastic Radiative Events in 1994

A sample of deep-inelastic events with an energetic photon ($E_\gamma > 4$ GeV) emitted collinear with the incident electron was selected. These radiative events can be interpreted as deep-inelastic scattering events with a reduced ("true") incident energy $E_t = E_e - E_\gamma$ which can be reconstructed due to the additional detection of the radiated photon in the small angle photon detector of the luminosity system. When using the E method, the Q_t^2 obtained by replacing in Eq. (7.1) the nominal beam energy by the reduced energy E_t. Note that Q_Σ^2 and y_Σ are unchanged by the $E_e \rightarrow E_t$ transformation while x_Σ is affected.

A first experimental study of this process at HERA has been published [35, 82] by the H1 collaboration using 1993 data, which where however too limited in statistics for a quantitative study of the proton structure. The larger integrated luminosity of the 1994 data permits a significant F_2 measurement for Q^2 values down to 1.5 GeV^2.

A summary of the selection criteria of the final sample of about 8200 events is given in Tab. 7.2 [83]. The event selection for radiative events is similar to the one for low Q^2 non-radiative events, apart from the additional requirement of a detected photon with at least 4 GeV in the small angle photon detector of the luminosity system. The minimum scattered electron energy is lowered to 8 GeV.

The selected sample contains both radiative DIS events and pile–up events due to overlaps of DIS and γp events with Bethe–Heitler (BH) events in a time window of ± 5 ns. The pile-up events are partly removed from the sample by requiring the energy in the electron tagger, E_{etag}, to be less than 2 GeV, but the majority of them remains. The background can be controlled through the redundancy of the true electron beam energy measurement E_t. For radiative DIS events we expect measurements of the quantity

$$\Delta \equiv [E_\gamma - E_e(y_e - y_h)]/E_\gamma \qquad (7.6)$$

to be concentrated around zero while for pile-up DIS events a concentration around one is expected. Here y_e and y_h are calculated according to Eq. (7.1) and (7.5). The distribution of Δ is shown in Fig. 7.2 for a sample of events with a) $E_{etag} > 2$ GeV (dominantly ep collisions with BH overlap events) and b) $E_{etag} < 2$ GeV. The data are compared with Monte Carlo simulation. The pile-up sample in Fig. 7.2a shows a clear peak for $\Delta = 1$, and is well described by the sum of simulated DIS and γp distributions with overlap of BH events. Fig. 7.2b shows a peak for $\Delta = 1$ from residual pile-up events for which the electron from the BH event was not detected, and a peak around $\Delta = 0$ from genuine radiative events. Radiative events are selected in this analysis by requiring $\Delta < 0.5$.
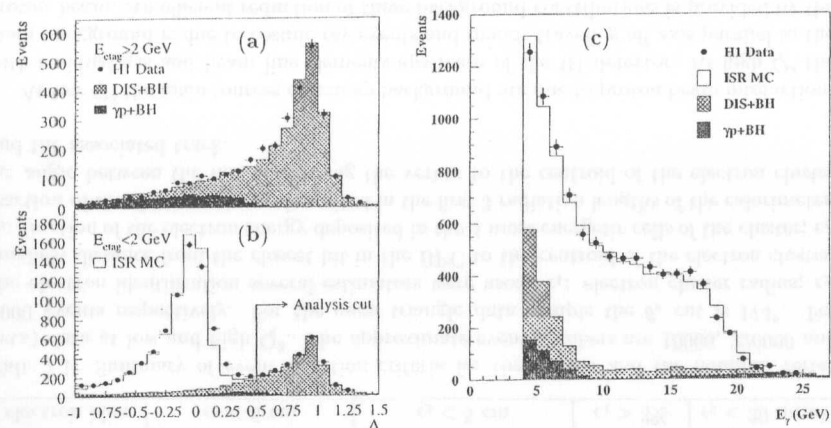
Fig. 7.2: Radiative events: experimental and Monte Carlo distributions of Δ (eq. 6) with a) the energy detected in the electron tagger (E_{etag}) bigger than 2 GeV; b) with $E_{etag} <$ 2 GeV and c) distribution of the photon energy detected in the photon tagger. The analysis cut in b) indicates the region of $\Delta > 0.5$ excluded from the analysis. The full solid line in b) and c) represents the sum of all three contributions in the Monte Carlo: DIS initial state radiation events (ISR MC), DIS events with a BH overlap (DIS + BH) and photo-production events with a BH overlap (γp + BH).

The background of pile-up events as estimated by the Monte Carlo simulation studies is subtracted statistically. The remaining background from overlap γp and DIS events estimated from Monte Carlo studies amounts to 8%, with at most 15% in an x, Q^2 bin. In Fig. 7.2c the photon energy spectrum as measured in the photon detector is shown for the selected sample and compared with simulated signal and background distributions. There is a good agreement between data and Monte Carlo simulation.

	low Q^2 (radiative events)
	E, Σ method
$\theta_e/^\circ$	≤ 174
E'_e/GeV	> 8
z_{vertex}/cm	5 ± 35
electron iden.	$\epsilon_1 < 5$ cm
electron iden.	$\epsilon_2 < 4$ cm
E_γ/GeV	> 4
E_{etag}/GeV	< 2
Δ	< 0.5

Tab. 7.2: Summary of event selection criteria for the radiative event sample. For the electron identification two estimators were used: ϵ_1: electron cluster radius and ϵ_2: smallest distance from the closest track to the centroid of the electron cluster. The variable Δ is defined in Eq. (7.6).

7.3.3 Selection of low-Q^2 DIS Events in 1995 Data Sample

The data sample used for this analysis corresponds to an integrated luminosity of 114 nb^{-1}. The trigger used requires that there be a local energy deposit (cluster) in the SPACAL calorimeter with energy greater than about 5 GeV occurring in time with an ep bunch crossing. The trigger efficiency is about 99% for electrons with an energy above 7 GeV. Losses of about 1% occur due to the event timing requirements.

Deep-inelastic scattering events in the H1 are identified by the detection of the scattered electron in the SPACAL or LAr calorimeter and the presence of a reconstructed interaction vertex. The electron identification cuts, selection requirements are detailed in Tab. 7.3.

	low Q^2 (shifted vtx)
	E, Σ method
electron iden.	$\epsilon_3 < 8.7$ cm
$\theta_e/^\circ$	≤ 178
E'_e/GeV	> 7
z_{vertex}/cm	$+70\pm 30$
electron iden.	$\epsilon_1 < 3.5$ cm
electron iden.	$\epsilon_2 < 10$ ns
electron iden.	$\epsilon_4 < 2$ cm
electron iden.	$\epsilon_5 < 2.5$ cm
electron iden.	$\epsilon_6 < 0.5$ GeV
E_{veto}/GeV	< 1
$\Sigma(E_h - P_{z,h})$ [1]	< 35 GeV

Tab. 7.3: Summary of event selection criteria for the radiative event sample. For the electron identification several estimators were used: ϵ_1: electron cluster radius and ϵ_2: the most energetic cluster in the electromagnetic section of the SPACAL is an electron candidate (see below) with a signal within a time window of 10 ns total width around the expected value for a genuine ep collision; ϵ_4: the required track segment in the BDC matched to the cluster in the SPACAL along the radial distance, ϵ_5: the required track segment in the BDC matched to the cluster in the SPACAL along the radial distance, ϵ_3: the radial distance from the beam line to the point at which the track associated with the cluster intersects the surface of the SPACAL ϵ_6: the energy measured behind the electron cluster in the hadronic part of the SPACAL with the a radius of 17.5 cm of the projected electromagnetic shower center.

The selection cuts were designed to have a high efficiency for detecting DIS events. For a large part of the kinematic region studied the total efficiency is better than 90%.

An efficient reduction of the main non-ep backgrounds, see Sec. 7.3.1, is provided by the minimum electron energy and the vertex requirements discussed above. The residual non-ep background was estimated by visual inspection to be less than 2% of the total number

---

[1] Only for the electron method $\Sigma(E_h - P_{z,h})$ is required to be larger than 35 GeV, where E_h and $P_{z,h}$ are the energy and longitudinal momentum of a hadron. The sum is over all energy deposits measured with the calorimeters.
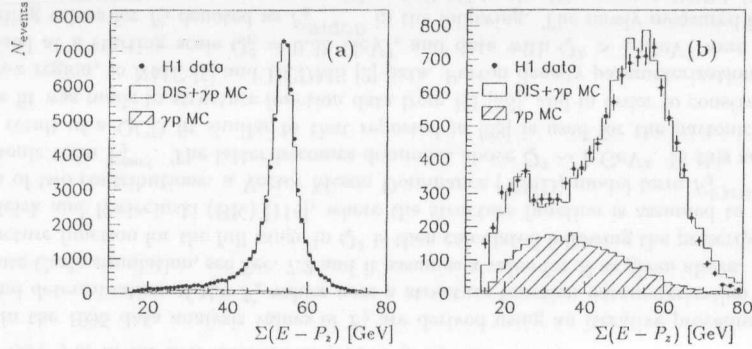
Fig. 7.3: Experimental (points) and Monte Carlo (solid histograms) distributions of $\Sigma(E_i - P_{z,i})$ measured in the calorimeter for a) all DIS event candidates and b) DIS event candidates with $y_e > 0.55$. The Monte Carlo curves are the sum of DIS and photo-production events and the photo-production events alone.

of events at the highest y, and negligible elsewhere. Similarly to the 1994 treatment of the background photo-production events, see Sec. 7.3.1, their amount was estimated from studies using simulated events from the Monte Carlo program PHOJET. The prediction for the remaining photo-production background was subtracted statistically bin by bin. For each Q^2 value, only the lowest x bin has a contamination larger than 5%. This contamination never exceeds 20%.

The energy scale for electrons has been determined with events at low y, for which the energy of the scattered electron is very close to the incident electron energy. The linearity of the energy response was verified with QED Compton events for the energy range used in this analysis. The precision of the angular measurement from the BDC was estimated using tracks in the central tracker extrapolated into the BDC region. Good agreement is observed between data and Monte Carlo calculation which is re-weighted as described in Sec. 7.4, and normalized to the luminosity.

Fig. 7.3 shows the distribution of $\Sigma(E_h - P_{z,h})$ for the full data sample and for the sample with $y > 0.55$. The Monte Carlo calculation describes the data well. The enhancement observed around 25 GeV in Fig. 7.3b results from events with one or more photons colinearly emitted by the incident electron.

In all, the detector response is well understood, allowing a precise extraction of the cross section and F_2.

7.4 Structure Function Measurement

7.4.1 Structure Function and Cross Section Measurement

The measured ep cross section in the HERA kinematic range can be expressed in terms of proton structure functions or cross sections for virtual photon-proton interactions as

follows

$$\frac{d^2\sigma}{dx dQ^2} = \frac{2\pi\alpha^2}{Q^4 x}\left(2 - 2y + \frac{y^2}{1+R}\right)F_2(x, Q^2)$$
$$= \Gamma[\sigma_T(x, Q^2) + \epsilon(y)\sigma_L(x, Q^2)] \equiv \Gamma\sigma_{\gamma^*p}^{eff}(x, y, Q^2). \tag{7.7}$$

Here $R = F_L/(F_2 - F_L)$, where F_L is the longitudinal structure function, α is the fine structure constant, and σ_L and σ_T are the cross sections for transverse and longitudinally polarized virtual photons, respectively. The flux factor, Γ, and the ratio of the longitudinal to the transverse flux, ϵ, are taken to be

$$\Gamma = \frac{\alpha(2 - 2y + y^2)}{2\pi Q^2 x}, \quad \epsilon(y) = \frac{2(1-y)}{2 - 2y + y^2}. \tag{7.8}$$

The quantity $\sigma_{\gamma^*p}^{eff}$ is the effective measured virtual photon-proton cross section for ep collisions in our kinematic range, and can be determined from the data without assumptions for R. The total virtual photon-proton cross section is defined[2] here as

$$\sigma_{\gamma^*p}^{tot} = \sigma_T(x, Q^2) + \sigma_L(x, Q^2) \simeq \frac{4\pi^2\alpha}{Q^2}F_2(x, Q^2). \tag{7.9}$$

With this definition $\sigma_{\gamma^*p}^{tot}$ depends only on Q^2 and x (or W) and the results of different experiments may easily be compared.

The virtual photon-proton cross section is determined by converting the measured number of events in a given bin into a bin averaged cross section using Monte Carlo acceptance calculations.

Compared to the previous H1 analysis [77] in the 1994 the F_2 measurement has been extended to lower and higher Q^2 (from $4.5 - 1600$ GeV^2 to $1.5 - 5000$ GeV^2), and to lower and higher x (from $1.8 \cdot 10^{-4} \leq x \leq 0.13$ to $3 \cdot 10^{-5} \leq x \leq 0.32$). The binning in x was governed by the detector resolution and could be chosen to be rather fine since the electron and Σ methods were used in the optimum range at low and high x, respectively. The x resolution is better than 20%. The Q^2 resolution is about 5% and the number of bins in Q^2 was adapted to statistics. All detector efficiencies were determined from the data utilizing the redundancy of the apparatus. Apart from very small extra corrections, all efficiencies were correctly reproduced by the Monte Carlo simulation. The bin averaged cross section was corrected for higher order QED radiative contributions using the program HECTOR [115]. Effects due to Z boson exchange at present values of Q^2 and y are smaller than 3% and were treated as part of the radiative corrections.

In the 1995 the data are binned in a grid of Q^2 and x for the region $Q^2 > 0.75$ GeV^2 as for previous H1 analyses, and a grid of Q^2 and y for the region below 0.75 GeV^2, which optimizes the access to the smallest possible (Q^2, x) values. Bin widths are chosen such that the number of events reconstructed in any given bin which originate from that bin is larger than 40% for the electron method and larger than 30% for the Σ method. All detector efficiencies are determined from the data utilizing the redundancy of the apparatus. Apart from small extra corrections, all efficiencies are correctly reproduced by

---

[2]The exact formula is $\sigma_{\gamma^*p}^{tot} = (4\pi^2\alpha/Q^4)(4M^2x^2 + Q^2)/(1-x) \cdot F_2(x, Q^2)$ [111, 112], which is approximately equal to (7.9) in the HERA kinematic range; M is the proton mass.

the Monte Carlo simulation, and therefore the Monte Carlo can safely be used to correct for acceptance and efficiency effects. The bin averaged cross section is corrected for first order QED radiative contributions with the program HERACLES. The effective virtual photon-proton cross section, $\sigma_{\gamma^* p}^{eff}$, is finally obtained by correcting the bin averaged cross sections for each bin to the values at the given bin centers.

In the 1994 analyses the structure function ratio $R = F_2/2xF_1 - 1$ was calculated using the QCD relation [85] with the NLO strong coupling constant [86] and the GRV structure function parametrization. Note that a 20% error on R corresponds to about 2% uncertainty on F_2 at $y = 0.6$ for R of about 0.6; no extra effect of the R uncertainty on F_2 was considered.

In 1995 analysis the model of [113] is applied for the calculation of R. These values of R are then used to determine the F_2 values, as well as to re-weight Monte Carlo events. The model is based on the photon-gluon fusion process and has the proper limit for $Q^2 \rightarrow 0$ GeV^2, where F_L should vanish $\propto Q^4$. The predictions of this model for the values of R in our kinematic region vary from 0.1 at $Q^2 = 0.35$ GeV^2 to 0.3 at $Q^2 = 3.5$ GeV^2. The predictions for R at higher Q^2 are in agreement with measurements from fixed target experiments. It should be noted that this is a model and future measurements could reveal quite different R values. However, only the lowest x point at each Q^2 is affected significantly by the assumption made for R. If R is taken to be zero rather than the values obtained using the above model, the variation in F_2 is 5 to 10% at the highest y (smallest x) at a given Q^2, and smaller elsewhere.

In the 1994 there were different data sets available which, for a given (Q^2, x) interval, did use different parts of the detectors. Thus many cross checks could have been made in kinematic regions of overlap for the two kinematic reconstruction methods and these gave very satisfactory results. In this analysis the results were obtained from the radiative F_2 analysis ($1.5 \leq Q^2 \leq 3.5$ GeV^2), from the shifted vertex analysis ($1.5 \leq Q^2 \leq 2.5$ GeV^2), from a combination of the shifted vertex and the satellite bunch analysis ($3.5 \leq Q^2 \leq 6.5$ GeV^2), from the open triangle analysis ($Q^2 = 8.5$ GeV^2) and from the nominal high statistics sample when the scattered electron is detected in the BEMC ($12 \leq Q^2 \leq 120$ GeV^2) or in the LAr calorimeter ($120 < Q^2 \leq 5000$ GeV^2).

In the 1995 data analysis values of F_2 are derived using an iterative procedure. An initial determination of the F_2 values uses a structure function parameterization in the Monte Carlo simulation, see Sec. 7.2 and it assumes a value for R as given above. A new structure function for the full range in Q^2 is then calculated following the prescription of Badelek and Kwiecinski (BK) [114], where the structure function is assumed to be the sum of two contributions: a Vector Meson Dominance (VMD) model term F_2^{VMD} and a partonic term F_2^{part}. The latter becomes dominant above $Q^2 \sim 1$ GeV^2. In this analysis the result of a QCD fit similar to that reported in [88] is used for the partonic term. This fit was made to structure function data from H1 [88], and in order to constrain the high-x region, to NMC [5] and BCDMS [2] data. Parton density parameterizations were defined at a starting scale $Q_0^2 = 0.35$ GeV^2, and data with $Q^2 > 1$ GeV^2 were fitted, yielding values for F_2 denoted as F_2^{H1QCD} in the following. The newly measured low Q^2 data points and the measurements at $Q^2 = 0$ GeV^2 in the W range at HERA [92, 93] were fitted to the form

$$F_2(x, Q^2) = C_{VM} F_2^{VMD}(x, Q^2) + \frac{Q^2}{Q^2 + Q_{VM}^2} F_2^{H1QCD}(\bar{x}, Q^2 + Q_{VM}^2), \quad (7.10)$$

with $\bar{x} = (Q^2 + Q_{VM}^2)/(W^2 + Q^2 + Q_{VM}^2)$. The fit parameters are the meson mass cutoff parameter Q_{VM}^2 and the normalization of the vector meson term C_{VM}. The latter parameter is not part of the BK model and was introduced to reproduce the real photoproduction data measured at HERA in a phenomenological way. Values of $Q_{VM}^2 = 0.45$ GeV^2 and $C_{VM} = 0.77$ are obtained[3]. It was checked that no further iteration step was needed. The Monte Carlo curves are re-weighted with these F_2 values (and the R values discussed above).

7.4.2 Sources of Systematic Errors

A list of sources of systematic errors in the 1994 F_2 determination is given below.

- The uncertainty in the electron energy scale which is 1% in the BEMC, and 3% in the LAr calorimeter. Since the y_e resolution varies as $1/y$ with the energy resolution even a 1% error on $\delta E/E$ can lead to 10% errors on F_2 at low y in the E method.

- The uncertainty in the hadronic energy scale: the detailed study of y_h/y_e and of $p_{T,h}/p_{T,e}$ (p_T is the momentum transverse to the beam axis) allowed the assignment of a 4% error on the hadronic energy deposited in the LAr calorimeter, a 15% error on the same quantity in the BEMC, and a 3% error on the y_h fraction carried by the tracks. These errors take into account the intrinsic energy scale uncertainty of each detector and the uncertainty of the sharing of the total hadronic final state energy between these three sub-detectors. These numbers also include uncertainties due to the treatment of the electronic noise in the LAr calorimeter and the BEMC.

- An uncertainty of up to 1 mrad for the electron polar angle which leads to an error on F_2 of 8% at low Q^2.

- Apart from the electron identification, all efficiencies were determined from the data and compared with Monte Carlo simulation. The agreement between the experimental and the simulated values for the individual efficiencies was found to be better than 2%. An overall error of 2% was assigned due to the imperfect description of the various efficiencies. A larger error was added to account for the variation of the vertex reconstruction efficiency at large x (up to 8%) where jets get closer to the beam pipe in the forward direction, and at small x or large θ (up to 4%) where H1 had no further tracking device besides the BPC to monitor the vertex efficiency.

- Uncertainties in the hadronic corrections, the cross section extrapolation towards $Q^2 = 0$ GeV^2 and higher order corrections, which give an error of up to 2% in the radiative correction. The accuracy was cross checked by comparing the HECTOR calculation with the HERACLES Monte Carlo simulation results. The agreement to the few percent level between the structure function results obtained with the electron and the Σ methods is an additional cross check for the control of the radiative corrections.

---

[3]Note that this procedure does not guarantee a consistent separation of F_2 into the F_2^{VMD} and F_2^{part} contributions, as prescribed by the model.

- The structure function dependence of the acceptance which was kept below 1% by performing a two step iterative analysis. The uncertainty in the simulation of the hadronic final state reflects most prominently in the efficiency for the requirement of an interaction vertex from tracks. A comparison of the different models (sect 4.3) for the hadronic final state was used to assign an additional 3% systematic error entering in all analyses at low x through the vertex efficiency.

- Based on the control data sample of electron tagged γp events the uncertainty due to photo-production background could be estimated to be smaller than 30% of the correction applied. This is equivalent to at most a 5% systematic error in the highest y bins at lower Q^2 only.

- Statistical errors in the Monte Carlo acceptance and efficiency calculations were computed and added quadratically to the systematic error.

- For the analysis of radiative events an additional 1.5% uncertainty on the photon energy measurement in the photon detector was considered and a 2% systematic error was added due to the uncertainty of the photon detector geometrical acceptance. An uncertainty on the trigger efficiency of 6% to 9% was included for the lowest x points.

A list of sources of systematic errors in the 1995 F_2 determination is given below.

- Uncertainty of the electron energy scale in the SPACAL, varying from 1% at large electron energies to 3% at 7 GeV.

- A 4% scale error for the hadronic energy in the LAr calorimeter, the effect of which is reduced due to the joint consideration of tracks and calorimeter cells for the Σ analysis. A 7% scale error was assigned to the energy of the hadronic final state measured in the SPACAL.

- A potential shift of up to 0.5 mrad for the electron polar angle.

- For the electron identification efficiency the error was taken to be 30% of the fraction of events lost by the cuts, as given by the DIS Monte Carlo.

- The following contributions to the systematic errors from the event selection were included: trigger and timing veto 0.5%; BDC efficiency 2%; vertex finding efficiency 2%. For the region $y < 0.05$ the systematic error on the vertex finding efficiency was increased to 5%.

- For the radiative corrections an error of 2% is taken everywhere, except for the highest y point of each Q^2 bin and for all points with $Q^2 \leq 0.65$ GeV^2, where it is increased to 5% for the electron method. This error is due to uncertainties in the hadronic corrections, in the cross section extrapolation towards $Q^2 = 0$ GeV^2, in the higher order corrections and the absence of soft photon exponentiation in the HERACLES Monte Carlo. These effects were studied using the program HECTOR [115].

- The uncertainty due to photo-production background was assumed to be 30% of the correction applied, i.e. smaller than 6%. This affects only the highest y bins at low Q^2.

- An additional error of 3% was assigned to the measurements using the Σ method to allow for the uncertainties in the hadronic final state simulation of the Monte Carlo programs. This error was determined by comparing the results of different reconstruction methods for the hadronic final state, using the combined information of calorimeter cells and tracks, or by using calorimeter cells only.

- The effect of reduced efficiency for detecting diffractive events, such as the exclusive channel $ep \rightarrow ep\rho^0$, has been estimated using the Monte Carlo programs for diffractive processes discussed in Sec. 7.2. Cross section corrections of up to 6% are applied for the points at the highest y values, and half of the correction was added to the systematic error. The effect is largest at the highest y values where the decay products of the meson often escape detection in the CJC and FT, and hence no event vertex is found.

- The overall normalization uncertainty is 3% due to the uncertainty in the luminosity determination.

These systematic uncertainties affect differently the F_2 measurements made with different methods. In both 1994 and 1995 analyses the comparison of the measurements made with the electron and with the Σ method has shown that the agreement between the two data sets is very good. For the final result the two measurements are combined [4] using the electron method for higher and the Σ method lower values of y.

The complete results of both 1994 and 1995 structure function measurements are published in [88, 89] in graphical and tabulated form. The effect of R is directly demonstrated as well as the the statistical, systematic and total errors and the value of R used for the F_2 calculation is presented. The measurements have a typical systematic error of 5–10%. Comparing the 1995 with the 1994 H1 analysis the F_2 measurement has been extended to lower Q^2 (from 1.5 GeV^2 to 0.35 GeV^2), and to lower x (from $3 \cdot 10^{-5}$ to $6 \cdot 10^{-6}$).

In Fig. 7.4 the 1995 F_2 data [89] are compared with previous H1 measurements [88], with the fixed target measurements of E665 [6] and NMC [5], and with the predictions of models for F_2 at low x. In the region of overlap the results are in good agreement with our previous measurements and the total error has been reduced by a factor of 2 to 3. The data also show a smooth continuation from the fixed target measurements towards the low-x region at HERA. The rise of F_2 with decreasing x is still clearly prominent for values of $Q^2 \geq 2$ GeV^2 but becomes less steep for smaller Q^2 values.

7.5   Discussion

7.5.1   Discussion of Results

A measurement has been presented of the proton structure function $F_2(x, Q^2)$ in deep-inelastic electron-proton scattering at HERA with data taken in the running period of 1994

---

[4]In 1995 the electron method is used except for the highest x point at $Q^2 = 1.5$ GeV^2. For this point the total error calculated with the Σ method is almost a factor of two better than that of the electron method, and therefore the Σ method is used.
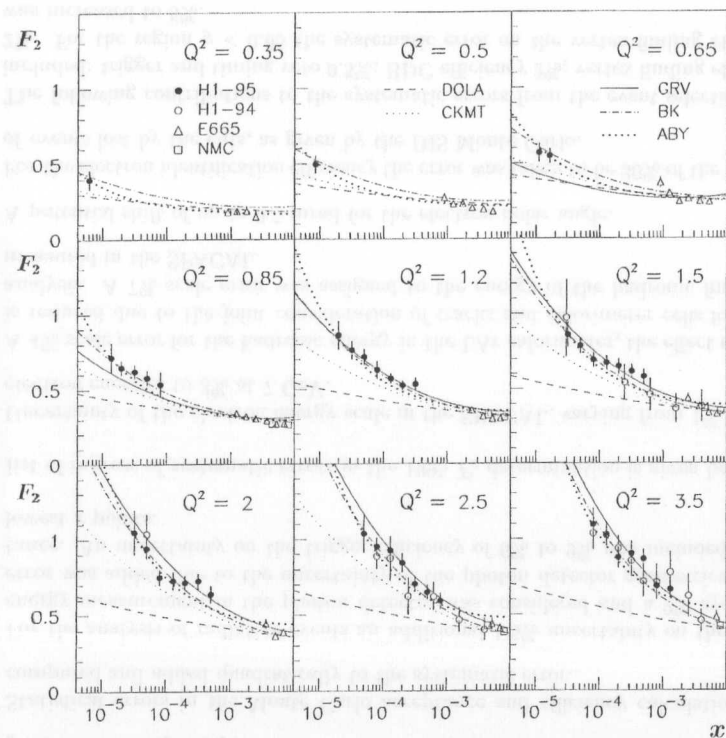
Fig. 7.4: Measurement of the proton structure function $F_2(x, Q^2)$ in the low Q^2 region by H1 (full points), together with previously published results from H1 (open circles), E665 (open triangles), NMC (open squares). The Q^2 values are given in GeV^2. Various predictions for F_2 are compared with the data: the model of Donnachie and Landshoff (dashed line), the model of Capella et al. (dotted line/small), the model of Badelek and Kwiecinski (dashed-dotted line), the model of Glück, Reya and Vogt (full line) and the model of Adel et al. (dotted line/large). Global normalization uncertainties are not included.

and 1995. The former profit on the integrated luminosity of 2.7 pb^{-1} which represents a tenfold increase in statistics compared to the F_2 analysis based on the 1993 data of the H1 experiment. The structure function measurement includes data from different detector components and running configurations. Low Q^2 values are reached using data with the ep interaction vertex shifted from the nominal position and with radiative events. The data cover a kinematic range for Q^2 between 1.5 and 5000 GeV^2 and x between $3.0 \cdot 10^{-5}$ and 0.32. The later are the first measurements made with the upgraded backward calorimeter and drift chamber of the H1 detector. The data cover the region of Q^2 between 0.35 GeV^2 and 3.5 GeV^2 and with Bjorken-x values down to $6 \cdot 10^{-6}$. The measurements presented are obtained using two different methods to reconstruct the inclusive scattering kinematics, allowing both a powerful internal cross check of the data and the measurement in a large kinematic region. A smooth transition is observed from the fixed target high-x data to the HERA low-x data. The distinct rise of the structure function with decreasing x in the low-x region, which is very prominent for $Q^2 \geq 2$ GeV^2, diminishes at lower Q^2 values. When taken together with the data from fixed target experiments, the rise observed for the smallest Q^2 values approaches that expected in Regge and VMD interpretations.

The data have been compared with different models which aim to describe the whole Q^2 region. Several of these models predict the correct qualitative behavior observed in the data but presently do not agree with the data throughout the full kinematic range. The data access the transition region from DIS to photo-production and provide powerful constraints on the development of further low-Q^2 phenomenology. Other fenomena such as phenomenological analysis of the F_2, comparison with the models at low Q^2, double asymptotic scaling, extraction of the gluon density as well as the more detail and complete presentation of the results, are presented in the [88].

7.5.2   Rôle of QED Compton Events Studies

Presently the systematic effects affecting the F_2 measurement are in the focus of the analyses, since statistical uncertainties become insignificant. On the other side it was shown throughout of here presented analysis that the QED Compton events provide an useful experimental tool for enhancing the knowledge of the backward scattering region. Therefore in this section the rôle of the QED Compton events studies is discussed in more details.

7.5.2.1   Energy Scale Studies

As it was shown in the above reviewed the F_2 analyses the following two methods are used in order to reconstruct the kinematics of the deep inelastic electron proton scattering: The electron method using only the information of the scattered electron and so-called "Σ" method calculating the kinematics based on both the scattered electron and the hadronic final state. Thus, the knowledge of scattered electron is crucial for the precise reconstruction of kinematical variables and consequently reducing the systematic errors of the F_2 measurement. In order to describe the kinematics of a scattered electron the two parameters are to be determined, its energy and the corresponding polar angle. In the kinematical regime characterized by the small values of $-Q^2$ (where Q^2 is the squared

momentum transfered) the electron is scattered into the backward scattering region of H1 detector. As it was shown in the previous chapter the experimental techniques based on the QED Compton events provide very useful tools to study this region.

In order to improve the measurement of **the energy of the scattered electron** the QED Compton method provided:

- The values of the overall calibration factors, which showed that e.g. the absolute energy scale of BEMC in 1994 was well understood, i.e. beyond 0.5% whilst in 1995 the absolute energy scale of SPACAL was undercalibrated by 2-3%.

- The only possible way of investigating the response linearity of the BEMC and SPACAL detectors in the H1 environment. These studies confirmed in 1994 the linearity of the BEMC energy scale to within 1% in the energy interval from 5 to 22 GeV, and in 1995 the linearity of the SPACAL energy scale to within 1% in the energy interval from 10 to 20 GeV. In addition in 1995 they indicated a non-linearity on the level of 3% and proved the undercalibration of the SPACAL energy scale by 2-3%.

- The first attempt to cross-check the energy resolution of the both BEMC and SPACAL detectors in the H1 environment. Despite the huge statistical errors it was shown that for the future measurements there is a way of extracting the resolution function of the in situ detector.

In the 1994 (1995) data taking **the polar angle of the scattered electron** was determined by means of the central and backward tracking detectors using the spatial coordinates of the interaction vertex and the reconstructed BPC point (BDC track) corresponding to the electromagnetic cluster in BEMC (SPACAL). In this procedure the relative position of the BPC-BEMC (BDC-SPACAL) versus the interaction vertex was crucial. Thus the studies of the relative position of the BEMC (SPACAL) versus the beam line and BPC (BDC) versus BEMC (SPACAL) using the samples of the QED Compton events were of the great importance. Although they took into the account only the relative shift of the corresponding detectors versus the beam line in the xy-plane, which were caused by a possible misplacement of the components during the setting up the whole H1 detector and the accelerator effects such as the various beam tilts in the different luminosity fills, they provided the corrections of the relative position of the backward calorimeter versus the beam line, see Eq. (6.20) and (6.42) and the corrections of the relative position of tracking detector and the corresponding calorimeter, see Eq. (6.22) and (6.43).

Although the BPC efficiency measurement was based on the strong assumption that the efficiency of the backward trackers BPC (BDC) was homogeneous over the whole $r\phi$-plane it was showed that the efficiency of the BPC (BDC) was high, i.e. $> 96\%$ ($> 97\%$) in 1994 (1995) data taking. The evaluation of the probability of γ-conversion and consequently, the estimation of dead material in front of BPC-BEMC (BDC-SPA-CAL) system is based on the samples of the QED Compton events indicated an increase of these parameters in the 1995 with respect to the 1994 data taking. It was caused by installing the new components during the 1994/95 winter shutdown. The comparison of the results of these studies performed using the experimental data and the Monte Carlo simulations are more important then the absolute results since they provide a test of

the description of the experimental environment in the Monte Carlo programs. It was shown that the amount of the dead material in front of the BPC-BEMC (BDC-SPACAL) system was underestimated in the Monte Carlo simulations in both the 1994 and 1995. In addition the inhomogeneous distribution of the dead material as a function of the azimuthal angle, ϕ, was observed in the 1995 experimental data in contrary to the Monte Carlo simulations.

Finally we would like to remind that all these methodological studies enhanced the knowledge of the backward scattering region of in a period when the H1 detector was largely upgraded.

7.5.2.2 Luminosity Determination

An important global systematic effect on the structure function is the precision of the luminosity measurement which e.g. resulted in the 1995 F_2 measurement in overall normalization uncertainty of 3%.

At present four different methods of luminosity measurement are employed in the H1 experiment, see Sec. 6.3. The most precise method of determining the luminosity from the reaction $ep \to ep\gamma$ is based on the measurement of the energy spectrum of hard photons. The main uncertainties of the measurement of the integrated luminosity e.g. for the 1994 "nominal vertex" data were: the photon detector absolute energy scale (0.9%), the trigger efficiency of the luminosity system (0.3%), the precision of the electron gas background subtraction (0.4%), the photon-tagger acceptance (0.5%), multiple photon overlaps (0.4%), the precision of integration resulting from the 10 sec interval between consecutive luminosity measurements (0.5%) and the correction for satellite bunches (0.5%), resulting in the total precision of the luminosity measurement of 1.5%. For the 1994 "shifted vertex" data sample the luminosity uncertainty was 3.9%.

As it was shown in Sec. 6.3.2.3, the main uncertainties of the measurement of the integrated luminosity using QED Compton method for the 1994 "nominal vertex" data were: the BEMC energy scale (0.8%), cluster radius determination (2.0%), its rather large read-out noise (2.3%), determination of the polar angle of the scattered electron and photon (2.0%), ToF timing (2.6%). Although the knowledge of newly installed detectors was not comparable with the former ones they already lower the systematic error of the luminosity measurement. The main uncertainties of the measurement of the integrated luminosity using QED Compton method for the 1995 "nominal vertex" data were, see Sec. 6.3.3: the SPACAL energy scale (1.3%), cluster radius determination (0.9%), SPACAL veto (3.2%), determination of the polar angle of the scattered electron and photon (1.1%). In addition the more precise determination of acoplanarity angle enabled tightening of the coplanarity restriction and thus to lower the Monte Carlo uncertainties.

Here it has to be stressed that here obtained results of the determination of the integrated luninosity using the QED Compton method, which were in agreement within one sigma of statistical errors with the values provided by other methods, confirmed the H1 luminosity measurement in the 1994 and 1995. Despite the fact that both the statistical and systematic errors of the values of integrated luminosity determined using QED Compton method the improtance of this kind of measurement is resided in its independence on the H1 luminosity system.

Chapter 8

Conclusion

A measurement has been presented of the total integrated luminosity using the samples of the QED Compton events recorded with the H1 detector in 1994 and 1995. The same data samples were employed in order to study the backward scattering region of the H1 experiment in terms of the absolute energy scale and the response linearity of the electromagnetic calorimeters, their relative positions to the beam line and the misalignment of the calorimeters and the corresponding tracking detectors. The BPC efficiency measurement, the evaluation of the probability of γ-conversion and consequently the estimation of the amount of the dead material in front of the BPC-BEMC and BDC-SPACAL system have been performed as well.

A survey of the definitions of the three classes of the hard photon radiation from the lepton line in the neutral current (NC) processes at HERA has been given. The exact analytic expressions of the QED Compton event cross section have been presented. The three separate contributions depending on the value of the invariant mass of the hadronic system have been reviewed. The definitions of the kinematical relations, which characterize the QED Compton events have been presented. The basic ideas and solutions which have been chosen in COMPTON, a Monte Carlo generator for QED Compton events, have been summarized together with the input values of the kinematical variables used in the production of the Monte Carlo simulation data used in here presented analysis. The various predictions of the distributions and correlations of the crucial kinematical variables for a sample of the QED Compton events generated using the COMPTON generator have been shown and discussed.

A brief description of the HERA accelerator and a review of the components of the H1 detector has been presented emphasizing the H1 backward scattering region, which was mainly relevant for the presented analysis.

The sensitivity of the BEMC photo-diode readout to the the passage of charged particles or photons through the depletion layer causes another type of background, known as nuclear counter effect, or "single diode events". The three main sources were identified being beam-gas and beam-wall interactions; direct and scattered synchrotron radiation; leaking showers particles originating from the interaction point. Since the proton induced background was effectively vetoed by the ToF system the further suppression of the fake triggers was based upon the lead shielding of the beam pipe in the BEMC region; identification of the SDE by the L1 trigger veto logic installed in the sixteen innermost BEMC

stacks; and their off-line flagging at the L4 trigger level of the H1 trigger system. The 40 % decrease of the trigger rate applying the SDE veto to the BSET stand-alone CL2 trigger element has been shown.

The experimental techniques used to select the QED Compton event samples in both 1994 and 1995 data taking have been described. Compared to [34] a new selection procedure has been designed in order to increase the efficiency of detecting of the QED Compton events. In both the 1994 and 1995 several samples of QED Compton events have been analyzed following the various configurations of HERA machine and H1 experiment.

The identification of a QED Compton candidate, which was based upon searching for two most energetic electromagnetic clusters with the back-to-back topology in the BEMC in 1994 and SPACAL in 1995 has been described. The QED Compton events were triggered by a signal of an electromagnetic cluster with energy well above the trigger threshold which was not vetoed by the timing requirements. The trigger efficiencies for BEMC (SPACAL) trigger elements and various combination of ToF trigger elements determined from the data have been presented.

The L5 classification routine EQEDC in 1994 and the 1995 event classification based on two different algorithms i.e. EQEDC and SQCFLA routines have been discussed. In order to reject as far as remaining background and consequently to obtain the clean samples of BEMC and SPACAL QED Compton events in 1994 and 1995 respectively, additional selection criteria had to be imposed. The positions of the analysis cuts in the corresponding distributions have been presented.

The various distributions of basic kinematical variables for data have been compared to the predictions of the COMPTON Monte Carlo. From here presented plots it has been concluded that the Monte Carlo distributions are in a good agreement with data within statistical errors. The reasons and consequences of the occasional discrepancies have been discussed.

Taking into account the simple final state of the QED Compton event kinematics the energy of the scattered electron and photon can be calculated from the two corresponding scattered polar angles. This redundancy provide the possibility to use the samples of the selected QED Compton events for calibration studies. For both BEMC and the SPACAL detectors the absolute energy scale and the response linearity have been studied. An attempt to determine the resolution of these two calorimeters in the H1 environment has been presented. It should be stressed that these calibration methods are Monte Carlo independent.

The description of the different methods used for luminosity measurement in the H1 experiment has been reviewed. The dominant contributions to the systematic error of the each method have been summarized. The samples of the QED Compton events have been analyzed in order to provide the measurements of the integrated luminosity for different run periods in 1994 and 1995 data taking. Comparing the results obtained using the QED Compton method it has been concluded, that (i) the values of integrated luminosity measured by means of the QED Compton method are in agreement within one sigma statistical error with values measured by means of the H1 luminosity system method and random coincidence method and thus confirm the luminosity measurement; (ii) the total error of the values of integrated luminosity determined by the QED Compton method

are larger compared to the for H1 luminosity system measurement, but comparable (even slightly smaller) with the ones obtained by the random coincidence method; (iii) the further decrease of both the statistical and the systematic errors of the integrated luminosity measurement using the QED Compton method is possible either by enlarging the amount of accumulated QED Compton events, which could be achieved by increasing the total amount of delivered luminosity by HERA machine in the H1 scattering region and/or by increasing the geometrical acceptance of the electromagnetic calorimeter covering the backward scattering region. The later was achieved by newly installed detectors in 1994/95 winter shutdown. In addition more sophisticated triggering e.g. such as using the components of the higher levels of H1 trigger system, can significantly change the signal to background ratio. Additionally, the improvement of the measurement of the scattered electron and photon in the H1 backward scattering region in terms of improved measurement of the cluster parameters and the more precise determination of the azimuthal angles of the scattered electron and photon for coplanarity determination can significantly decrease the systematic error.

A measurement of the proton structure function F_2 in 1994 and 1995 is reviewed in more detail and the rôle of QED Compton event analysis in such complex measurement has been discussed. The systematic effects affecting the F_2 measurement are in the focus of the analyses at H1 experiment, since statistical uncertainties become insignificant. The detailed calibration and technical studies using the QED Compton events presented here were aimed to improve our knowledge of the apparatus and thus to back the F_2 analysis and its results.

Finally, we would like to conclude that although this analysis has been primarily limited by the relatively small statistics available in the 1994 (due to small instantaneous luminosity) and 1995 (due to the trigger down-scaling and short period of data taking), it was demonstrated, that the study of QED Compton events provides useful experimental tools for enhancing the knowledge of the backward scattering region of the H1 detector and in addition enables an independent cross-check of the luminosity measurement. We believe, that future analyses of QED Compton events will benefit from increased statistics and thus will not only decrease the total errors of here presented results but will enable us to study the detector components in more details and to measure the luminosity in the significantly smaller run ranges.

Appendix A

Derivation of Generalized Helicity Formula for One-Photon-Exchange Processes

Considering a diagram of the type shown in Fig. A.1 one can write its differential cross section in the form:
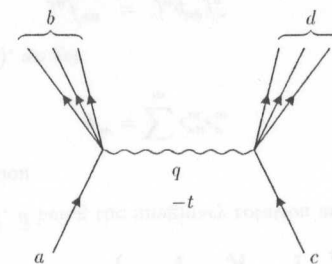
Fig. A.1: The diagram for the process $a + c \rightarrow b + d$ via one photon exchange.

$$d\sigma = \frac{1}{2\,\lambda^{1/2}(s,\,m^2,\,m'^2)}\,\frac{1}{t^2}\,|\mathcal{M}|^2\,\frac{d^4q}{(2\pi)^4}\,, \tag{A.1}$$

where s is the total energy squared in the center of mass frame, t is is the absolute value of the virtual photon's four-momentum squared, m, m' are the masses of the initial particles a and c, respectively and the kinematical function λ is defined by

$$\lambda = x^2 + y^2 + z^2 - 2xy - 2yz - 2zx\,, \tag{A.2}$$

and

$$|\mathcal{M}|^2 = I_{\mu\nu}I'^{*\mu\nu}\,, \tag{A.3}$$

$$I_{\mu\nu} = \frac{1}{n} \sum \int d\Gamma\, j_\mu j_\nu^*, \tag{A.4}$$

$$I'^{*\mu\nu} = \frac{1}{n'} \sum{}' \int d\Gamma'\, j'^\mu j'^{*\nu}, \tag{A.5}$$

where j_μ (j'_ν) is electromagnetic current at the left-hand (or right-hand) vertex, n (n') is the number of initial polarization states at left-hand (right-hand) vertex, $\sum$ ($\sum'$) means summing over all polarization states of initial and final particles at left-hand (right-hand) vertex, the Lorentz invariant space factors $d\Gamma$, $d\Gamma'$ are as follows:

$$d\Gamma = (2\pi)^4\, \delta^{(4)}(p_a - p_b - q)\, d\Gamma_b \tag{A.6}$$
$$d\Gamma' = (2\pi)^4\, \delta^{(4)}(p_c - p_d - q)\, d\Gamma_d \tag{A.7}$$

where $d\Gamma_b$ and $d\Gamma_d$ is the Lorentz invariant space factor for the initial (system b) and the final state (system d), respectively.

Using

$$d^4q = \frac{1}{4\,\lambda^{1/2}(s, m^2, m'^2)}\, dt\, dW^2\, dW'^2\, d\phi, \tag{A.8}$$

where W, W' are the invariant mass of the systems b and d, respectively, and ϕ is the virtual photon's azimuthal angle. Integration over the azimuthal angle ϕ leads to

$$\frac{d\sigma}{dt\, dW^2\, dW'^2} = \frac{1}{64\pi^3}\, \frac{1}{2\,\lambda^{1/2}(s, m^2, m'^2)}\, \frac{1}{t^2}\, |\mathcal{M}|^2. \tag{A.9}$$

Using the helicity treatment [57] the helicity structure of $|\mathcal{M}|^2$ is established as follows. First, the four-vectors of the vertex (p_a, p_b, q) $((p_d, p_c, q))$ form the so called "left-hand (right-hand) vertex plane" in four-space. Now a set of unit polarization four-vector $(\epsilon_\parallel, \epsilon_0, \epsilon_1, \epsilon_2)$, associated with the left-hand vertex and defined as follows in four-space: $\epsilon_\parallel$ is parallel to q, ϵ_0 belongs to the "left-hand vertex plane" and is orthogonal to $\epsilon_\parallel$, ϵ_2 is orthogonal to both planes (p_a, p_b, q), and (p_d, p_c, q), and finally, ϵ_1 is orthogonal to $\epsilon_\parallel$, ϵ_0 and ϵ_2. In addition, the following circular combinations of them

$$\epsilon_\pm = \mp \frac{(\epsilon_1 \pm i\epsilon_2)}{\sqrt{2}} \tag{A.10}$$

yield another set of polarization four-vectors, $(\epsilon_\parallel, \epsilon_0, \epsilon_+, \epsilon_-)$, which satisfied $\epsilon_m^* \epsilon_n = \pm\delta_{mn}$. The physical interpretation of these polarization vectors is that $(\epsilon_0, \epsilon_+, \epsilon_-)$, are associated respectively with helicity states[1] 0, +1, -1 of the virtual photon with respect to the left-hand vertex plane; $\epsilon_\parallel$ is eliminated by the request for gauge invariance. Analogicaly, for the right-hand vertex, we introduce a set of linear polarization vectors $(\epsilon'_\parallel, \epsilon'_0, \epsilon'_1, \epsilon'_2)$.

Notice, that directly from definition $\epsilon'_\parallel = \epsilon_\parallel$, and $\epsilon'_2 = \epsilon_2$. Repeating the previous algorithm we get another set $(\epsilon'_\parallel, \epsilon'_0, \epsilon'_+, \epsilon'_-)$.

---

[1] Helicity is here defined as the spin component in the vertex plane.

The two tetrads ϵ_m and $\epsilon'_{m'}$, $(m, m' = \parallel, 0, +, -)$ could be superposed to each other by means of a four-space rotation about the plane defined by $(\epsilon_\parallel, \epsilon_2)$. The corresponding rotation matrix is defined by

$$\epsilon_m = \sum_{m'} R_{m,m'} \epsilon_{m'} \tag{A.11}$$

and its expression is easily calculated or derivated from the Wigner rotation matrices, extrapolating them from real to complex rotation angles:

$$R_{m,m'} = \begin{pmatrix} 1 & 0 & 0 & 0 \\ 0 & \frac{1+x}{2} & -\frac{y}{\sqrt{2}} & \frac{1-x}{2} \\ 0 & \frac{y}{\sqrt{2}} & x & -\frac{y}{\sqrt{2}} \\ 0 & \frac{1-x}{2} & \frac{y}{\sqrt{2}} & \frac{1+x}{2} \end{pmatrix}, \tag{A.12}$$

where $x = \cos\bar\theta$, $y = \sin\bar\theta$, $\bar\theta$ being the imaginary rotation angle.

Using the closure relation

$$g^{\mu\nu} = \sum_m \epsilon_m^{*\mu} \epsilon_m^\nu \tag{A.13}$$

combining with Eq. (A.11), we get

$$\begin{aligned} j_\mu j'^{*\mu} &= j_\mu g^{\mu\rho} j'^*_\rho \\ &= \sum_{m,m'} j_m \Gamma_{m,m'} j'^*_m \end{aligned} \tag{A.14}$$

defining

$$j_m = j_\mu \epsilon_m^{*\mu}, \quad j'_m = j'_\rho \epsilon_m^{'*\rho}, \tag{A.15}$$

and we obtain

$$|\mathcal{M}|^2 = \sum_{m,m',n,n'} I_{m,n} R_{m,m'} R_{n,n'} I'^*_{m',n'} \tag{A.16}$$

defining

$$\begin{aligned} I_{m,n} &= I_{\mu\nu} \epsilon_m^\mu \epsilon_n^{*\nu} \\ &= \frac{1}{n} \sum \int d\Gamma\, j_m j_n^* \end{aligned} \tag{A.17}$$

$$\begin{aligned} I'_{m',n'} &= I'_{\mu\nu} \epsilon_{m'}^{'\mu} \epsilon_{n'}^{'*\nu} \\ &= \frac{1}{n} \sum \int d\Gamma'\, j'_{m'} j'^*_{n'} \end{aligned} \tag{A.18}$$

Notice, that in Eq. (A.14) and (A.16), only the values of m, m', n, $n' = +, 0, -$ are to be considered, since $j_\parallel = j'_\parallel = 0$ by the gauge invariance.

$$|\mathcal{M}|^2 = \sum_{m,m'} I_{m,m} (R_{m,m'})^2 I'^*_{m',m'} \tag{A.19}$$

Using parity conservation ($I_{++} = I_{--}$, $I'_{++} = I'_{--}$) one get for the cross section Eq. (A.9) the following expression [59]:

$$\frac{d\sigma}{dt\,dW^2\,dW'^2} = \frac{1}{64\pi^3}\frac{1}{2\,\lambda^{1/2}(s,\,m^2,\,m'^2)}\frac{1}{t^2}$$

$$\times\left[I_{++}I'_{++}(1+\cosh^2\phi)+(I_{++}I'_{00}+I_{00}I'_{++})\sinh^2\phi+I_{00}I'_{00}\cosh^2\phi\right] \qquad (A.20)$$

$$\cosh\theta = \frac{t\,(2s-t-\Sigma)-(W^2-m^2)(W'^2-m'^2)}{\lambda^{1/2}(W^2,\,m^2,\,-t^2)\,\lambda^{1/2}(W'^2,\,m'^2,\,-t'^2)}, \qquad (A.21)$$

where

$$\Sigma = m^2 + m'^2 + W^2 + W'^2. \qquad (A.22)$$

At the present stage the helicity method could be applied for our particular case of the Compton scattering $ep \to e\gamma + X$:

$$a \equiv e, \quad b \equiv (e-\gamma), \quad c \equiv p, \quad d \equiv X. \qquad (A.23)$$

For more detial technical derivation see the [60].

Appendix B

L4 Routine to flag BEMC Nuclear Counter Effect

In order to suppreess the fake triggers due to the nuclear counter effect, so-called BEMC single diode events (SDE), analyzed in Chapter 4, at the L4 trigger level of the H1 trigger system a flagging routine was used. In this appendix its FORTRAN source code is presented.

```
      subroutine bccosm (iflag)
*     stacks with only 3 wls - small triangles
      dimension ismtri(8)
      data ismtri / 2, 7, 20, 29, 70, 79, 92, 97 /
      save ismtri
*     limit for the maximum relative contribution from 1 diode
      parameter (ratlim = 0.95)
*keep,bcs.
      integer      nhrow,nhcol,nhlen
      parameter   (nhrow = 2, nhcol = 1, nhlen=2)
      integer      nbosiw
      parameter   (nbosiw=1000)
      integer      iw(nbosiw)
      real         rw(nbosiw)
      common /bcs/ iw
      equivalence (rw(1),iw(1))
      save   /bcs/
*keep,bosmdl.
c     ------bosmdl
      logical         begjob,endrun,begrun,revent,endjob,othdat
      common/bosmdl/begjob,endrun,begrun,revent,endjob,othdat,
     +              lccrun,nccrun,nevent,
     +              iha,ibs,idb,idatel,lup,isn,jsn
      save   /bosmdl/
```

```
c       ------
*kend.
        common /enbemc/ ebemc,nclus,eclus,ratmax
*keep,stfunct.
*       index of element before row number irow
        indr(ind,irow)=ind+2+iw(ind+1)*(irow-1)
*       index of l'th element  of row number irow
        indcr(ind,l,irow)=indr(ind,irow) + l
*       l'th integer element of the irow'th row of bank with index ind
        ibtab(ind,l,irow)=iw(indcr(ind,l,irow))
*       l'th real element of the irow'th row of bank with index ind
        rbtab(ind,l,irow)=rw(indcr(ind,l,irow))
*kend.
*       at first entry
        if (begrun) then
          call bhs(iha+34,1,100,0.0,99.)
          call stext(iha+34,4,'bemc:')
          call stext(iha+34,5,'stack number for cosmic-diode flag>.95')
          call bhs(iha+35,1,100,0.0,50.)
          call stext(iha+35,4,'bemc:')
          call stext(iha+35,5,'stack energy for cosmic-diode flag>.95')
        endif
*       event entry
        if (revent) then
          iflag  = 0
          ratmax = 0.0
*         link to the bemc diode and stack banks
          inbe0r = nlink('BEOR',0)
          inbenr = nlink('BENR',0)
          inbngr = nlink('BNGR',0)
          if (inbe0r.ne.0 .and. inbenr.ne.0 .and. inbngr.ne.0) then
            nrbe0r = iw(inbe0r+2)
            nrbenr = iw(inbenr+2)
            nrbngr = iw(inbngr+2)
*           find the hottest bemc stack
            estmax = 0.0
            nstmax = 0
            irowmx = 0
            do 10 irow = 1, nrbe0r
            esta   = rbtab(inbe0r,1,irow)
            if (esta .gt. estmax) then
              estmax = esta
              nstmax = ibtab(inbngr,1,irow)
              irowmx = irow
            endif
10          continue
*           hottest stack found
```

```
            if (irowmx .gt. 0) then
*             check if the stack is small triangle
              fact    = 0.25
              do 20 i = 1, 8
              if (nstmax .eq. ismtri(i)) fact = 0.33333
20            continue
*             determine the diode / stack energy ratio
              ratmax = 0.0
              do 30 i = 1, 4
              e = rbtab(inbenr,i,irowmx)
              if (e .eq. 0.) then
                ratio = 0.
              else
                ratio = (e * fact) / estmax
              endif
              if (ratio.gt.ratmax) ratmax = ratio
30            continue
*             fill the histos for the positive decision
              if (ratmax .gt. ratlim) then
                iflag = 1
                call shs(iha+34,1,float(nstmax))
                call shs(iha+35,1,estmax)
              endif
            endif
          endif
        endif
        return
        end
```

Bibliography

[1] B. H. Wiik, HERA status, Proceedings of the workshop "'Physics at HERA"', Vol.1, ed. W. Buchmüller and G. Ingelman, DESY, Hamburg, 1991

[2] BCDMS Collab., A. C. Benvenuti et al., Phys. Lett. **B223** (1989) 485; CERN preprint CERN-EP/89-06.

[3] L. W. Withlow, PhD thesis, SLAC-report-357 (1990)

[4] EMC Collab., M. Arneodo et al., Nucl. Phys. **B333** (1990) 1.

[5] NMC Collab., M. Arneodo et al., Phys. Lett. **B364** (1995) 107; NMC Collab., M. Arneodo et al., hep-ph/9610231 preprint, (1996).

[6] E665 Collab., M.R. Adams et al., Phys. Rev. **D54** (1996) 3006.

[7] M.W.Krasny, W.Placzek, H.Spiesberger, Z. Phys. **C53** (1992) 687.

[8] A. Courau, P. Kessler, Phys. Rev. **D33**, (1986) 2028.

[9] A. Kwiatkowski, H.-j. Möhring, H. Spiesberger, Characteristics of the Radiative Events in the Deep Inelastic ep Scattering at HERA, DESY 90-145, Nov. 1990, Hamburg.

[10] H1 Spacal group, R.-D. Appuhn et al., DESY 96-171, August 1996, submitted to Nucl. Instr. and Meth.

[11] A. Courau, P. Kessler, Phys. Rev. **D46**, (1992) 117.

[12] H1 Collab., I. Abt et al., Nucl. Instr. and Meth. **A386** (1997) 310 and **A386** (1997) 348.

[13] ZEUS Collab., M. Derick et al., Phys. Lett. **B293** (1992) 465; M. Derick et al., Z. Phys. **C63** (1994) 391.

[14] M. Botje, M. Klein, C. Pascaud, Proceedings of the workshop 1995/96 "Future Physics at HERA", Vol.1, ed. G. Ingelman, A. De Roeck, R. Klanmer, DESY, Hamburg, 1996

[15] H. Bethe, W. Heitler, Proc. Roy. Soc. **A146** (1934) 83.

[16] H1 collaboration, C. Berger et al., Technical proposal for the H1 detector, DESY-report PRC 86-02, Hamburg (1986), unpublished.

[17] P.Schmüser, Zur Fertigstellung von HERA, in Physikalische Blätter 46, Nr.12, 1990

[18] S. Levonian, A. Paintch, Treatment ot the Proton Satellite Bunches in 1994 Data, Interal report H1-09/95-454, DESY 1995

[19] Manufactured by Kyowa Gas Chemical Industry, see T. Kanon et al., Nucl. Instr. and Meth. 213 (1983) 261.

[20] S. Egli et al., Nucl. Instr. and Meth. **A283** (1989) 487.

[21] B. Andrieu et al., Nucl. Instr. and Meth. **A336** (1993) 460.

[22] J. Heatherington Analysis of the FToF data, H1 interal report H1-06/94-362, DESY 1994

[23] D. Zarbock, Phd thesis, in litt.

[24] J. Ban et al., Nucl. Instr. and Meth. **A372** (1996) 399-414.

[25] S. Burke et al., Track Finding and Fitting in the H1 Forward Track Detector, DESY preprint 95-132, Hamburg (1995), submitted to Nucl. Instr. and Meth.

[26] H. T. Duhme et al., H1 internal note, September 1991

[27] F. Sefkow et al., IEEE Trans. Nucl. Sci. 42, No. 4 (1995) 900.

[28] J. Ban et al., The BEMC single electron trigger, H1 internal report, H1-07/92-235, DESY (1992)

[29] J.C. Bizot et al., Hardware study for a topological level 2 trigger, H1 internal report H1-09/92-240, DESY, Hamburg (1992)
J.C. Bizot et al., Status of simulation for a topological level 2 trigger, H1 internal report H1-09/92-212, DESY (1992)

[30] J. Fent et al., A level 2 calorimeter trigger using neural networks, H1 internal report H1-04/91-172, DESY, Hamburg (1991)

[31] E. Barrelet et al., The hardware implementation of L3 triggers in H1, H1 internal report H1-12/88-100, DESY, Hamburg (1988)

[32] P. Fuhrmann et al., Data logging and online reconstruction in H1, contributed paper to CHEP '94, the Int. Conf.on Comp. in High Energy Physics, San Francisco (1994)

[33] A. Campbell, A RISC multiprocessor event trigger for the data acquisition system of the H1 experiment at HERA, Int. Conf. Real Time '91, Jülich, FRG (1991)

[34] S. Kermiche, Phd thesis, LAL 94-14.

[35] H1 Collaboration (T. Ahmed et al.), Experimental Study of Hard Photon Radiation Processes at HERA, DESY-95-024 / Z.Phys. **C66** (1995) 529.

[36] T. Kurča, PhD thesis, H1 internal report H1-06/94-364, DESY, Hamburg, (1994).

[37] B. Schwab, PhD thesis, University of Heidelberg (1996).

[38] M. Livan, V. Vercesi and R. Wigmans, Scintillating-Fibre Calorimetry, CERN 95-02, Feb. 1995

[39] H1 Spacal group, T. Nicholls et al., DESY 95-165, Sept. 1995, to appear in Nucl. Instr. and Meth. A374 (1996)

[40] HAMAMATSU photonics k.k., 314-5, Shimokanzo, Toyooka-village, Iwata-gun, Shizuoka-ken, 438-01 Japan.

[41] LeCroy Corporation, 1990 Research Instrumentation Catalog, NY, 1989.

[42] Bicron, 12345 Kinsman Road, Newbury, OH 44065, USA.

[43] S. Kermiche, //H1ECLASS/EC_RACO/EQEDC, DESY, October 1996.

[44] V Boudry et al., The Inclusive Electron Trigger for the Spacal Design and CERN-test Results, H1 internal report H1-03/95-430, DESY, Hamburg (1995)

[45] H1 Collaboration, Technical Proposal to Upgrade the Backward Scattering Region of the H1 Detector, PRC 93/02, DESY, Hamburg (1993)

[46] H1 Collaboration, Technical Proposal to built Silicon Tracking Detectors for H1, H1 internal report 06/92-226, DESY, Hamburg (1992)

[47] K. Müller, R. Beyer, 1995 L4 Filter Farm Selection Algorithm, H1 internal report, DESY, Hamburg (1996)

[48] Hamamatsu, Technical Data Sheet No. S-504-01, 1986.

[49] G. Blanar et al., Nucl. Instr. and Meth. **A203** (1982) 213.

[50] J. Heatherington at al., Studies on ToF FTDC data, H1 internal note H1-08/92-307, DESY, Hamburg (1992).

[51] M. Landon private communication.

[52] J. Ferencei, private communication, 1991.

[53] A. Courau private communication and H1 note in preparation.

[54] U. Goerlach, Proposal for an Active Beam Pipe Shielding in 1994 H1 internal note H1-12/93-333, DESY, Hamburg (1993)

[55] D. D. Pitzl, Abschirmung der HERA-Detektoren gegen Synchrotronstrahlung Diplomarbeit 1987, II. Institut für Experimentalphysik Universität Hamburg.

[56] J. Ferencei, K. Meier, Correspondence of the Pulser Level to Energy for BEMC H1/BEMC internal note 28-93

[57] P. Kessler, Nucl. Phys. **B15** (1970) 253.

[58] J. Dress, Springer Tracts in Modern Physics, edited by G. Hohler Springer, New York, 1971, Vol. 60, p. 107

[59] J. Dress, Acta Physica Austriaca 41, (1975) 141.

[60] C. Carimalo, G. Cochard, P. Kessler, J. Parisi and B. Roehneri, Phys. Rev. **D10**, (1974) 1561.

[61] Z. Zhang, A. Antmann, T. Constant, Feasibility study for the measuring $F_2(x, Q^2)$ at low Q^2 with inelastic QED Compton events at HERA, H1 internal report H1-10/96-495, DESY, Hamburg (1996).

[62] Ch. Brune, PhD thesis, University of Heidelberg (1996).

[63] A. Meyer, PhD thesis, University of Hamburg (1997).

[64] A. Panitch, PhD thesis, University of Brussels (1996).

[65] A. Glazov, PhD thesis, Humboldt University, Berlin (1998).

[66] S. Tapprogge, PhD thesis, University of Heidelberg (1996).

[67] C. Arndt, Diploma thesis, University of Hamburg (1996).

[68] M. Swart, Diploma thesis, University of Heidelberg (1996).

[69] M. Dirkmann, Diploma thesis, University of Dortmund (1995).

[70] R. Barschke, PhD thesis, University of Hamburg (1997).

[71] K. H. Spring, Photons and Electrons.

[72] L. Favart, H1 internal note H1-06/94-366, DESY, Hamburg (1994)

[73] J. C. Bizot, private communication.

[74] D. Hoffmann, M. Enzenberger,
http://www-h1.desy.de/itrigger/L2Trigger/l2tel.html

[75] V. Lamaitre, private communication.

[76] W. Eick et. al., Nucl. Instr. and Meth., **A386** (1997) 269.

[77] H1 Collaboration, T. Ahmed et al., Nucl. Phys. **B439** (1995) 471.

[78] U. Bassler and G. Bernardi, Nucl. Instr. and Meth. **A361** (1995) 197.

[79] G. Marchesini et al., Comp. Phys. Comm. **67** (1992) 465.

[80] H. U. Bengtsson and T. Sjöstrand, Computer Phys. Comm. **46** (1987) 43.

[81] N. H. Brook, A. De Roeck and A. T. Doyle, RAYPHOTON 2.0, Proceedings of the Workshop Physics at HERA, vol. 3, eds. W. Buchmüller, G. Ingelman, DESY (1992) 1453.

[82] L. Favart, Ph.D. Thesis, University of Brussels (1995).

[83] L. Favart et al., DESY grey report 96/01 (1996).

[84] ZEUS Collaboration, M. Derrick et al., DESY preprint 95-193 (1995).

[85] G. Altarelli and G. Martinelli, Phys. Lett. **B76** (1978) 89.

[86] W.J. Marciano, Phys. Rev. **D29** (1984) 580.

[87] H1 Collab., S. Aid et al., Phys. Lett. **B346** (1995), 415

[88] H1 Collab., S. Aid et al., Nucl. Phys. **B470** (1996) 3.

[89] H1 Collab., C. Adloff et al., Nucl. Phys. **B497** (1997) 3.

[90] ZEUS Collab., M. Derrick et al., Z. Phys. **C72** (1996) 399.

[91] H1 Collab., C. Adloff et al., DESY preprint 96-236 (1996).

[92] H1 Collab., T. Aid et al., Z. Phys. **C69** (1995) 27.

[93] ZEUS Collab., M. Derrick et al, Z. Phys. **C63** (1994) 408.

[94] G. A. Schuler and H. Spiesberger, Proceedings of the Workshop Physics at HERA, vol. 3, Eds. W. Buchmüller and G. Ingelman, DESY (1992) 1419.

[95] A. Kwiatkowski, H. Spiesberger and H.-J. Möhring, Comp. Phys. Comm. **69** (1992) 155.

[96] G. Ingelman, Proceedings of the Workshop Physics at HERA, vol. 3, Eds. W. Buchmüller and G. Ingelman, DESY (1992) 1366.

[97] L. Lönnblad, Comp. Phys. Comm. **71** (1992) 15.

[98] H1 Collab., I. Abt et al., Z. Phys. **C63** (1994) 377.

[99] ZEUS Collab., M. Derrick et al., Z. Phys. **C59** (1993) 231.

[100] T.Sjöstrand and M.Bengtsson, Comp. Phys. Comm. **43** (1987) 367;
H.-U.Bengtsson and T.Sjöstrand, Comp. Phys. Comm. **46** (1987) 43;
T.Sjöstrand, CERN-TH-6488 (1992).

[101] ZEUS Collab., M. Derrick et al., Phys. Lett. **B315** (1993) 481;
H1 Collab., T.Ahmed et al., Nucl. Phys. **B429** (1994) 477.

[102] H. Jung, Comp. Phys. Comm. **86** (1995) 147.

[103] B. List, Diplome Thesis, Technical University of Berlin (1993) (unpublished).

[104] H1 Collab., S. Aid et al., Nucl. Phys. **B468** (1996) 3;
H1 Collab., S. Aid et al., Nucl. Phys. **B463** (1996) 3.

[105] ZEUS Collab., M. Derrick et al., Z. Phys. **C69** (1995) 39;
ZEUS Collab., M. Derrick et al, Phys. Lett. **B380** (1996) 220;
ZEUS Collab., M. Derrick et al, Z. Phys. **C69** (1995) 39.